Copper chalcogenide nanoparticles as photocatalysts for the removal of pharmaceuticals from water

M.P.Ravele

orcid.org/0000-0003-3308-6835

Dissertation submitted in fulfillment of the requirements for the degree *Masters of Science in Chemistry* at the North-West University

Supervisor: Prof. D.C. Onwudiwe

Co-supervisor: Dr. O.A. Oyewo

Graduation ceremony: July 2022

Student number: 32470789

Declaration

I, Murendeni P. Ravele, student number 32470789, hereby declares that the work presented in this research project entitled: “Copper chalcogenide nanoparticles as photocatalysts for the removal of pharmaceuticals from water.” Submitted for the requirement of MSc Degree in Chemistry to the Department of Chemistry, North-West University, Mafikeng Campus is an original research work of my own under the supervision of Prof D.C. Onwudiwe. This research work has not previously been submitted to any other University or by another student of the North-West University or other University.

Signature — 19/07/2022 Date

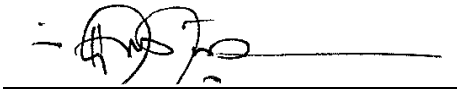

Signature supervisor — 19/07/2022 Date

Signature co-supervisor — 19/07/2022 Date

Dedication

This is in memory of my late father, Mr. Patrick. M. Ravele, your memory continues to live in me. Your love knew no boundaries; you have always brought laughter, always wanted to see the best in me. Thank you so much, Patrick “Ace,” for being the best father anyone would ever dream of and for always being there. May this dissertation continue to give you peace in paradise!

Acknowledgment

❖ I would first like to thank my supervisor, Professor Damian Onwudiwe, whose expertise was invaluable in formulating the research questions and methodology. Your insightful feedback pushed me to sharpen my thinking and brought my work to a higher level.

❖ I want to acknowledge my co-supervisor, Dr. Opeyemi Oyewo, for her excellent collaboration. I want to thank you for your patient support and all of the opportunities I was given to further my research.

❖ My gratitude goes to all the academic and laboratory staff of the Department of Chemistry, North-West University, Mafikeng Campus, for all the assistance provided throughout this study.

❖ To all Inorganic and Materials chemistry research group members, NWU, it has been great working alongside you all, and thank you for your encouragement and support.

❖ Most importantly, none of this could have happened without my family. To my mother, kids, and sisters, I am forever grateful. This dissertation stands as a testament to your unconditional love and encouragement.

❖ Finally, I could not have completed this dissertation without the support of my friends, Paula Maseko and Olalekan Christian Olatunde, who provided stimulating discussions as well as happy distractions to rest my mind outside of my research.

Abstract

In recent years, the development of efficient catalytic materials to degrade emerging contaminants in water has become a major research topic. This is due to an increased release of these types of contaminants into the environment and the inability of conventional technologies to remove them. Advanced oxidation processes (AOPs), which utilize generated reactive radicals to effect the degradation of molecules, have gained significant attention, not only because they can completely degrade emerging contaminants, but because they are environmentally friendly, cost-effective, and they have the potential mineralization of pollutants without generation of secondary waste. More attention is specifically focused on the use of semiconductor nanoparticles as catalysts for the generation of radical species in AOPs.

Copper chalcogenides CuE (E = O, S) are promising semiconductor materials with various stoichiometric phases that influence their optical and structural properties. These stoichiometric phases are dependent on the methods of preparation, which, when meticulously manipulated, could be used to obtain a wide array of materials with varying properties. This dissertation demonstrated control over stoichiometric phases of $Cu_{2-x}S$ using copper(II)dithiocarbamate complex as a single-source precursor by varying reaction parameters such as type of capping agent used and reaction temperature. While for CuO nanoparticles, copper(II)acetate monohydrate was used as the single-source precursor at different calcination temperatures. Solvothermal decomposition of copper(II) dithiocarbamate complex in dodecanthiol(DDT) was used to prepare pure phase djuleite($Cu_{31}S_{16}$) at 120 and 150 °C and roxbyite (Cu_7S_4) at 220 and 250 °C, while oleylamine was employed in the synthesis of pure phase CuS (covellite) at 120 °C and Cu_9S_5(degenite) at 220 °C. In between these two temperature extremes, mixed phases were obtained that were not subjected to further characterization. Copper oxide nanoparticles were prepared via the thermal decomposition of copper(II)acetate monohydrate at three different temperatures, which were informed by the decomposition profile of the complex when analyzed by thermogravimetric analysis. The as-prepared pure phase copper chalcogenide nanoparticles were further characterized using scanning electron microscope (SEM), transmission electron microscope (TEM), and UV-visible absorption spectroscopy.

The morphologies of the copper sulfides varied from pseudo spherical to spherical, and it was interesting to observe the digenite displayed rod shape morphology despite being prepared from

the same precursor compound. The copper sulfide samples were used as photocatalysts to degrade tetracycline (TC) as model antibiotics under visible light irradiation. The results of the study showed varying degradation efficiencies with Cu_7S_4 (250 °C) exhibiting the best activity in the reaction system of up to 99% within 120 min of light exposure, compared to CuS, Cu_9S_5, $Cu_{31}S_{16}$ (120 °C), $Cu_{31}S_{16}$ (150 °C) and (Cu_7S_4 (220 °C) which degraded 88, 98.5, 46.5, 85 and 90 % respectively under the same conditions.

The copper oxides of pure phases, obtained at 350 and 400 °C, labeled as CuO (350°C) and CuO (400 °C), respectively, were used to degrade acyclovir (ACV) as model antiviral. Both samples (CuO at 350°C and CuO at 400 °C) demonstrated high and comparable removal efficiency of 96.61 and 99.55 %, respectively, after 120 min. The results of this study confirm the potential of copper chalcogenides as semiconductor catalysts for the degradation of pharmaceuticals from an aqueous solution. In addition, the results showed that the phase of the chalcogenide affects the degradation efficiency.

List of publications

1. **Ravele, M.P.,** O.A. Oyewo, and D.C. Onwudiwe, Controlled synthesis of CuS and Cu_9S_5 and their application in the photocatalytic mineralization of tetracycline. *Catalysts*, 2021. 11(8): p. 899
2. **Ravele, M.P**., et al., Photocatalytic degradation of tetracycline in aqueous solution using copper sulfide nanoparticles. C*atalysts*, 2021. 11(10): p. 1238.

Table of Contents

Preface

This dissertation was written using the article format. All experimental works and drafting of the initial manuscript were done by Murendeni P.Ravele, while Prof. D. C. Onwudiwe and Dr. O.A. Oyewo carried out the supervision of the research work and proofreading of manuscripts. A total of two (2) published articles and one (1) submitted manuscripts were combined in compiling the thesis. The submitted manuscript is:

1. Copper oxide nanoparticles and their applications in the photocatalytic degradation of acyclovir (ACV) (*Journal of Photochemistry and Photobiology*)

All manuscripts have been included in this thesis with permission from all journal Editors and Co-authors.

List of figures

List of Schemes

List of tables

List of abbreviations

Cu_9S_5	Digenite
Cu_7S_4	Roxbyite
$Cu_{31}S_{16}$	Djurleite
$Cu_{1.75}S$	Anilite
$Cu_{1.4}S$	Spionkopite
$Cu_{1.12}S$	Yarrowite
$Cu_{1.6}S$	Geerite
CuS	Covelite
°C	Degrees Celsius
mg	Milligrams
g	Grams
nm	Nanometers
eV	Electronvolt
%	Percentage
min	Minutes
h	Hour
TEM	Transmission electron microscopy
SEM	Scanning electron microscopy
XRD	X-ray diffraction
UV-Vis-NIR	Ultraviolet visible near-infrared spectrophotometers

UV-Vis	Ultraviolet-visible spectrophotometers
PL	Photoluminescence spectroscopies
EDX	Energy-dispersive X-ray spectroscopy
NPs	Nanoparticles
TC	Tetracycline
ACV	Acyclovir
Eg	Bandgap
ECs	Emerging contaminants
mg/L	Milligram per liter
mpt	Melting point temperature
Cu_2O	Cuprous oxide
Cu_4O_3	Paramelaconite
CuO	Tenorite
JCPDS	Joint committee on powder diffraction standards
POP	Persistant pollutants
AOP	Advanced oxidation process
DDT	Dodocanthiol
OLA	Olaylamine
WWTPs	Waste water treatment plants
CEC	Contaminants of emerging concern
NC	nano crystals

EDS	Energy dispersive spectroscopy
FTIR	Fourier transform infrared
mmol	Milli mole
mL	Millilitre
hv	Photon energy
β	Band edge
TGA	Thermogravimetric analysis
DTG	Derivative thermogravimetry
DSC	Differential scanning calorimetry
θ	Theta
^{0}	Degree
$\mathbf{C_o}$	concentration at different times
$\mathbf{c_i}$	Initial concentration
$\mathbf{A_0}$	Blank abrorbance
$\mathbf{A_i}$	Absorbance at different times
BET	Brunauer-Emmett-Teller
CuDTC	Copper(II) dithiocarbamate
pKa	Dissociation constant
d	Crystalline size
$\mathbf{\mu mg^{-1}}$	micrograms per litre
λ	Wavelenth

Chapter 1

General background

1.0. Problem statement

Safe and clean water is one of the primary needs for humans and animals. However, many regions around the globe lack clean and safe water despite its availability naturally as groundwater and surface water. This is due to the presence of harmful water-soluble chemicals, including metal oxides, metal complexes, heavy metal ions, pharmaceutical ingredients, phenols, dyes, fertilizers, pesticides, surfactants, agricultural runoff, and pathogens emanated into the environment and water bodies [1]. Disposal of pharmaceutical are not regulated; their residues in the environment, also called "emerging contaminants (ECs)" of concern, have gained much attention. This is due to their (1) strong resistance/persistence, (2) wide range of applications and subsequent release into the aquatic and terrestrial environment, (3) substantial influences on human health and the environment. These persistent pollutants (POPs) are highly resistive to degradation due to their persistence, enabling them to be resilient. In addition, adverse health effects caused by these contaminants such as congenital disabilities, cancer, growth risk in infants, dysfunctional reproductive and immune systems on human health, and living creatures can be disastrous [2].

Different conventional and non-conventional treatments explored to remove pharmaceuticals include coagulation-flocculation, biodegradation, bio-filtration, ozonation, chemical precipitation, combined heterogeneous and advanced oxidation processes (AOPs), and adsorption. Most of these pharmaceuticals are polar micro-pollutants, thereby not easily removed by these conventional treatment methods. Examples of these pharmaceuticals are tetracycline and acyclovir [3][4]. Tetracycline is an antibiotic that is used to fight bacterial infections, while acyclovir is known as an antiviral medication. Both of them have also been combined to prepare ointment as part of drug therapy, especially in treating skin infections.

Recently AOPs have opened a new area of research using semiconductor materials for degrading pharmaceuticals. However, further investigation is required to improve the semiconductor synthesis route due to their large band gaps that cannot respond to visible light, cost, instability, complex preparation methods, and toxicity [5]. As such, research needs to concentrate on preparing semiconductor materials that have good absorption properties,economic, stable, safe to prepare, and environmentally friendly.

1.2.0. Motivation and rationale

Despite the advantages of unitary semiconductors, their shortcomings include activation within the UV range only (due to a large band gap), fast recombination between electron–hole pairs, and high tendency for agglomeration. Copper chalcogenides have proven to be promising alternative semiconductor materials due to their highly stable chemical structure, biocompatibility, environmental friendliness, and economical production. Combining these properties means that copper chalcogenides can initiate the AOPs effectively and play an essential role in the degradation of pharmaceuticals. The preparation method plays a vital role in the activity and stability of copper chalcogenides. Among the methods of synthesis solvothermal method using copper complexes as single- source precursors in the presence of a capping agent has materialized as a suitable option for preparing copper chalcogenides in such a way that it allows for optimization of reaction conditions and hence good stability, ability to undergo sharp decomposition with minor impurity, control over size, morphology, and crystal phase of the semiconductor material. By controlling the properties of the semiconductor, their influence as semiconductor catalysts could be studied.

1.3.0. Aim and Objectives

The study aims to develop efficient and cost-effective copper chalcogenide materials that could serve as photocatalysts to degrade antibiotics and antiviral-based pollutants in water.

To fulfill the aim, the following objectives were identified.

- To synthesize and characterize novel photocatalyst of copper sulfide and copper oxide nanoparticles,
- To evaluate the photocatalytic performance of copper sulfide and copper oxide nanoparticles on the degradation of tetracycline and acyclovir, respectively,
- To investigate the photocatalytic mechanism of copper sulfide and copper oxide nanoparticles.

1.4.0. References

1. Prasad, G., A. Reshma, and M.V. Ramesh, Assessment of drinking water quality on public health at Alappuzha district, southern Kerala, India. Materials Today: Proceedings, 2021.
2. Xu, L., *et al*., Occurrence, fate, and risk assessment of typical tetracycline antibiotics in the aquatic environment: A review. Science of the Total Environment, 2021. 753: p. 141975.
3. Du, C., *et al*., A review of metal organic framework (MOFs)-based materials for antibiotics removal via adsorption and photocatalysis. Chemosphere, 2021: p. 129501.
4. Anh, H.Q., *et al*., Antibiotics in surface water of East and Southeast Asian countries: A focused review on contamination status, pollution sources, potential risks, and future perspectives. Science of The Total Environment, 2021. 764: p. 142865.
5. Xu, Y., *et al*., Advances in technologies for pharmaceuticals and personal care products removal. Journal of Materials Chemistry A, 2017. 5(24): p. 12001-12014.

Chapter 2
Literature review
2.0. Emerging contaminants in water environment

Emerging contaminants (ECs), also referred to as contaminants of emerging concern (CECs), could be described as substances released into the environment without adhering to proper waste discharge regulations. These substances are mainly inorganic compounds that are present as disinfectants, food additives, wood preservatives, pesticides, and flame retardants. They also include pharmaceuticals and household substances such as personal care products, laundry detergents, hormones, surfactants, and other organic compounds present in water and generated mainly by human activities [1]. In the past decade the increase in the production and use of these relatively new classes of materials has increased concern over the long time safety of the environment [2-7]. They are synthetic persistent organic chemicals, thereby not usually controlled in the environment, but in the long term, can cause severe effects on human and environmental health.

In recent decades, the improvement in the techniques used to detect substances in the aquatic environment has resulted in the identification of an increasing number of contaminants and their transformation products, which were previously unknown in water bodies. There are more than 700 emerging contaminants grouped in 20 different classes as classified by NORMAN network [8, 9]. Figure 2.1. Shows some groups of ECs found in the environment that are released from manufacturing activities as the primary source of these threatening compounds.

2.1.0. Pharmaceuticals

Pharmaceuticals are a class of ECs that are currently not regulated properly; therefore, their metabolites have gained much attention due to their (1) strong persistence, (2) wide range of application, and subsequent release to the aquatic and terrestrial environment, (3) substantial influences on human health and the environment. These persistent contaminants are highly resistant to degradation and cause possible adverse effects on human health and living creatures, such as congenital disabilities, cancer, growth risk in infants, dysfunctional reproductive and immune systems [10-13]. The concern over ECs now seems like an obvious challenge due to the number of new diseases being discovered on a regular basis.

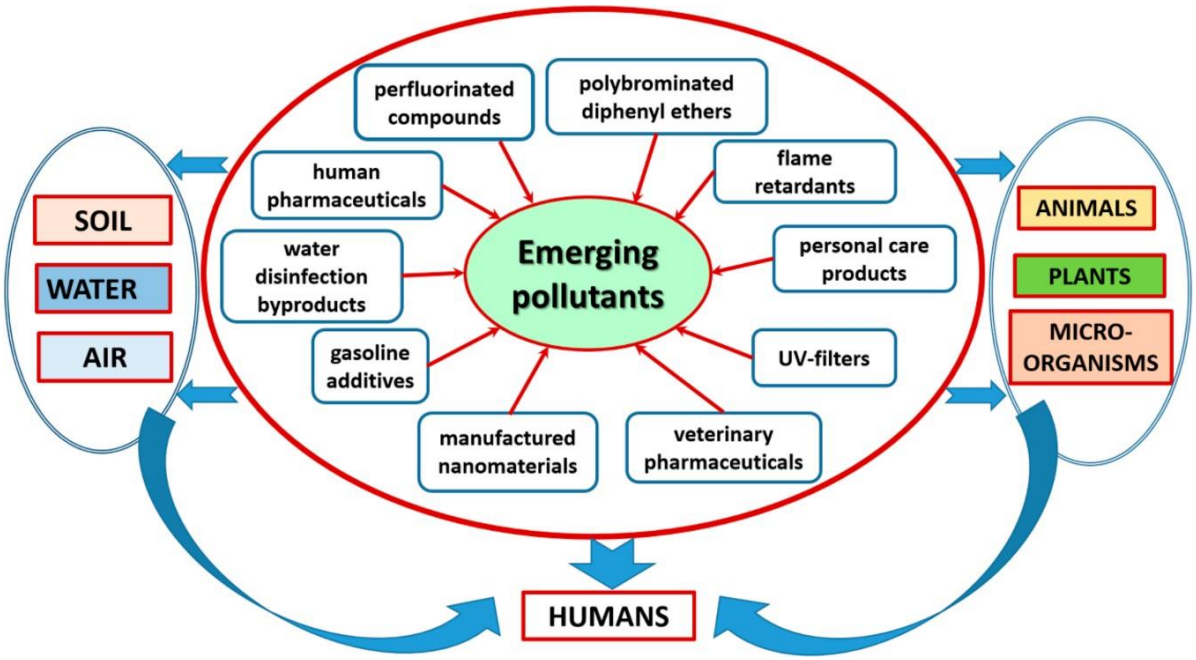

Figure 2. 1: Some groups of ECs in the environment [13].

Among the ECs, an increase in the usage, disposal, and production of pharmaceuticals for diagnosis, prevention, and treatment of emerging diseases in animals and humans has been recorded [14, 15]. Natural or synthetic chemicals found over the counter, therapeutic drugs, prescription medicines, and veterinary drugs are referred to as pharmaceuticals. These

compounds were designed to induce pharmacological effects, restore health, target specific organs, and confer significant social benefits.

Pharmaceuticals are released into the environment through several routes. One major route is their release from the human system either as metabolites or the unchanged compound. Figure 2.2. shows other potential routes through which pharmaceuticals enter the environment, including improper disposal of expired or unused medications, wastewater originating from the industrial processes of pharmaceutical manufacturing companies, and hospital effluents[16]. The presence of these pharmaceuticals has been identified in sewer water [17], surface water [18], groundwater [19], wastewater treatments plants (WWTPs) [20, 21], and even in drinking water [22].

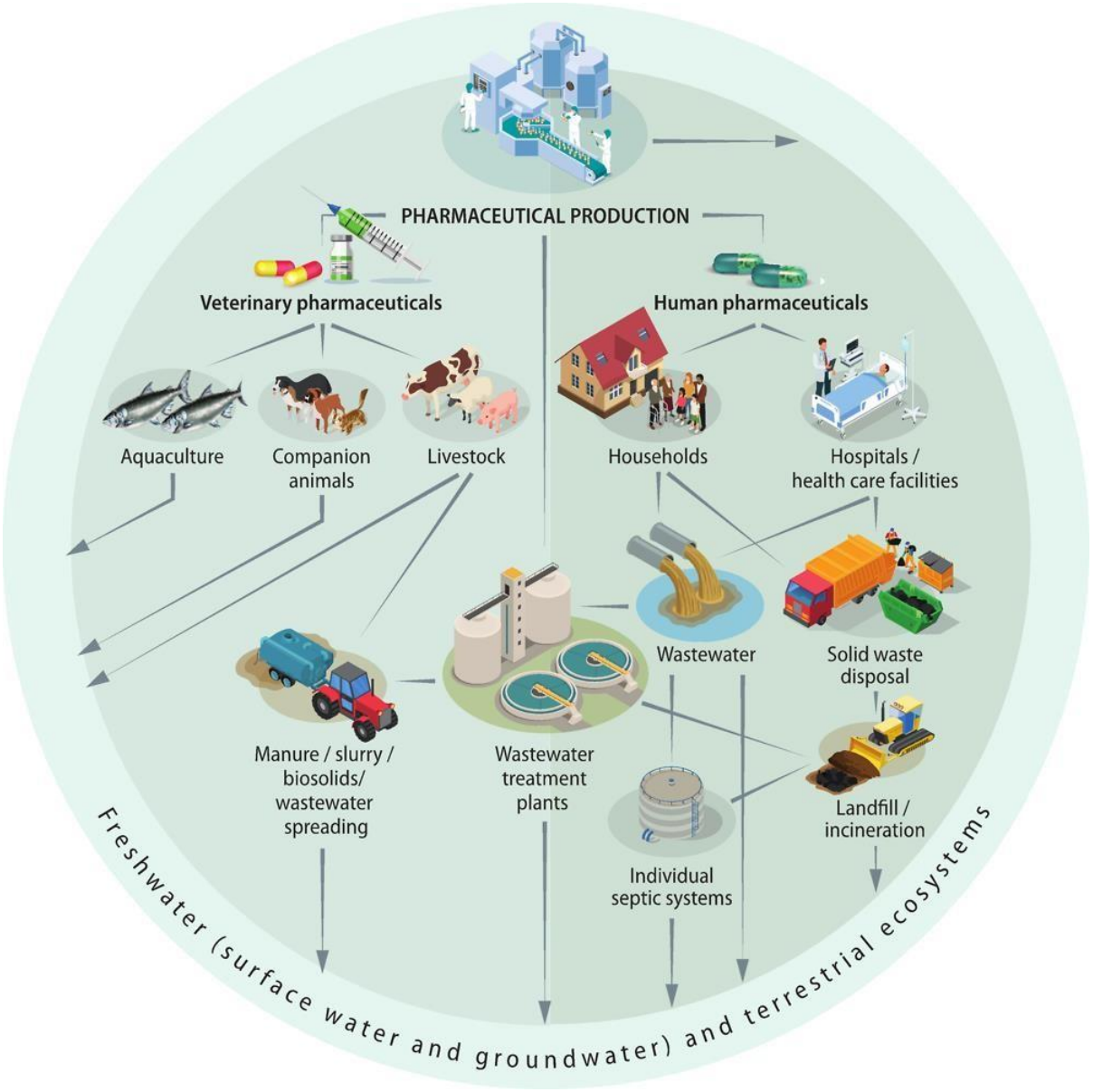

Figure 2. 2: Pharmaceutical routes to the environment [22].

When water from some of these sources is used for irrigation purposes, plants could take up these pharmaceuticals and thus find their way into the food chain. Even at a very low level, continuous exposure to pharmaceuticals has been identified as the cause of cancer and hormonal imbalance in humans, disrupting crucial physiological functions, reproduction, and metabolism and negatively impacting the homeostasis function of the endocrine system [23]. They could also exert some eco-toxicological effects on non-targeted organisms because of their active state in the environment [24, 25]. Pharmaceuticals can be categorized into different classes, including antibiotics, estrogens, contraceptives, nervous stimulants, beta-blockers, anti-inflammatory drugs, lipid regulators, analgesics, and antiepileptic drugs [16, 26]. Among these, anti-inflammatory/analgesics and antibiotics are the most consumed.

2.2.0. Antibiotics: Acyclovir and tetracycline

In human medicine, antibiotics are used to prevent or treat microbial infections. They are either manufactured or naturally occurring chemicals. The most used antibiotics include aminoglycoside, fluoroquinolone, quinolone, sulfonamide, macrolide, and tetracycline [27]. A significant challenge associated with antibiotics in the environment is the development of resistance by pathogens to antibiotics. This study will explore acyclovir (ACV) and tetracycline (TC) as model pharmaceuticals representing antiviral and antibacterial, respectively, because of their high consumption [28, 29].

2.2.1. Degradation pattern of acyclovir

Acyclovir (ACV) is an antiviral drug commonly used to treat the herpes simplex virus, varicella-zoster virus (VZV), cold sores, cytomegalovirus, Epstein - Barr virus, and hepatitis B virus (HBV)[30]. It has a short life span in the human body due to its low water solubility; therefore, it is usually prescribed in high doses. Among the administrated dose, it is reported that only15-20% is metabolized, while 80-85% is unmetabolized. These metabolites of ACVs have been found in the water recently due to their intensive use [31]. Prasse *et al*., reported 0.04-3.2 μgL^{-1} in groundwater, surface water, and drinking water [32, 33]. The consumption of these trace ACV can result in diarrhea, headache, and renal failure [34]. Taichena An *et al*., reported the three main degradation pathways proposed for ·OH initiating acyclovir degradation scheme 2.1. HPLC/MS study revealed the formation of six major degradation products [35] [36]. The following are the three pathways proposed for initiating degradation of ACV, (i) ·OH

reacts with ACV at C_8 to form · OH-adduct, hydroxylated products such as monohydroxylated(1) and dihydroxylated(2) are produced. (ii) some of the isocytosine moieties (products 3 and 4) formed by ·OH direct attack, which are further oxidized to product 5. (iii) ·OH attacks ACV through H abstraction at C_1, resulting in the formation of guanine, product 6. All formed products, and ACV could be mineralized into H_2O and CO_2 by elongating the irradiation time. Moreover, product 6 was used to confirm the ACV removal [36].

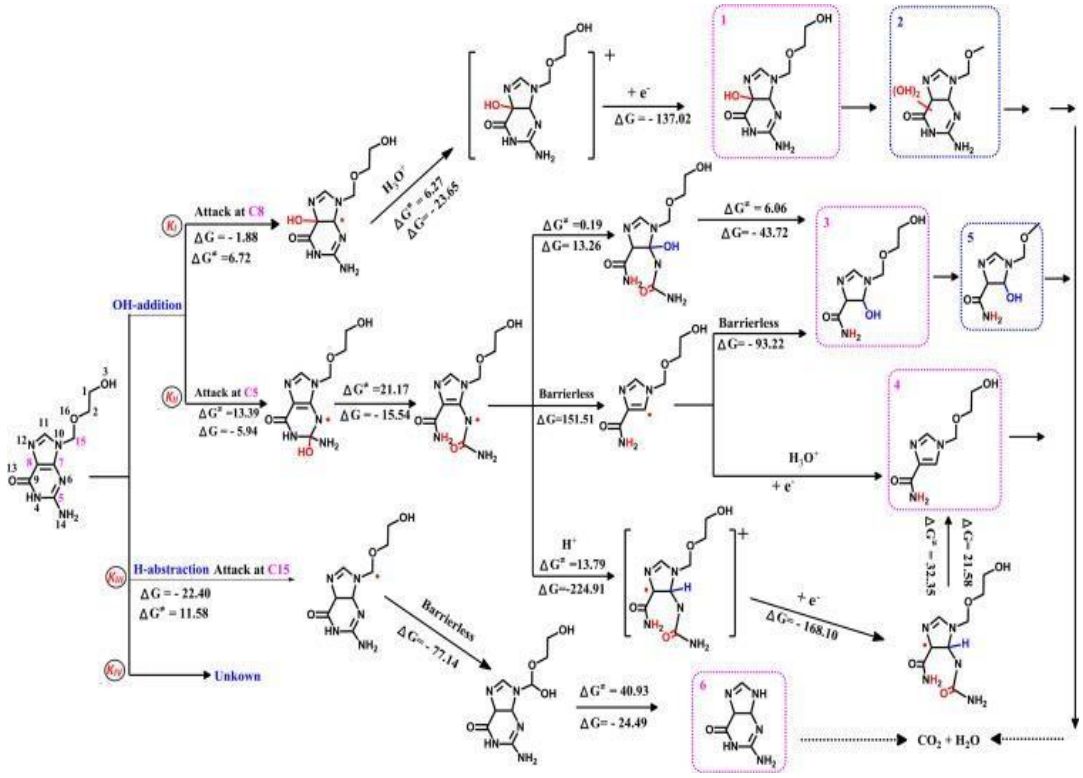

Scheme 2. 1: Proposed photocatalytic degradation mechanism of acyclovir [37]

2.2.2. Degradation pattern of tetracycline (TC)

The discovery of TC was by Benjamin Duggar, a Russian working under Yellapragada Subbarow at Lederle Laboratories in the 1940s. Their veterinary, human therapy and agricultural purposes began in the 1950s [38, 39]. TCs fall under the inexpensive class of antibiotics, which makes them affordable for developing countries. Its usage has been abused in the past decades, and, consequently, severe environmental problems, including human health damage and ecological risks, have been recorded [40]. Studies revealed that TC residues are found in different environmental compartments owing to their extensive usage [40, 41]. Their

residues stimulate the development of antibiotic-resistant microorganisms, which can prompt adverse effects on human health through their consumption in drinking water or water used for irrigation purposes on fruit and vegetable farms. These may distract human microflora, thereby increasing the risk of certain infections [42, 43]. Different photocatalysis has been used for the degradation of TC in water. Its breakdown includes the attack on some positions by different reactive oxygen species generated during the photocatalysis process. These photocatalytic degradations usually arise from the breakdown of the phenolic group, double bonds, amine, and N-dimethyl groups of the TC molecule [44]. According to Ren *et al*., the attack sites are highly functional groups and electron reach positions that active radicals, including O_2, can attack$^{\cdot-}$, OH$^{\cdot}$. h^+ and H_2O_2 [45]. As described by Xie *et al*., the potential TC degradation pathway includes hydroxylation, dealkylation, and dehydration under visible light, as shown in scheme 2. The attack on TC with molecular m/z=444.15 was first at the $^{\cdot}$OH forming its hydroxylated product, which via dealkylation was transformed to P1. Furthermore, P4 and P5 were obtained via dealkylation and dehydration reactions following the dehydration of P3. The opening of ring products including P6, P7, P8, P9, P10, and P11 were formed through the further oxidation of products R3, P6 and P7. Finally, CO_2 and H_2O were oxidized from the ring opening products [46] .

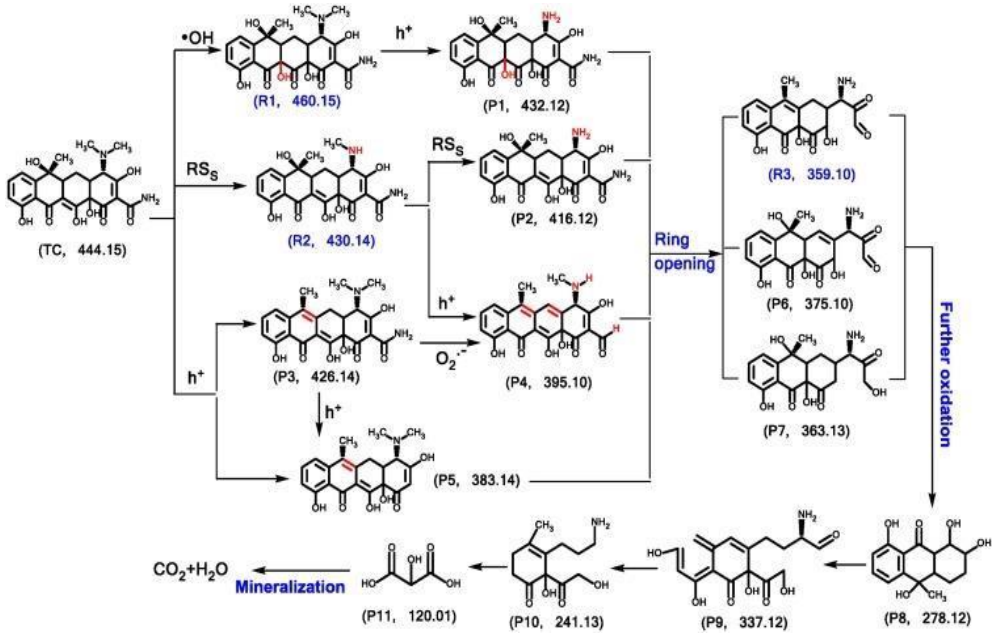

Scheme 2. 2: Proposed photocatalytic degradation mechanism of TC [46].

These antibiotics are soluble or slightly soluble in aqueous systems and are therefore not readily adsorbed in the subsoil, making them accumulate, persistent, and widely distributed in the environment. Consequently, they are detected in the environment at a concentration of $ngmL^{-1}$ to μmL^{-1} range due to their incomplete degradation [47, 48]. Their continued existence in water bodies has been associated with an increase in drug-resistant bacteria, which is harmful to human health. Although different studies have confirmed the presence of these antibiotics in the environment, conventional water treatment systems are currently not able to adequately deal with them. Both conventional and non-conventional treatment routes reported for the removal of antibiotics include coagulation-flocculation, bio-filtration, ozonation, biodegradation, chemical precipitation, combined heterogeneous and advanced oxidation processes (AOPs), and adsorption. Most of these antibiotics are polar micro-pollutants, thereby not easily removed by conventional treatment methods [49, 50][6]. The inefficiency of these methods has given rise to the need for a more practical approach that would ultimately degrade the antibiotics and remediate the environment from their toxic effect. Advanced oxidation processes (AOPs), such as photocatalysis, have proven to be an effective process for the complete degradation of TC, with the generation of H_2O and CO_2 as end products.

2.3.0. Photocatalysis and mechanism

In chemistry, chemical reactions carried out in the presence of light, and a photocatalyst are defined as photocatalysis. It is a promising technology for eliminating different classes of contaminants under light irradiation and different conditions. It has found its application in nitrogen fixation [51] [52], selective organic compound synthesis [53, 54], water splitting [55, 56], pollutant degradation [57] [58], CO_2 reduction and antibacterials [59, 60]. In water purification, photocatalysis is employed in the decomposition of contaminants, and its advantages include (1) low cost, (2) complete mineralization, (3) only mild pressure and temperature conditions required, and (4) no waste disposal problem [61]. The photocatalytic mechanism involves seven key steps, as shown in Figure 2.3. These steps can be categorized into four major stages: stage1- light absorption by the semiconductor to generate the electron-hole pair; stage 2- separation of excited charges; stages 3, 4, and 5- charge separation and movement to the semiconductor surface or recombine in bulk, stages 6 and 7- utilization of surface charges for redox reactions [62]. The surface morphology and the structure of the catalyst are significant as the photocatalyst strongly depends on them. Generally, a photon with energy equal to or above the semiconductor's bandgap is absorbed and produces carriers

consisting of holes and electrons, thereby promoting oxidation-reduction reactions. The electron in the VB of the photocatalyst is excited to its CB, creating a hole in the VB. The generated holes and electrons might combine or move to the catalyst surface, initiating different photo-redox reactions. Photocatalysis is performed in water under aerobic conditions, which involves water as reaction species and /or oxygen, reactive oxygen species (ROS), hydrogen peroxide (H_2O_2), superoxide radical ($O_2^{\bullet-}$), singlet oxygen (O_2), and hydroxyl radical (•OH). These are generated from surrounding water, oxygen molecules, or OH groups that are present on the surface of the catalyst. In photocatalytic degradation, free radicals and photoactivated holes are the primary oxidants, mineralizing pollutants into CO_2 and water.

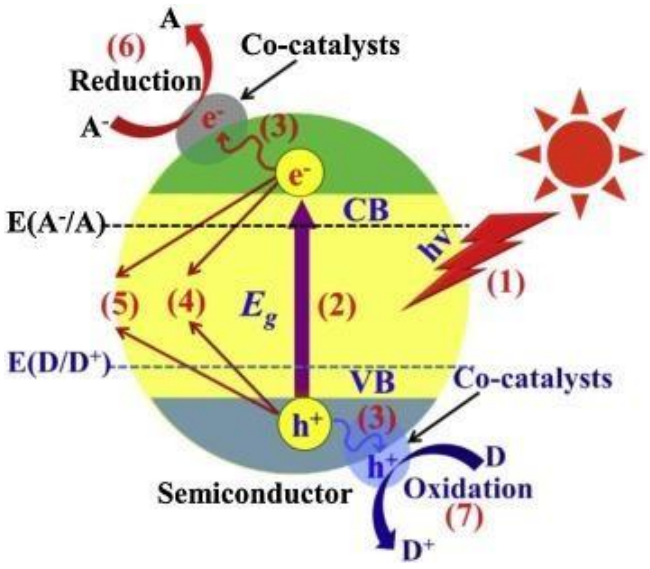

Figure 2. 3: The mechanism of photocatalysis [62].

Different metal sulfides, oxides, nitrides, and phosphates have been used as photocatalysts [62]. Their efficiency depends on utilizing the solar/light energy, which is also a factor of their band gap energies. Table 2.1 presents some of the semiconductor materials that have been used as photocatalysts and their corresponding band gap structures.

Table 2. 1. Semiconductor photocatalysts and their bandgap structures.

Semiconductor	**Crystal structure**	**Band Gap Structure (pH = 7, vs. NHE)**			**Ref.**
		CB	**VB**	**E_g/eV**	
Ag_3PO_4	cubic	0.04	2.49	2.45	[63]
TiO_2	Anatase	−0.5	2.7	3.2	[64]
g-C_3N_4		−1.3	1.4	2.7	[65, 66]
TaON		−0.75	1.75	2.5	[67]
CdS		−0.9	1. 5	2.4	[68]
g-C_3N_4		−1.53	1.16	2.7	[69]
$BiVO_4$		−0.3	2.1	2.4	[70]
Cu_2O		−1.16	0.85	2.0	[71]
WO_3		−0.1	2.7	2.8	[72]
Ta_3N_5		−0.75	1.35	2.1	[67]

The catalytic performance of photocatalysts is dependent on three factors, including light-harvesting, separation and transfer of photogenerated charge carriers, and surface reaction. The most stable photocatalysts have a large bandgap and limiting photocatalytic efficiency. The bandgap energy of a photocatalyst is closely related to light absorption. Therefore, a promising photocatalyst must meet the following criteria (1) high photostability, (2) enhanced photoactivity towards UV and visible light, (3) chemical and biological inertness, (4) environmental friendliness, and (5) low cost and ease of synthesis [73-75]. Different methods have been used to prepare these photocatalysts, and the methods of synthesis influence both their structural and optical properties. The following section discusses the different techniques that have been reported for the synthesis of nanoparticles.

2.4.0. Methods of synthesis of nanoparticles

In the past decades, nanoparticles having a size range from 1 to 100 nm have been the researchers' focus for their scientific interest and technological applications. They consist of interesting size-dependent structural, optical, electrical, chemical, and magnetic properties, which are not obtained in their bulk structures. The synthesis of nanoparticles could broadly be divided into physical and chemical methods. Physical processes have the advantages of producing nanoparticles in large quantities; however, the size control and uniformity of the NPs are challenging to achieve with this approach. On the other hand, the chemical synthesis method can synthesize uniform NPs with well-controlled size [76]. Varying the reaction conditions such as reaction temperature and surfactants can give rise to NPs with different shapes such as nanorods, spherical, nanosheets, etc. This control model is now utilized in materials such as metals as well as metal oxides.

The colloidal synthesis method is an oxygen-free, organic phase synthetic approach, which involves the thermal decomposition of precursor compounds, typically inorganic or organometallic complexes [77, 78]. The precursors are transformed chemically into monomers upon agitation, thereby providing essential constituents to form colloidal NPs.The utilization of the colloidal method of synthesis of nanoparticles has gained attraction owing to its advantages, such as the generation of monodispersed NPs, high crystallinity, and enhanced dispersibility in organic solvents. The protocol usually comprises of numerous steps (1) formation of nuclei from the initially homogeneous solution;(2) growth process of the preformed nuclei; (3) the isolation of nanoparticles from the solution of reaction mixture; and (4) post-synthetic purification of the nanoparticles through washing treatments to remove any unreacted precursors and ligands from the nanoparticles solution. These materials are characterized by different properties, of which their bandgap energy is very significant. The bandgap could either be direct or indirect or range within the value of $0<Eg<4$ eV. The chemical and physical properties of nanoparticles are significantly dependent on their structures, shapes, size, compositions, and surface chemistry. These have allowed nanoparticles to be utilized in various fields and applications such as electronics, catalysis, magnetism, biomedicine, and optics are widely reported. Thus, the vital requirement in the

synthesis of NPs is the excellent control of size and shape while maintaining their uniformity [79-82].

Although different chemical methods have been employed to prepare nanoparticulate materials, hot injection and heat-up techniques utilize homogeneous nucleation to synthesize NPs. Figure 2.4 shows the schematic representation of the heat-up approach, a batch process in which ligands, solvents, and precursors are initially placed in the flask, which is then mixed at low temperature, heated up to the preferred reaction temperature to start the nucleation and growth processes. The advantage of this technique is that it can be used for the large-scale production of NPs due to its simplicity[76, 83, 84].

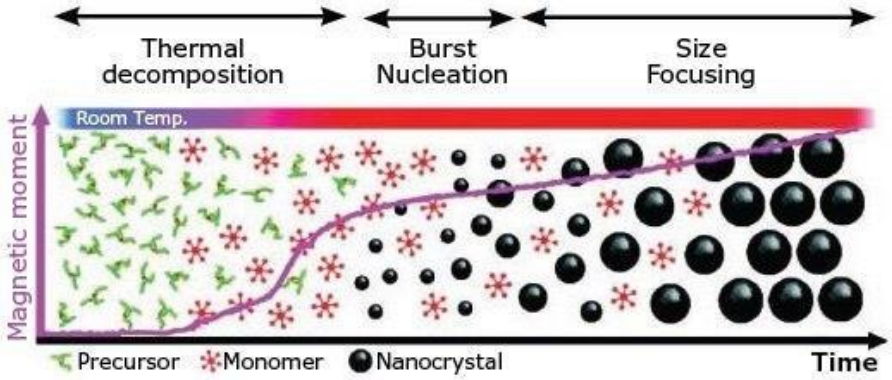

Figure 2. 4: The heat-up nanoparticles synthesis process [85]

In the heat-up technique, the nucleation process is longer than in hot injection. This has been attributed to the progressive generation of monomers with an increase in the supply of thermal energy [86]. Consequently, even after initiating the nucleation process, high supersaturation is maintained for a prolonged period; however, an undefined separation between the nucleation and growth stages eventually results in a broader size distribution during the heat-up process. In 1993 Bawendi group established the hot injection method (figure 2.5) to synthesize monodispersed Cd chalcogenide NPs, where cold precursor solution was injected into hot liquid. This technique was also extended to synthesizing different types of semiconductor NPs including metal sulfides and metal oxides [78, 87-90].

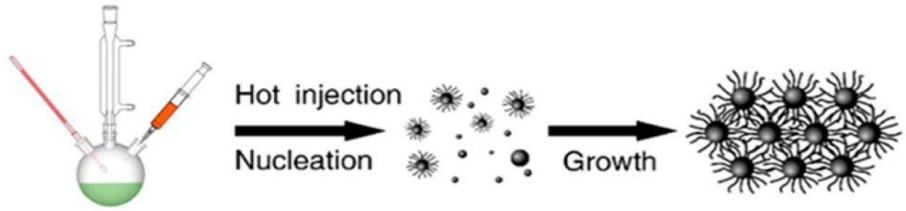

Figure 2. 5: The hot-injection nanoparticles synthesis process [77]

In the hot injection approach to nanoparticles synthesis, upon the injection of the precursor compound into the hot solution of the coordinating solvent, a higher degree of supersaturation is prompted. This leads to instantaneous nucleation burst resulting from the supersaturation free energy. Although the hot-injection and heat-up approach initial step is the burst of nucleation, which is then followed by the growth of the nuclei, enhanced uniformity of size is accomplished by the hot-injection route since the injection results in a single nucleation process giving rise to uniform growth of the nanoparticles[81, 91].

In selecting nanoparticles for a specific application, such as the treatment of contaminated water, one of the essential criteria considered is the environmental friendliness of the nanoparticles and the bandgap energy to ensure that maximum solar energy utilization. In the current project, the materials of choice are copper sulfide and copper oxide. In addition to the environmental friendliness of these copper chalcogenides, they are also made up of earth-abundant elements, which would positively impact their cost-effectiveness.

2.5.0.Copper chalcogenide nanocrystals (Copper oxide and Copper sulfide)

Copper chalcogenide nanocrystals have attracted great interest recently because of (1) their low cost, abundance, and low toxicity compared to other toxic metal chalcogenides such as lead and cadmium-based compounds; (2) excellent intrinsic functional properties, such as appropriate band gap energies for solar light absorption, excellent charge carrier mobilities, plasmonic properties, the potential for high carrier concentrations and low conductivity and;
(3) their composition, structural and stoichiometric versatility and also an abundance of non-stoichiometric phases, with related low energy of formation.

2.5.0.Copper oxide

Three distinctly different phases of copper oxide are cuprous oxide (Cu_2O), paramelaconite (Cu_4O_3), and tenorite (CuO), which are all p-type semiconductors having a direct bandgap. The

reported bandgap for Cu_2O is between 2.0-2.6 eV, while CuO is in the lower range of 1.2-1.6 eV[92, 93]. Copper oxide's crystal symmetry varies from cubic, tetragonal, and monoclinic for Cu_2O, Cu_4O_3, and CuO, respectively, as shown in Figure 2.6. CuO is the most stable phase, followed by Cu_2O, while Cu_4O_3 is the least stable phase.

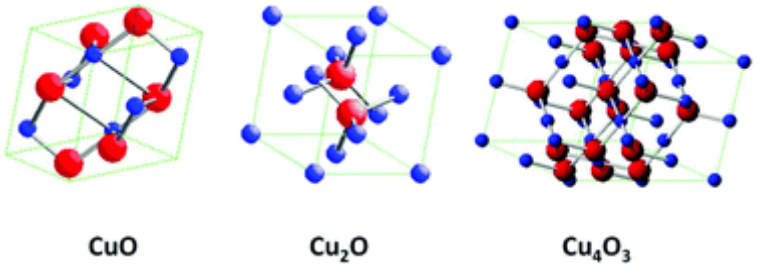

Figure 2. 6: Monoclinic, cubic, and tetragonal crystal structures of copper oxide compounds (blue and red spheres represent copper and oxygen atoms, respectively)

2.5.1.Copper sulfide

Copper sulfide $Cu_{2-x}S$ is a p-type semiconductor material, which is known for the diversity of its crystal phases, and it is comprised of several non-stoichiometric compositions. The bandgap energy range from 1.2-2.0 eV, making them promising semiconductors for technological applications [94] and photocatalytic application. The compound is made up of eight dominant crystal phases, as presented in Figure 2.7. The crystal phases are categorized by the cubic close packing of sulfur and copper atoms occupying different interstitial sites. Table 2.2 shows the nature of the packing of S atoms to the corresponding composition and mineral name.

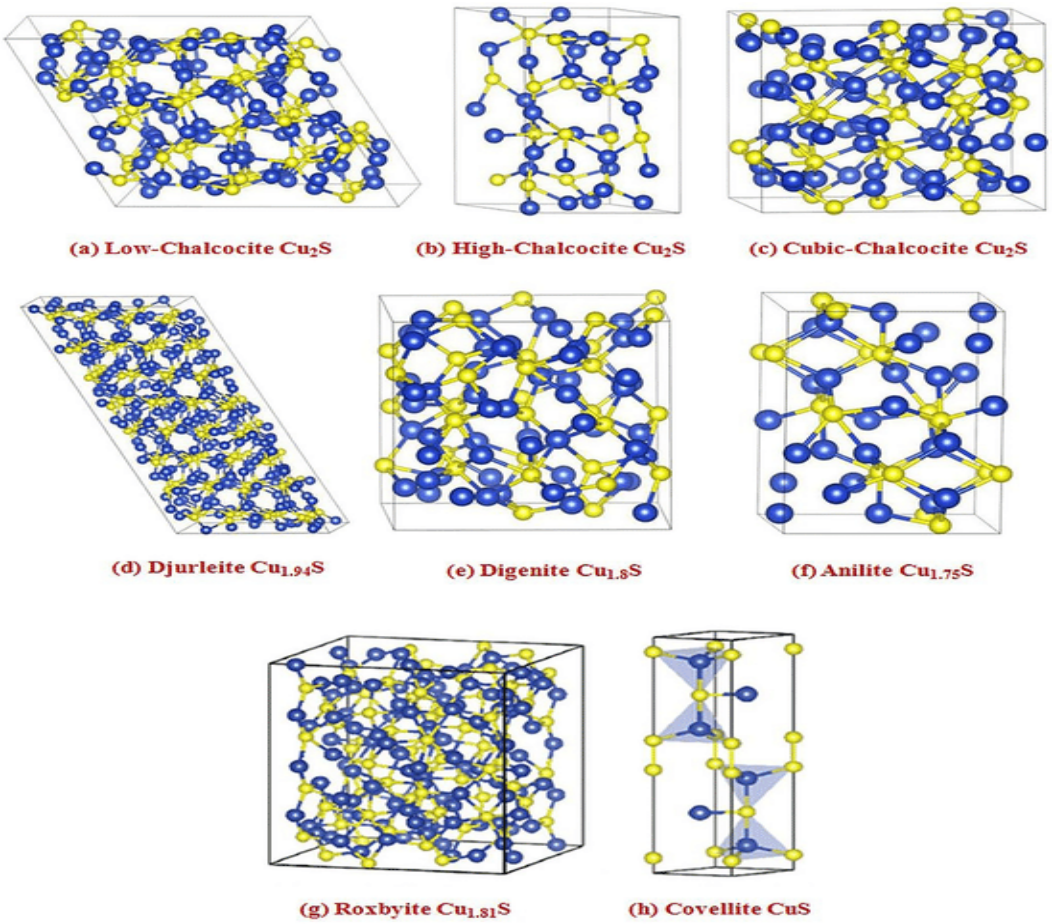

Figure 2. 7: Dominant crystal phases of copper sulfide [95]

Table 2. 2: Different copper sulfide minerals and corresponding compositions, sulfur (S) packing, and crystal system.

Mineral name	**Composition**	**Crytal system**	**S packing**
Anilite	Cu_7S_4 $Cu_{1.75}S$	Orthorhombic	Fcc
Covellite	CuS	Hexagonal	Hcp
Low-chalcocite	Cu_2S	Monoclinic	Hcp
Djurleite	$Cu_{31}S_{16}$ $Cu_{1.94}S_{1.97}$	monoclinic	Hcp
Cubic-Chalcocite	Cu_2S	Cubic	Fcc
Digenite	Cu_9S_5 $Cu_{1.8}S$	Cubic	Fcc
High-chalcocite	Cu_2S	Hexagonal	Hcp
Roxbyite	$Cu_{58}S_{32}$ $Cu_{1.81}S$	Triclinic	Hcp

2.6.0.Synthesis of copper chalcogenide nanocrystals

Copper chalcogenides NCs have been synthesized by various methods, Hydrothermal/solvothermal method, microwave-assisted method, hard-template-assisted and one-pot heat up method, etc. [96].

2.6.1.Hydrothermal/solvothermal method

In this method, the precursor solubility and reactivity are increased due to higher pressure and temperature used during the synthesis; the solvent can either be water (hydrothermal) or solvent/organic ligand molecule (solvothermal). A specialized vessel referred to as an autoclave is used as a reaction vessel. The autoclave is made out of three components, namely outer stainless steel, inner Teflon liner, and stainless steel cap, which can withstand higher pressure and temperatures. This method gives NPs with high crystallinity; however, the size is large and not ideal [97]. M.Saranya and A.Nirmala Grace prepared hydrothermally synthesized CuS; the work done by Z.H Han *et al*., gave $Cu_{1.8}S$ and $Cu_{31}S_{16}$ method [98] [99].

2.6.2. Template-assisted method

Micro-and nanostructured chalcogenides can be synthesized with controlled morphologies, sizes, and hollow/porous features using hard-template techniques, which can copy the template's feature set and transfer those to the final product after the template is removed. A three-step process is followed: (i) preparation of the template, (ii) growing desired nanomaterials on the surface or inside the pores of the templates, and (iii) selectively removing the templates to obtain the final nanostructures. Chun-Hong Kuo *et al*., successfully prepared Cu_2O and Cu_2S in addition; Yu Xin Zhang *et al*., prepared CuO using this method [100, 101].

2.6.3. Microwave Synthetic Method

In the microwave method, microwave energy is converted into thermal energy, thereby causing the creation of a chemical reaction for synthesizing nanomaterials via the thermolysis of copper chalcogenides nanoparticles complex precursors at frequencies in the range of 0.3 to 2.45 GHz. CuO nanoparticles' spherical shape and an average size of 4 nm were successfully prepared by Hui Wang et al., while CuS was prepared by Rong-huiLiu et al. [102,103].

2.6.4. Hot injection method using single-source precursors

An oxygen-free environment is required for the synthesis of copper sulfide. In the hot injection route, to achieve an inert reaction system, the setup usually involves using shleink apparatus connected to a three-neck round bottom flask charged with a condenser Figure 2.8. The precursor copper complex is dispersed in a high boiling point solvent such as dodecanethiol, octadecene, and oleylamine, which act as capping agents and reducing agents. Prior to initiation of the reaction, the solution is degassed at elevated temperature to remove water, followed by purging with nitrogen to remove any dissolved oxygen. The temperature is then increased to the preferred temperature and allowed to stir for at least 60 min. The NCs are washed with toluene/ethanol solvent and air-dried, followed by characterization [104].

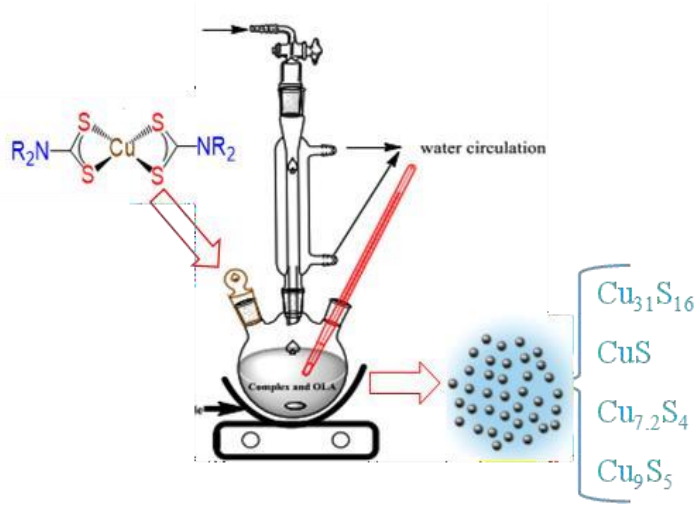

Figure 2. 8: Setup for solvothermal synthesis of nanoparticles

Copper Oxide can be prepared by employing the thermal decomposition of metal surfactant complexes. This is performed by simply heating the Cu substrate to a high temperature, usually between 200 and 800 °C, in an oxygen-rich environment [105].

2.7.0. Degradation of pharmaceuticals using copper oxide and copper sulfide

The activity of a catalyst is influenced by its optical properties, especially the bandgap energy. The copper chalcogenide powders' activity was reported in different studies. Previous reports have reported the copper oxide and copper sulfide photocatalytic performance on pharmaceuticals. G. O. El-Sayed *et al.*, used CuO as a catalyst to degrade metronidazole under the UV-radiation. The maximum degradation was 85 % in 120 min [106]. 99 % activity by Spherical-shaped Cu_7S_4 was reported for tetracycline [107].

2.8.0. References

1. Tang, Y., *et al*., *Emerging pollutants in water environment: Occurrence, monitoring, fate, and risk assessment.* Water Environment Research, 2019. **91**(10): p. 984-991.
2. Gusain, R., *et al*., *Adsorptive removal and photocatalytic degradation of organic pollutants using metal oxides and their composites: A comprehensive review.* Advances in colloid and interface science, 2019. **272**: p. 102009.
3. Xu, Y., *et al*., *Advances in technologies for pharmaceuticals and personal care products removal.* Journal of materials chemistry A, 2017. **5**(24): p. 12001-12014.
4. Yu, H., *et al*., *Degradation of diclofenac by advanced oxidation and reduction processes: kinetic studies, degradation pathways and toxicity assessments.* Water research, 2013. **47**(5): p. 1909-1918.
5. Zheng, B., *et al*., *Degradation of the emerging contaminant ibuprofen in aqueous solution by gamma irradiation.* Desalination, 2011. **276**(1-3): p. 379-385.
6. Birch, G., *et al*., *Emerging contaminants (pharmaceuticals, personal care products, a food additive and pesticides) in waters of Sydney estuary, Australia.* Marine pollution bulletin, 2015. **97**(1-2): p. 56-66.
7. Du, B., *et al*., *Pharmaceutical bioaccumulation by periphyton and snails in an effluent-dependent stream during an extreme drought.* Chemosphere, 2015. **119**: p. 927-934.
8. Geissen, V., et al., *Emerging pollutants in the environment: a challenge for water resource management.* International soil and water conservation research, 2015. **3**(1): p. 57-65.
9. Snow, D.D., *et al*., *Detection, occurrence and fate of emerging contaminants in agricultural environments.* Water Environment Research, 2017. **89**(10): p. 897-920.
10. Wahlang, B., *Exposure to persistent organic pollutants: impact on women's health.* Reviews on environmental health, 2018. **33**(4): p. 331-348.
11. Adithya, S., *et al*., *A critical review on the formation, fate and degradation of the persistent organic pollutant hexachlorocyclohexane in water systems and waste streams.* Chemosphere, 2021: p. 129866.
12. Zacharia, J.T., *Degradation pathways of persistent organic pollutants (POPs) in the environment*, in *Persistent Organic Pollutants*. 2019, IntechOpen.
13. Vasilachi, I.C., *et al*., *Occurrence and fate of emerging pollutants in water environment and options for their removal.* Water, 2021. **13**(2): p. 181.
14. Verlicchi, P., *et al*., *Hospital effluents as a source of emerging pollutants: an overview of micropollutants and sustainable treatment options.* Journal of hydrology, 2010. **389**(3-4): p. 416-428.
15. Gamarra Jr, J.S., *et al*., *Environmental Risk Assessment (ERA) of diclofenac and ibuprofen: A public health perspective.* Chemosphere, 2015. **120**: p. 462-469.
16. Thalla, A.K. and A.S. Vannarath, *Occurrence and environmental risks of nonsteroidal anti-inflammatory drugs in urban wastewater in the southwest monsoon region of India.* Environmental monitoring and assessment, 2020. **192**(3): p. 1-13.
17. Mutiyar, P.K. and A.K. Mittal, *Occurrences and fate of selected human antibiotics in influents and effluents of sewage treatment plant and effluent-receiving river Yamuna in Delhi (India).* Environmental monitoring and assessment, 2014. **186**(1): p. 541-557.

18. Petrović, M., *et al., Determination of 81 pharmaceutical drugs by high performance liquid chromatography coupled to mass spectrometry with hybrid triple quadrupole–linear ion trap in different types of water in Serbia.* Science of the total environment, 2014. **468**: p. 415-428.
19. Lin, Y.-C., *et al., Occurrence of pharmaceuticals, hormones, and perfluorinated compounds in groundwater in Taiwan.* Environmental monitoring and assessment, 2015. **187**(5): p. 1-19.
20. Kanama, K.M., *et al., Assessment of pharmaceuticals, personal care products, and hormones in wastewater treatment plants receiving inflows from health facilities in North West Province, South Africa.* Journal of toxicology, 2018. **2018**.
21. Gurke, R., *et al., Development of a SPE-HPLC–MS/MS method for the determination of most prescribed pharmaceuticals and related metabolites in urban sewage samples.* Journal of chromatography B, 2015. **990**: p. 23-30.
22. Riva, F., *et al., Monitoring emerging contaminants in the drinking water of Milan and assessment of the human risk.* International journal of hygiene and environmental health, 2018. **221**(3): p. 451-457.
23. Yilmaz, B., *et al., Endocrine disrupting chemicals: exposure, effects on human health, mechanism of action, models for testing and strategies for prevention.* Reviews in endocrine and metabolic disorders, 2020. **21**(1): p. 127-147.
24. Suárez, S., et al., *How are pharmaceutical and personal care products (PPCPs) removed from urban wastewaters?* Reviews in Environmental Science and Bio/Technology, 2008. **7**(2): p. 125-138.
25. Wu, X., Q. Fu, and J. Gan, *Metabolism of pharmaceutical and personal care products by carrot cell cultures.* Environmental Pollution, 2016. **211**: p. 141-147.
26. Martín, J., *et al., Occurrence of pharmaceutical compounds in wastewater and sludge from wastewater treatment plants: removal and ecotoxicological impact of wastewater discharges and sludge disposal.* Journal of hazardous materials, 2012. **239**: p. 40-47.
27. Pan, Y., *et al., Enhanced removal of antibiotics from secondary wastewater effluents by novel UV/pre-magnetized Fe0/H2O2 process.* Water research, 2019. **153**: p. 144-159.
28. Tong, X., *et al., Insights into the interactions between tetracycline, its degradation products and bovine serum albumin.* SpringerPlus, 2016. **5**(1): p. 1-9.
29. Irwin, K.K., et al., *Antiviral drug resistance as an adaptive process.* Virus evolution, 2016. **2**(1).
30. Gupta, A., R.K. Vyas, and A. Gupta, *Occurrence of acyclovir in the aquatic environment, its removal and research perspectives: A review.* Journal of Water Process Engineering, 2021. **39**: p. 101855.
31. Akimsheva, E.Y., E. Dolinina, and E. Parfenyuk, *Interactions of sol-gel encapsulated acyclovir with silica matrix.* Colloids and Surfaces B: Biointerfaces, 2019. **178**: p. 103-110.
32. Prasse, C., *et al., Biotransformation of the antiviral drugs acyclovir and penciclovir in activated sludge treatment.* Environmental science & technology, 2011. **45**(7): p. 2761-2769.

33. Prasse, C., *et al*., *Oxidation of the antiviral drug acyclovir and its biodegradation product carboxy-acyclovir with ozone: kinetics and identification of oxidation products.* Environmental science & technology, 2012. **46**(4): p. 2169-2178.
34. Portilla, D., L. Schnackenberg, and R.D. Beger. *Metabolomics as an extension of proteomic analysis: study of acute kidney injury*. in *Seminars in nephrology*. 2007. Elsevier.
35. Jia, T.-C., *et al*., *Photodegradation mechanisms of acyclovir in water and the toxicity of photoproducts.* Journal of Radioanalytical and Nuclear Chemistry, 2019. **320**(3): p. 823-830.
36. An, T., *et al*., *Photocatalytic degradation and mineralization mechanism and toxicity assessment of antivirus drug acyclovir: Experimental and theoretical studies.* Applied Catalysis B: Environmental, 2015. **164**: p. 279-287.
37. Thi, L.-A.P., *et al*., *Prospects and challenges of photocatalysis for degradation and mineralization of antiviral drugs*, in *Nanostructured Photocatalysts*. 2021, Elsevier. p. 489-517.
38. Chopra, I. and M. Roberts, *Tetracycline antibiotics: mode of action, applications, molecular biology, and epidemiology of bacterial resistance.* Microbiology and molecular biology reviews, 2001. **65**(2): p. 232-260.
39. Eliopoulos, G.M., G.M. Eliopoulos, and M.C. Roberts, *Tetracycline therapy: update.* Clinical infectious diseases, 2003. **36**(4): p. 462-467.
40. Daghrir, R. and P. Drogui, *Tetracycline antibiotics in the environment: a review.* Environmental chemistry letters, 2013. **11**(3): p. 209-227.
41. Chen, G., L. Zhao, and Y.-h. Dong, *Oxidative degradation kinetics and products of chlortetracycline by manganese dioxide.* Journal of hazardous materials, 2011. **193**: p. 128-138.
42. Heuer, O.E., et al., *Human health consequences of use of antimicrobial agents in aquaculture.* Clinical Infectious Diseases, 2009. **49**(8): p. 1248-1253.
43. Lopez Penalver, J.J., et al., *Degradation of tetracyclines in different water matrices by advanced oxidation/reduction processes based on gamma radiation.* Journal of Chemical Technology & Biotechnology, 2013. **88**(6): p. 1096-1108.
44. Wang, J., et al., *Evaluating tetracycline degradation pathway and intermediate toxicity during the electrochemical oxidation over a Ti/Ti_4O_7 anode.* Water research, 2018. **137**: p. 324-334.
45. Ren, L., *et al*., *Defects-engineering of magnetic γ-Fe_2O_3 ultrathin nanosheets/mesoporous black TiO_2 hollow sphere heterojunctions for efficient charge separation and the solar-driven photocatalytic mechanism of tetracycline degradation.* Applied Catalysis B: Environmental, 2019. **240**: p. 319-328.
46. Xie, Z., *et al*., *Construction of carbon dots modified MoO_3/g-C_3N_4 Z-scheme photocatalyst with enhanced visible-light photocatalytic activity for the degradation of tetracycline.* Applied Catalysis B: Environmental, 2018. **229**: p. 96-104.
47. El-Sheikh, S.M., *et al*., *Visible light activated carbon and nitrogen co-doped mesoporous TiO_2 as efficient photocatalyst for degradation of ibuprofen.* Separation and Purification Technology, 2017. **173**: p. 258-268.

48. Ray, S.K., D. Dhakal, and S.W. Lee, *Rapid degradation of naproxen by AgBr-α-$NiMoO_4$ composite photocatalyst in visible light: mechanism and pathways.* Chemical Engineering Journal, 2018. **347**: p. 836-848.
49. La Farre, M., *et al*., *Fate and toxicity of emerging pollutants, their metabolites and transformation products in the aquatic environment.* TrAC Trends in Analytical Chemistry, 2008. **27**(11): p. 991-1007.
50. Eslami, A., *et al*., *Photocatalytic degradation of ibuprofen and naproxen in water over NS-TiO_2 coating on polycarbonate: Process modeling and intermediates identification.* Inorganic Chemistry Communications, 2020. **115**: p. 107888.
51. Li, M., *et al*., *Recent progress on electrocatalyst and photocatalyst design for nitrogen reduction.* Small Methods, 2019. **3**(6): p. 1800388.
52. Zhao, Y., *et al*., *Alkali etching of layered double hydroxide nanosheets for enhanced photocatalytic N2 reduction to NH_3.* Advanced Energy Materials, 2020. **10**(34): p. 2002199.
53. Zhang, S., *et al*., *Photocatalytic ammonia synthesis: Recent progress and future.* EnergyChem, 2019. **1**(2): p. 100013.
54. Xiao, J., *et al*., *Heterogeneous photocatalytic organic transformation reactions using conjugated polymers-based materials.* ACS Catalysis, 2020. **10**(20): p. 12256-12283.
55. Lin, L., *et al*., *Molecular-level insights on the reactive facet of carbon nitride single crystals photocatalysing overall water splitting.* Nature Catalysis, 2020. **3**(8): p. 649-655.
56. Zhang, Z., *et al*., *A Highly Crystalline Perylene Imide Polymer with the Robust Built-In Electric Field for Efficient Photocatalytic Water Oxidation.* Advanced Materials, 2020. **32**(32): p. 1907746.
57. Deng, Y., *et al*., *Engineering the photocatalytic behaviors of g/C_3N_4-based metal-free materials for degradation of a representative antibiotic.* Advanced Functional Materials, 2020. **30**(31): p. 2002353.
58. Li, J., *et al*., *Synergistic photocatalytic decomposition of a volatile organic compound mixture: High efficiency, reaction mechanism, and long-term stability.* ACS Catalysis, 2020. **10**(13): p. 7230-7239.
59. Zhang, W., A.R. Mohamed, and W.J. Ong, *Z-Scheme photocatalytic systems for carbon dioxide reduction: where are we now?* Angewandte Chemie International Edition, 2020. **59**(51): p. 22894-22915.
60. Wang, L., *et al*., *An all-organic semiconductor C_3N_4/PDINH heterostructure with advanced antibacterial photocatalytic therapy activity.* Advanced Materials, 2019. **31**(33): p. 1901965.
61. Ameta, R., et al., *Photocatalysis*, in *Advanced oxidation processes for waste water treatment*. 2018, Elsevier. p. 135-175.
62. Wen, J., *et al*., *A review on g-C3N4-based photocatalysts.* Applied surface science, 2017. **391**: p. 72-123.
63. Yi, Z., *et al*., *An orthophosphate semiconductor with photooxidation properties under visible-light irradiation.* Nature materials, 2010. **9**(7): p. 559-564.

64. Ward, M.D., J.R. White, and A.J. Bard, *Electrochemical investigation of the energetics of particulate titanium dioxide photocatalysts. The methyl viologen-acetate system.* Journal of the American Chemical Society, 1983. **105**(1): p. 27-31.
65. Wang, X., *et al*., *A metal-free polymeric photocatalyst for hydrogen production from water under visible light.* Nature materials, 2009. **8**(1): p. 76-80.
66. Zhang, J., et al., *Synthesis of a carbon nitride structure for visible-light catalysis by copolymerization.* Angewandte Chemie International Edition, 2010. **49**(2): p. 441-444.
67. Chun, W.-J., *et al*., *Conduction and valence band positions of Ta2O5, TaON, and Ta3N5 by UPS and electrochemical methods.* The Journal of Physical Chemistry B, 2003. **107**(8): p. 1798-1803.
68. Finlayson, M.F., *et al*., *Determination of flat-band position of cadmium sulfide crystals, films, and powders by photocurrent and impedance techniques, photoredox reaction mediated by intragap states.* The Journal of Physical Chemistry, 1985. **89**(26): p. 5676-5681.
69. Yan, S., *et al*., *Organic–inorganic composite photocatalyst of gC_3N_4 and TaON with improved visible light photocatalytic activities.* Dalton Transactions, 2010. **39**(6): p. 1488-1491.
70. Long, M., W. Cai, and H. Kisch, *Visible light induced photoelectrochemical properties of n-$BiVO_4$ and n-$BiVO_4$/p-Co_3O_4.* The Journal of Physical Chemistry C, 2008. **112**(2): p. 548-554.
71. de Jongh, P.E., D. Vanmaekelbergh, and J.J. Kelly, *Cu_2O: a catalyst for the photochemical decomposition of water?* Chemical Communications, 1999(12): p. 1069-1070.
72. Hardee, K.L. and A.J. Bard, *Semiconductor electrodes: X. Photoelectrochemical behavior of several polycrystalline metal oxide electrodes in aqueous solutions.* Journal of the Electrochemical Society, 1977. **124**(2): p. 215.
73. Han, C., et al., *Gold nanorods-based hybrids with tailored structures for photoredox catalysis: fundamental science, materials design and applications.* Nano Today, 2019. **27**: p. 48-72.
74. Xu, Y.-J., *Promises and Challenges in Photocatalysis.* Frontiers in Catalysis, 2021. **1**: p. 6.
75. Molinari, R., C. Lavorato, and P. Argurio, *Visible-light photocatalysts and their perspectives for building photocatalytic membrane reactors for various liquid phase chemical conversions.* Catalysts, 2020. **10**(11): p. 1334.
76. Park, J., et al., *Synthesis of monodisperse spherical nanocrystals.* Angewandte Chemie International Edition, 2007. **46**(25): p. 4630-4660.
77. Coughlan, C., et al., *Compound copper chalcogenide nanocrystals.* Chemical reviews, 2017. **117**(9): p. 5865-6109.
78. Kwon, S.G. and T. Hyeon, *Colloidal chemical synthesis and formation kinetics of uniformly sized nanocrystals of metals, oxides, and chalcogenides.* Accounts of chemical research, 2008. **41**(12): p. 1696-1709.
79. Li, J., Q. Wu, and J. Wu, *Synthesis of Nanoparticles via Solvothermal and Hydrothermal Methods 12.* 2016.

80. Chang, J. and E.R. Waclawik, *Colloidal semiconductor nanocrystals: controlled synthesis and surface chemistry in organic media.* RSC Advances, 2014. **4**(45): p. 23505-23527.
81. Yin, Y. and A.P. Alivisatos, *Colloidal nanocrystal synthesis and the organic–inorganic interface.* Nature, 2005. **437**(7059): p. 664-670.
82. Talapin, D.V., *et al.*, *Prospects of colloidal nanocrystals for electronic and optoelectronic applications.* Chemical reviews, 2010. **110**(1): p. 389-458.
83. Park, J., et al., *Ultra-large-scale syntheses of monodisperse nanocrystals.* Nature materials, 2004. **3**(12): p. 891-895.
84. Kwon, S.G., et al., *Kinetics of monodisperse iron oxide nanocrystal formation by "heating-up" process.* Journal of the American Chemical Society, 2007. **129**(41): p. 12571-12584.
85. Sinatra, L., J. Pan, and O.M. Bakr, *Methods of synthesizing monodisperse colloidal quantum dots.* Material Matters, 2017. **12**: p. 3-7.
86. van Embden, J., A.S. Chesman, and J.J. Jasieniak, *The heat-up synthesis of colloidal nanocrystals.* Chemistry of Materials, 2015. **27**(7): p. 2246-2285.
87. Murray, C., D.J. Norris, and M.G. Bawendi, *Synthesis and characterization of nearly monodisperse CdE (E= sulfur, selenium, tellurium) semiconductor nanocrystallites.* Journal of the American Chemical Society, 1993. **115**(19): p. 8706-8715.
88. Guo, Q., et al., *Sulfide nanocrystal inks for dense Cu (In1− x Gax)(S1− y Se y) 2 absorber films and their photovoltaic performance.* Nano letters, 2009. **9**(8): p. 3060-3065.
89. Tang, J., *et al.*, *Synthesis of Colloidal $CuGaSe_2$, $CuInSe_2$, and Cu (InGa) Se_2 Nanoparticles.* Chemistry of materials, 2008. **20**(22): p. 6906-6910.
90. Pan, D., et al., *Synthesis of Cu− In− S ternary nanocrystals with tunable structure and composition.* Journal of the American Chemical Society, 2008. **130**(17): p. 5620-5621.
91. Peng, X., J. Wickham, and A. Alivisatos, *Kinetics of II-VI and III-V colloidal semiconductor nanocrystal growth:"focusing" of size distributions.* Journal of the American Chemical Society, 1998. **120**(21): p. 5343-5344.
92. Balamurugan, B. and B. Mehta, *Optical and structural properties of nanocrystalline copper oxide thin films prepared by activated reactive evaporation.* Thin solid films, 2001. **396**(1-2): p. 90-96.
93. Ogwu, A., *et al., The influence of rf power and oxygen flow rate during deposition on the optical transmittance of copper oxide thin films prepared by reactive magnetron sputtering.* Journal of Physics D: Applied Physics, 2005. **38**(2): p. 266.
94. Ravele, M.P., O.A. Oyewo, and D.C. Onwudiwe, *Controlled Synthesis of CuS and Cu_9S_5 and Their Application in the Photocatalytic Mineralization of Tetracycline.* Catalysts, 2021. **11**(8): p. 899.
95. Majumdar, D., *Recent progress in copper sulfide based nanomaterials for high energy supercapacitor applications.* Journal of Electroanalytical Chemistry, 2021. **880**: p. 114825.
96. Xu, W., *et al.*, *Localized surface plasmon resonances in self-doped copper chalcogenide binary nanocrystals and their emerging applications.* Nano Today, 2020. **33**: p. 100892.

97. Yadav, S., S.R. Yashas, and H.P. Shivaraju, *Transitional metal chalcogenide nanostructures for remediation and energy: a review.* Environmental Chemistry Letters, 2021. **19**(5): p. 3683-3700.
98. Saranya, M. and d.A. Nirmala Grace. *Hydrothermal synthesis of CuS nanostructures with different morphology*. in *Journal of Nano Research*. 2012. Trans Tech Publ.
99. Han, Z., et al., *A simple solvothermal route to copper chalcogenides.* Materials Letters, 2000. **44**(6): p. 366-369.
100. Kuo, C.H., *et al.*, *Cu_2O nanocrystal-templated growth of Cu_2S nanocages with encapsulated Au nanoparticles and in-situ transmission X-ray microscopy study.* Advanced Functional Materials, 2011. **21**(4): p. 792-797.
101. Zhang, Y.X., *et al.*, *Facile synthesis of mesoporous CuO nanoribbons for electrochemical capacitors applications.* Int. J. Electrochem. Sci, 2013. **8**: p. 1366-1381.
102. Wang, H., *et al.*, *Preparation of CuO nanoparticles by microwave irradiation.* Journal of crystal growth, 2002. **244**(1): p. 88-94.
103. Liu, R.-h., *et a*l., *Microwave-assisted synthesis of self-assembled camellia-like CuS superstructure of ultra-thin nanosheets and exploration of its sodium ion storage properties.* Journal of Electroanalytical Chemistry, 2021. **898**: p. 115607.
104. Wang, F., *et al.*, *Monodisperse copper chalcogenide nanocrystals: controllable synthesis and the pinning of plasmonic resonance absorption.* Journal of the American Chemical Society, 2015. **137**(37): p. 12006-12012.
105. Vila, M., C. Diaz-Guerra, and J. Piqueras, *Optical and magnetic properties of CuO nanowires grown by thermal oxidation.* Journal of Physics D: Applied Physics, 2010. **43**(13): p. 135403.
106. El-Sayed, G., *et al.*, *Photocatalytic degradation of metronidazole in aqueous solutions by copper oxide nanoparticles.* J Basic Environ Sci, 2014. **1**: p. 102-110.
107. Ravele, M.P., *et al.*, *Photocatalytic Degradation of Tetracycline in Aqueous Solution Using Copper Sulfide Nanoparticles.* Catalysts, 2021. **11**(10): p. 1238.

Chapter 3

Controlled synthesis of CuS and Cu_9S_5 and their application in the photocatalytic mineralization of tetracycline

3.0 Introduction

Copper sulfide is an interesting metal sulfide that has attracted huge research attention due to its interesting optical and structural properties. It exists in different stoichiometry and crystalline phases, and it is a typical p-type semiconductor. The bandgap energy ranges from 1.2 to 2.0 eV and greatly depends on both the stoichiometry and phases. Its non-toxicity, unique structural properties, and fascinating functional properties are some of its advantages over other related semiconductors such as CdS [1, 2]. The stoichiometry varies from the Cu-rich to Cu deficient phases [3, 4] and the non-stoichiometric phases. These include the digenite ($Cu_{1.8}S$) [5], roxbyite (Cu_7S_4) [6], djurleite ($Cu_{1.97}S$) [7, 8], anilite ($Cu_{1.75}S$) [9], spionkopite ($Cu_{1.4}S$) [10], yarrowite ($Cu_{1.12}S$) [10], and geerite ($Cu_{1.6}S$) [10]. They all exhibit strong optical absorption in the near-infrared region [11]. These properties make them promising materials in various areas of application such as photocatalysis, solar cells, lithium batteries, and sensing materials. The accurate stoichiometry, which is dependent on the preparative conditions used, affects the properties of copper sulfide [12].

The synthesis of copper sulfide has been achieved using different approaches such as microwave irradiation [13, 14], hydrothermal [15, 16], sonochemical [17, 18], hot injection [19], solvothermal [20], thermolysis of single-source precursor [3]. The use of single-source precursor compounds is of great interest because they generate mostly more stable nanoparticles, are cheaper, and eliminate. The use of copper dithiocarbamate complexes as single-source precursors to prepare the copper sulfide nanoparticles has proven to be an efficient route and gives rise to good quality copper sulfides [3, 21]. In copper dithiocarbamate complexes, the crystallinity phase, size, shape, and physical properties of the copper sulfide are determined by the type of capping agent used and temperature. Capping agents could be used to stabilize the surface of copper sulfide to prevent agglomeration and obtain monodispersed nanoparticles [22]. The varying morphology of copper sulfide such as nanorods[13, 23], nanowires [7], flowerlike [14, 24], nanotubes [25], nanoplates [26, 27], spherical [3], nanodisks [28],

nanosheets [29], hollow spheres [30] also depend largely on the type of capping agent used, among other factors.

Antibiotics are one of the most important drugs used to prevent and treat microbial infections [31], and tetracycline (TC) is one of the common antibiotics used to treat animal and human diseases. It is made up of multiple ionizable functional groups such as hydroxyl, phenolic, and dimethyl amino groups. In addition, TC is a hydrophilic antibiotic; therefore, it is attracted to water molecules and easily dissolves [32]. However, the unreasonable use of TC and its release into the environment results in the contamination of water courses [33]. The severity of health risks posed by TC has been well studied [31]. For example, wastewater from pharmaceutical, aquaculture, and hospital activities contains decomposed chemicals and a high concentration of TC that pose a serious risk to humans and the environment [34]. Series of health issues related to high amounts of TC consumption have been widely reported [35]. Excessive TC in the human body could cause nausea, vomiting, diarrhea, loss of appetite, headache, mouth sores, sore throat, dizziness, and rectal discomfort [36]. The abuse of TC has been reported to increase the chances of disease transmission to humans through water, soil, or the consumption of affected food products, animals, or livestock [37]. TC also carries the risk of bone growth reduction and permanent discoloration of teeth when consumed by pregnant women or children under nine years [38].

The existing advanced methods for TC removal or mineralization includes adsorption[39-41], coagulation/flocculation [42], and degradation using catalyst [43, 44]. Adsorption is commonly used in developing countries because of its low cost and ease of materials preparation [45]. However, the ability to degrade TC into harmless and useful minerals using the photocatalysis route provides additional benefit and high economic feasibility over the adsorption route in terms of efficiency and no secondary waste generation. Hence, the preparation of semiconductor materials as possible photocatalysts for the effective removal of pollutants from water continues to generate research interest.

This paper reports a solvothermal method for the controlled synthesis of covellite (CuS) and digenite (Cu_9S_5) nanostructures by using copper dithiocarbamate as a single-source precursor, temperature variation, and oleylamine as the stabilizing agent. The as-prepared nanopowders were also successfully used as photocatalysts for the photodegradation of tetracycline in an aqueous solution.

3.1.0. Material and methods

3.1.1. Materials

All the chemical reagents used, including 4-ethylaniline, p-tolualdehyde, methanol, ethanol, carbon disulfide, dichloromethane, potassium hydroxide, sodium borohydride, and copper(II) chloride dihydrate, were purchased from Merck chemicals. They were analytical grade and were used as received without further purification.

3.1.2. Instrumentation

The crystalline structures were studied using powder XRD on a Bruker D8 Avance X-Ray Diffractometer (Karlsruhe, Germany). Microstructural studies were carried out using a transmission electron microscope (Hitachi HF–2000 TEM at 200 kV by Hitachi High-Tech Corporation, Tokyo, Japan) operated at 200 kV and a JEOL 6400F field-emission SEM (Zeiss, Oberkochen Germany). The atomic-level compositions were examined by energy-dispersive spectroscopy (EDS) attached to the SEM. Functional groups of the complex were studied using Fourier transform infrared (FTIR) spectroscopy on a Bruker Alpha-P FTIR spectrometer (Bremen, Germany). The absorption spectra were measured using Prove 300 Spectroquant (Merck, Burlington MA, USA), while the photoluminescence measurement was carried out using LS 45 Fluorimeter (Perkin Elmer, Waltham, MA, USA).

3.1.3. Preparation of copper(II) bis(N-4-methyl benzyl)-N-(4-ethyl phenyl) dithiocarbamate

4-ethylaniline (4.0 mmol) and p-tolualdehyde (4.0 mmol) were dissolved in methanol, after which their solutions were mixed and then stirred steadily at room temperature. After 2 h, the solution was evaporated to remove the solvent. The resulting oily product was dissolved in a 20 mL solution of methanol and dichloromethane (1:1). To this solution, sodium borohydride was added (2.8 mmol), and stirring was maintained for 2 h in ice, followed by 20 h stirring at room temperature. After that, the solvent was evaporated, rinsed with water, and extracted with dichloromethane. The solvent was removed to give oily substituted amine, and the product was rinsed with water and extracted using dichloromethane. The evaporation of the organic layer gave the substituted amine as a brownish oil. The substituted amine was dissolved in ethanol, and then potassium hydroxide (4.0 mmol) was added to the solution and stirred for 30

min, followed by dropwise addition of carbon disulfide (4.0 mmol), while the temperature was maintained for two h. Copper(II) chloride dihydrate (2.0 mmol) was added to the solution with constant stirring. The resulting precipitate, copper(II) bis(N-4-methylbenzyl)-N-(4-ethylphenyl) dithiocarbamate, was washed with cold water and then air-dried (Scheme 3.1) [46].

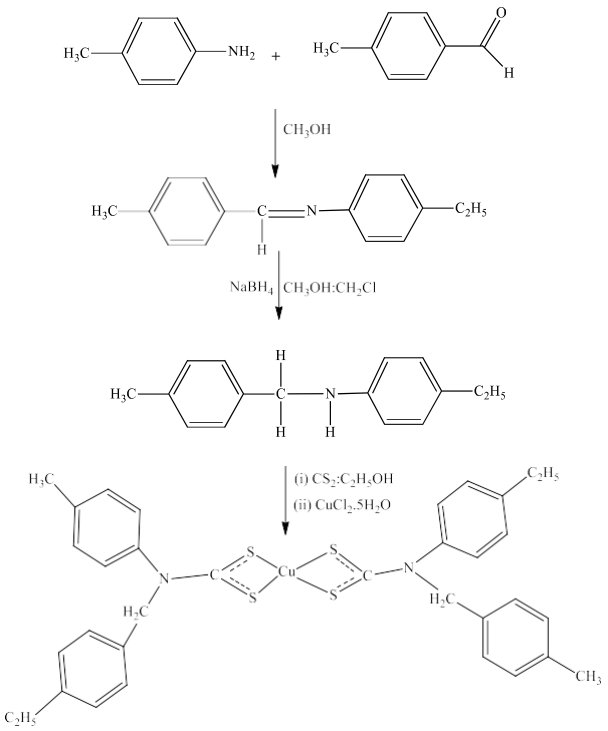

Scheme 3. 1: Preparation of copper(II) bis(N-4-methyl benzyl)-N-(4-ethyl phenyl) dithiocarbamate complex.

Color: purple brown; Yield 65%, mpt 178–180 °C. FTIR (cm^{-1}): ν = 2046 (νNCS); 1457 (νC–N); 1029 (νC–S), 540 (νCu–S), 2985 (ν = C–H), 2931 (ν = C–H), Anal. Calcd. For Chemical Formula: $C_{34}H_{60}N_2S_4Cu$ (688.66 $g.mol^{-1}$): Elemental Analysis: C, 59.30; H, 8.78; N, 4.07; S, 18.62. Found: C, 61.80; H, 5.32; N, 4.45; S, 19.63.

3.1.4 Preparation of copper sulfide nanoparticles

About 0.5 g of the copper dithiocarbamate complex was dispersed in a 100 mL three-necked flask 10 mL containing oleylamine. The mixture was then degassed for 10 min at room temperature by passing nitrogen through the set-up and heated up to 120 ℃. After 1 h, the resultant solution was cooled to room temperature, followed by washing with ethanol and toluene, leading to the precipitation of the nanoparticles. The obtained product was centrifuged and washed severally to isolate the pure nanoparticles and then air-dried. This process was repeated at different reaction temperatures of 150, 180, and 220 ℃ to give a green powder at lower temperatures and black powder and higher temperatures.

3.1.5. Photocatalytic experiment

80 mg of each photocatalyst was introduced into the 200 mL flask containing a 100 mL aqueous solution of 50 mg/L TC in the photocatalytic reactor. After stirring the solution in the dark for 60 min to attain an adsorption-desorption equilibrium between the TC molecules and photocatalysts, the reactor was illuminated with visible light. The process lasted for 120 min. During the experiment, about 5 mL aliquots of the solution were collected at 15 min intervals, centrifuged, and filtered using 0.22 μm PTFE syringe filters (Merck, Burlington, MA, USA). A UV–vis spectrophotometer was used to measure the concentration of the residual TC during the photodegradation process.

3.2.0. Results and discussion

3.2.1 Structural studies

The crystal structure and confirmation of the phase purity of copper sulfide at different temperatures were carried out by XRD analysis and are presented in Figure 3.1. (a)–(c). The XRD patterns showed that, at the lowest synthesis temperature (120 °C), a covellite CuS structure was formed. The pattern matched well with JCPDS No. 06-0464 and conformed well with previous reports on CuS nanostructures [47, 48]. An increase in temperature to 150 °C resulted in the formation of additional peaks at 27.98, 32.38, 46.58, and 55.03º, which were attributed to the (111), (200), (220), and (311) patterns of the nonstoichiometric phase of copper sulfide ($Cu_{7.2}S_4$). At 180 °C, the disappearance of the peaks due to CuS and $Cu_{7.2}S_4$ occurred, and the appearance of peaks ascribed to high-temperature stable-phase digenite (Cu_9S_5)

resulted. However, at this reaction temperature, impurity peaks were observed at 2θ values of 22.57, 27.14, 31.55, and 32.60, which were due to the (101), (102), (110), and (111) patterns of dicopper sulfide (Cu_2S) [49].A further increase to 220 °C gave rise to the pure form of digenite (Cu_9S_5), with peaks assigned to the (101), (0015), (107), (1010), and (0114), which were consistent with the standard values according to JCPDS No. 047-1748 and corresponded to the rhombohedral structure belonging to the space group R3 m[50, 51] (Figure 3.1. (b)). There was no other phase of copper sulfide or any impurity peaks generated at this temperature. The strong and sharp diffraction peaks observed in the XRD patterns as the temperature increased indicated an increase in the crystalline nature of the samples. The absence of any diffraction peaks corresponding to CuO and/or Cu_2S in the XRD pattern of the digenite at this high reaction temperature showed no probable impurities and indicated that high temperature favors the formation of this phase. This temperature-controlled solvothermal synthesis technique confirmed that, by using copper dithiocarbamate, pure-covellite CuS and digenite Cu_9S_5 could easily be synthesized at low and high temperatures, respectively. An earlier report on the preparation of copper sulfide nanocrystals using copper dithiocarbamate as a precursor also showed the formation of mixed phases (Figure 3.1.(c)) at a lower temperature and pure-phase Cu_9S_5 at a higher temperature of synthesis [52] . Because the samples obtained at 150 and 180 ºC resulted in mixed phases, their characterization was not pursued further for both optical- and morphology-based studies.

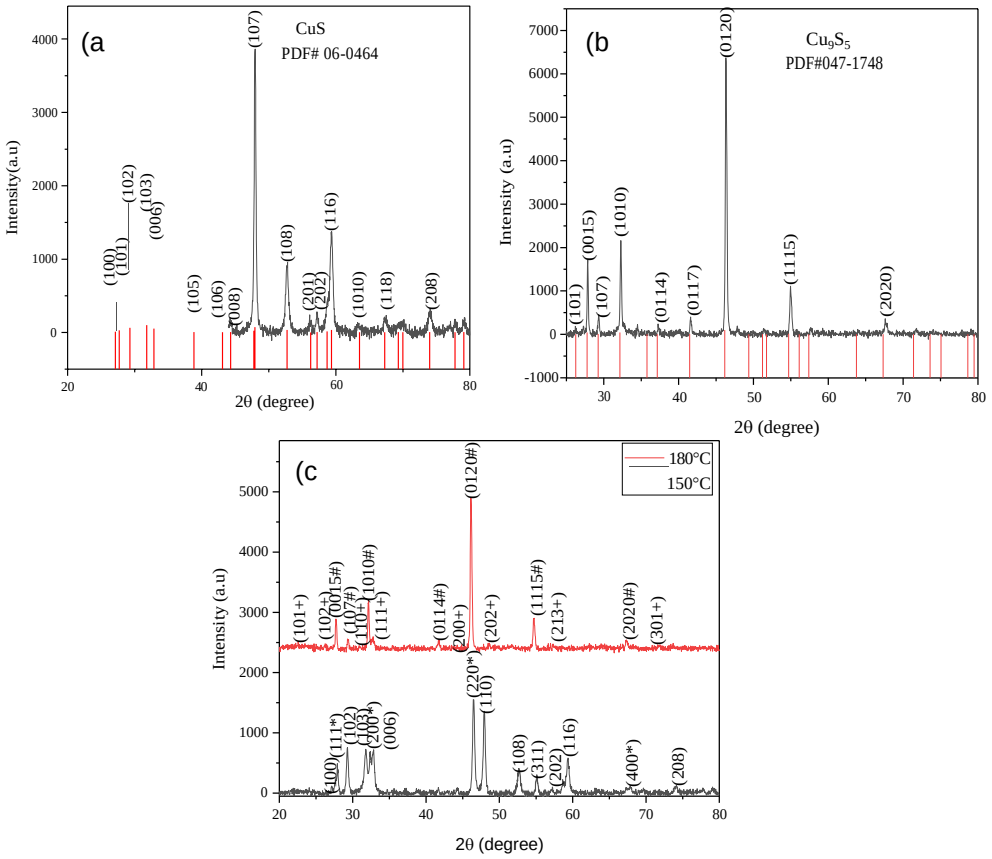

Figure 3. 1: XRD patterns of (a) pure covellite, (b) pure digenite, and (c) mixed phases of copper sulfide ($^{\#}Cu_9S_5$, $^{*}Cu_{7.2}S_4$, and $^{+}Cu_2S$) nanoparticles obtained from the thermolysis of copper(II) dithiocarbamate complex.

The average crystalline sizes of the pure-phase covellite (CuS) and digenite (Cu_9S_5) nanocrystals were determined using the Scherrer equation $d = 0.9\lambda/(\beta \cos \theta)$, where d is the crystalline size, λ is the wavelength of X-ray used for the measurement (1.540598 Å), β is the full width at half maximum using the most intense peak (after the correction of the instrumental broadening) expressed in radians, and θ is the Bragg angle. The values obtained were 24.94 and 32.06 nm for the covellite (CuS) and digenite (Cu_9S_5) nanocrystals, respectively.

3.2.2. SEM and TEM analysis

The surface morphologies of the as-prepared copper sulfide samples were studied by SEM, and the micrographs are presented in Figure 3.2.(a) and (b). The two images demonstrate their morphological differences, with significant differences in their packing and particle distribution. The covellite (CuS) sample consists of spherical and more agglomerated nanoparticles, while the digenite (Cu_9S_5) sample was composed of small rods arranged parallel and fairly distributed across the mat.

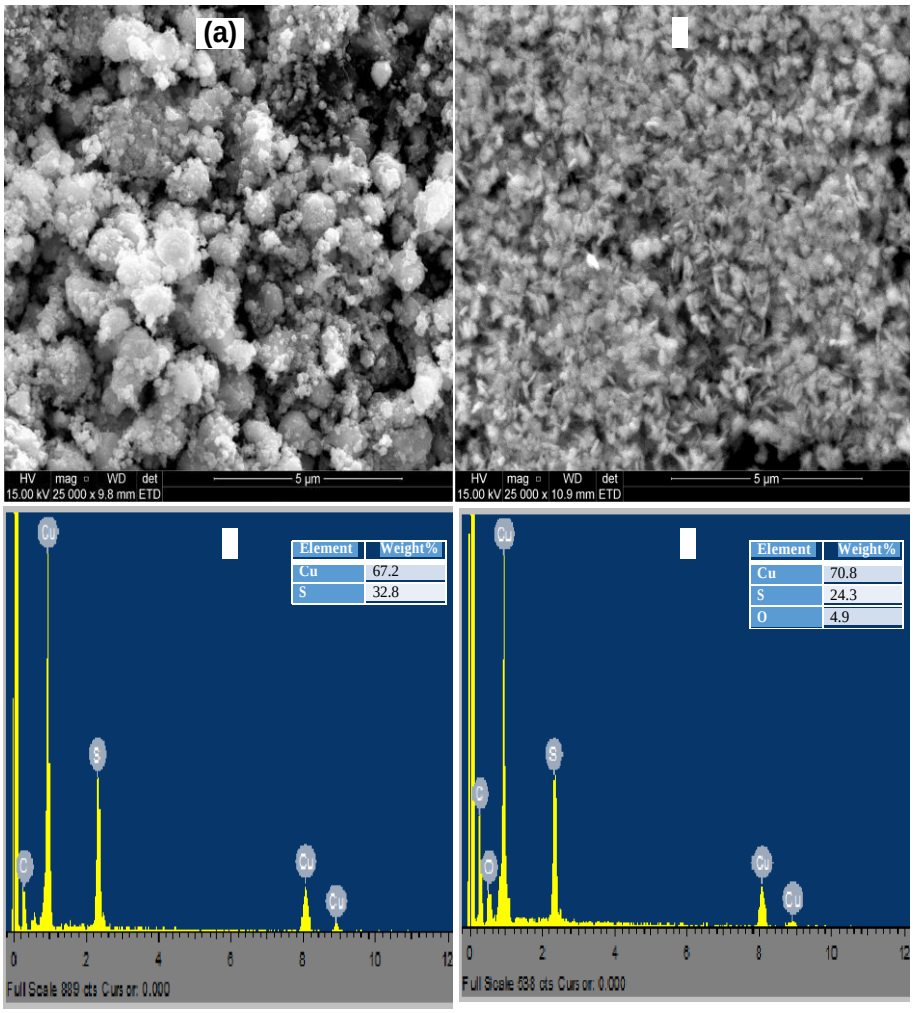

Figure 3. 2: (a) & (b) SEM and (c) & (d) EDX of covellite (CuS) and digenite (Cu_9S_5) nanoparticles respectively

The EDS spectra of both copper sulfides (Figure 3.2. (c),(d)) demonstrated that they mainly comprise Cu and S elements. The weight % of Cu and S estimated for both covellite, and digenite phases are shown as tables in the inset of the respective EDX spectrum. Ideally, the weight % of Cu and S in covellite should be 66.46/33.54%. The table on the insert shows that the estimated values were quite close to the ideal values, with the percentage of Cu being slightly higher than the expected value, similar to an earlier report. This higher percentage of Cu could be attributed to the excessive absorption of copper ions on the surface of nanoparticles [53]. The ideal amount of Cu/S in the digenite phases is 78.10/21.90%, and the EDX spectrum showed the presence of an O atom, which was due to the generation of SO_2 as a byproduct of the oxidation of CuS into Cu_9S_5 [54]. The structural evolution of Cu_9S_5 nanosheets from CuS nanoflowers was reported at 250 °C, with the generation of SO_2 as a byproduct [55].

The TEM micrographs presented in Figure 3.3. (a),(b) conform with the observation in the SEM micrographs. It is apparent that both samples were distinctly different in their morphologies. The covellite CuS in Figure 3.3. (a) shows a cluster of spherical nanoparticles with an average particle size of 24.24 nm, while the digenite Cu_9S_5 presents some stacks of nanorods oriented parallel and with an average length and width of 61.25 and 22.71 nm, respectively, as shown in their particle size distribution histograms in Figure 3.3 (c),(d), respectively.

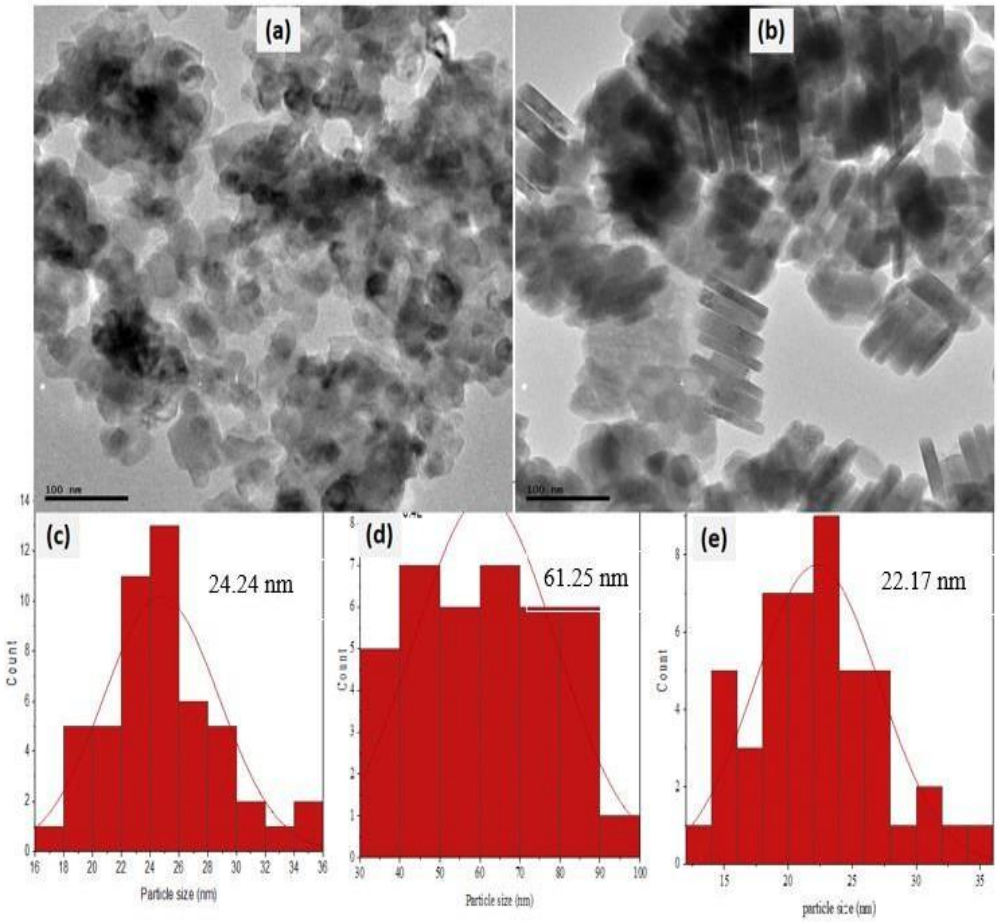

Figure 3. 3: (a) TEM micrographs of covellite (CuS), (b) digenite (Cu_9S_5), particle size distribution histogram of (c) covellite and (d),(e) digenite nanoparticles.

3.2.3.UV–vis and photoluminescence spectra

The absorption spectra of both covellite and digenite are shown in Figure 3.4 (a). The absorption spectrum of the covellite CuS showed a broad absorption from 300 to 600 nm, with a peak around 475 nm, and then gradually increased from around 630 nm into the infrared region. The observed absorption in the range 300–600 nm was attributed to the excitonic absorption of covellite CuS [56], and the absorption that tailed into the infrared region is characteristic of covellite CuS and was due to the interband transitions from the valence states to the unoccupied states [56, 57]. The absorption spectrum of the digenite Cu_9S_5 phase showed a broader absorption from 300 nm and extended into the near-infrared region around 800 nm before increasing gradually beyond 780 nm. The absorption spectra of both samples were similar to previously reported covellite and digenite phases [52, 58].

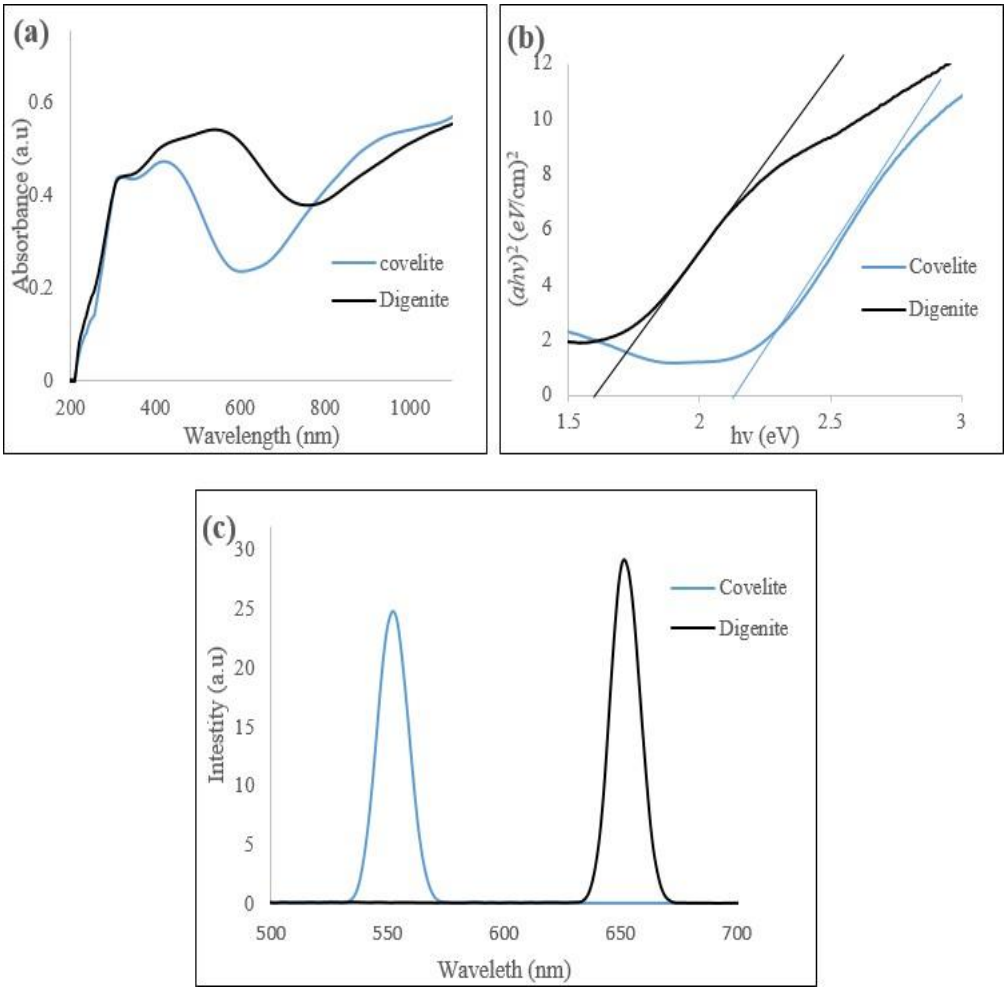

Figure 3. 4:(a) UV-vis-NIR spectra (b) Tauc plot , and (c) photoluminescence spectra of covellite (CuS), (b) digenite (Cu_9S_5), .

The bandgap (Eg) energies could be obtained from the high-frequency region of the spectra by using the Tauc equation $(\alpha h\upsilon)1/m = k\ (h\upsilon - Eg)$ [59]. This involves a plot of $(\alpha h\nu)^2$ versus energy ($h\nu$), where α is the absorption, ν is the frequency, h is a Planck constant, $h\nu$ is the photon energy, m = 2 for a direct energy gap, and m = 1/2 for the indirect gap. The extrapolation of the linear region of the bandgap to the point x = 0 gives the band gap values of the CuS and Cu_9S_5 samples as 2.25 and 1.60 eV, respectively. These values were in the range of the bandgap energies reported earlier [60- 62]

The photoluminescence spectra of both covellite and digenite at room temperature, at an excitation wavelength of 400 and 500 nm, respectively, are shown in Figure 3.4(c). The PL of covellite showed that the nanoparticles had emissions at 554 nm, which could be associated

with the transition that occurred between the electronic states near band edges (i.e., band-to-band transition) [63]. Variation in the emission peak of covellite was observed. While no emission peak was reported for covellite in the range of 400–800 nm [64], Sreelekha *et al*., reported two PL emissions at 417 and 444 nm for CuS prepared by the coprecipitation route [65]. These observations further indicated that the nature and position of the emission spectrum are heavily dependent on the morphology and also the inherent structure of the samples[66, 67]. The photoluminescence spectrum of digenite showed emissions at 650 nm, also suggesting a near band-edge emission. The difference in the spectra obtained could be ascribed to their microstructural and morphological variation, which could influence their electronic transition [68].

3.2.4. Photocatalytic studies

The structure of tetracycline is shown in Figure 3.5. (a), and it consists of two chromophores that are made up of four rings labeled a, b, c, and d [69]. It is an amphoteric molecule with pKa values of 3.3, 7.7, 9.7, and 12[70, 71]. At pH 4, the molecules exist in the neutral and positively charged states (TC^{+}), and as the solution is increased to pH 9, the negatively charged TC molecules become dominant [72]. Figure 3.5(b) presents the absorption spectrum of TC, which showed absorption peaks around 275 and 360 nm. The first absorption peak corresponds to ring (a), while the second peak corresponds to the other aromatic rings (b), (c), and (d) and the developing chromophores. The photolytic degradation of TC has been well studied [73], indicating that the process was distinctly inhibited in the positively charged forms (TC^{+}) and promoted in the negatively charged (TC^{-}) form. The results of other similar studies also showed that the reliance of photolysis on the pH of the solution is related to the protonation states and also the absorbance spectra of other organic pollutants [72]. The effect of pH on the degradation of the TC molecule and also on the shifting of the peak position has been studied. The results showed that at pH 4, the absorbance of TC was relatively lower compared to that at pH 6, indicating that the extinction efficiency of TC^{+} is lower compared to TC^{0}. This observation also indicated that the rate constant of photolysis at pH 4 was lower than that at pH 6. However, a further increase in the pH from 6 to 9 resulted in the increase in the photolysis rate constant, indicative of the low stability of TC at high pH [73]. Yu *et al*., [74] reported that the phenolic, acylamino, and hydroxyl groups of TC remained incompletely degraded by photolysis even after 300 min of simulated light irradiation. The results agreed with previous reports that

photolysis alone is not capable of completely degrading these groups in TC [73]. This further confirmed that the naphthol ring of TC remained intact during photolysis, and only partial mineralization was achieved.

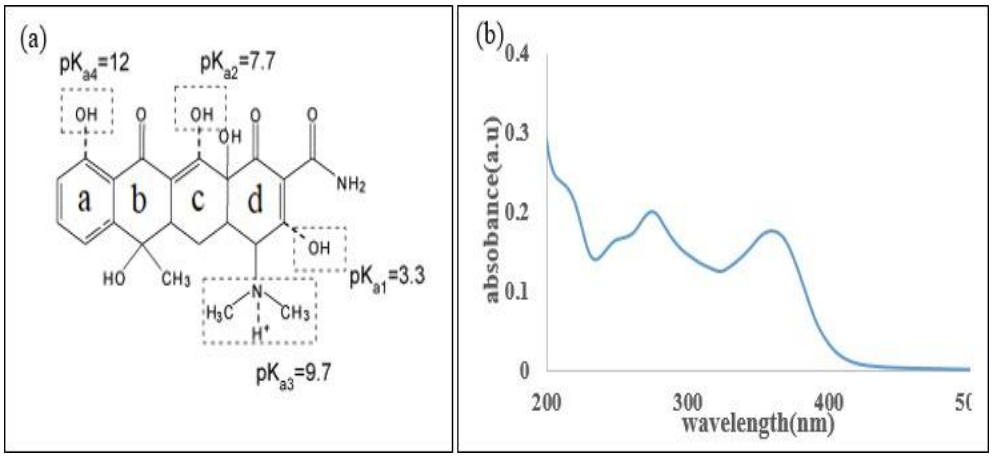

Figure 3. 5: (a) The structure and (b) absorption spectrum of tetracycline (TC).

3.2.5. Dark absorption and photocatalytic performances

The dark adsorption experiment was conducted prior to photodegradation by stirring the mixture of the prepared samples with the TC solution in the dark in order to attain the dark adsorption-desorption equilibrium. The results presented in Figure 3.6 showed that an adsorption equilibrium was reached between the TC solution and the catalyst after 60 min when the samples were taken at 20 min intervals. In addition, the results indicated that less than 20% degradation efficiency of the TC was achieved in the dark adsorption experiment for digenite, while 15% was achieved using covellite as a photocatalyst. Additionally, the adsorption process did not show a significant effect on tetracycline degradation, indicating that dual activities or the mechanism of adsorption and degradation would be required for the total removal of TC from aqueous solution. The adsorption performance of digenite was higher than covellite, similar to previous studies on the degradation of TC [75].

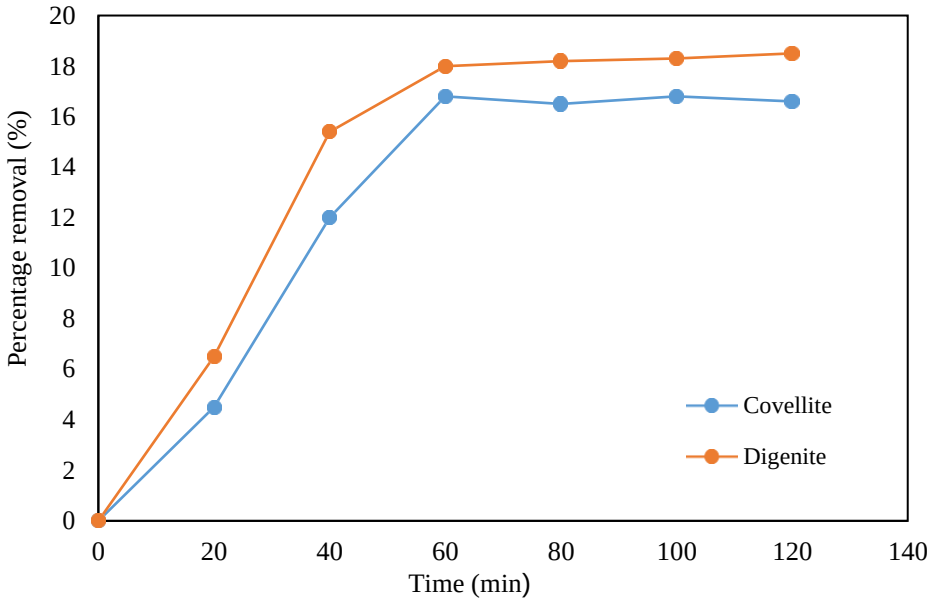

Figure 3. 6: Adsorption equilibrium graph between the TC solution and the photocatalysts (digenite and covellite).

3.2.6.Photocatalytic degradation of TC using digenite and covellite catalysts

The photocatalytic degradation experiments were conducted under visible light (l > 420 nm) using both digenite and covellite separately. Aliquots were taken at 15 min intervals in both cases. Figure 3.7.a,b presents the time-resolved UV–vis spectra during the photodegradation of TC. A decrease in the absorption of TC at the wavelength of 357 nm occurred, accompanied by a shift in the absorption band to a shorter wavelength, which is an indication of the degradation of TC [69]. The main absorption peak corresponding to TC sequentially shifted from 357 to 350 nm, which implied that the degradation of TC occurred gradually, with an increase in contact time, during the photodegradation process. Therefore, a direct relationship between contact time and degradation percentage was observed through the wavelengths. The digenite phase exhibited higher catalytic ability with 98.5% degradation compared to the covellite phase, which showed 88% degradation within the 120 min reaction time using 80 mg of the catalysts. The higher degradation efficiency achieved with the digenite phase might be due to its higher absorption property for light in the visible region, observed in its UV–visible spectrum (Figure 3.4.) compared to the covellite. Hence, it was able to generate more radicals compared to the covellite phase.

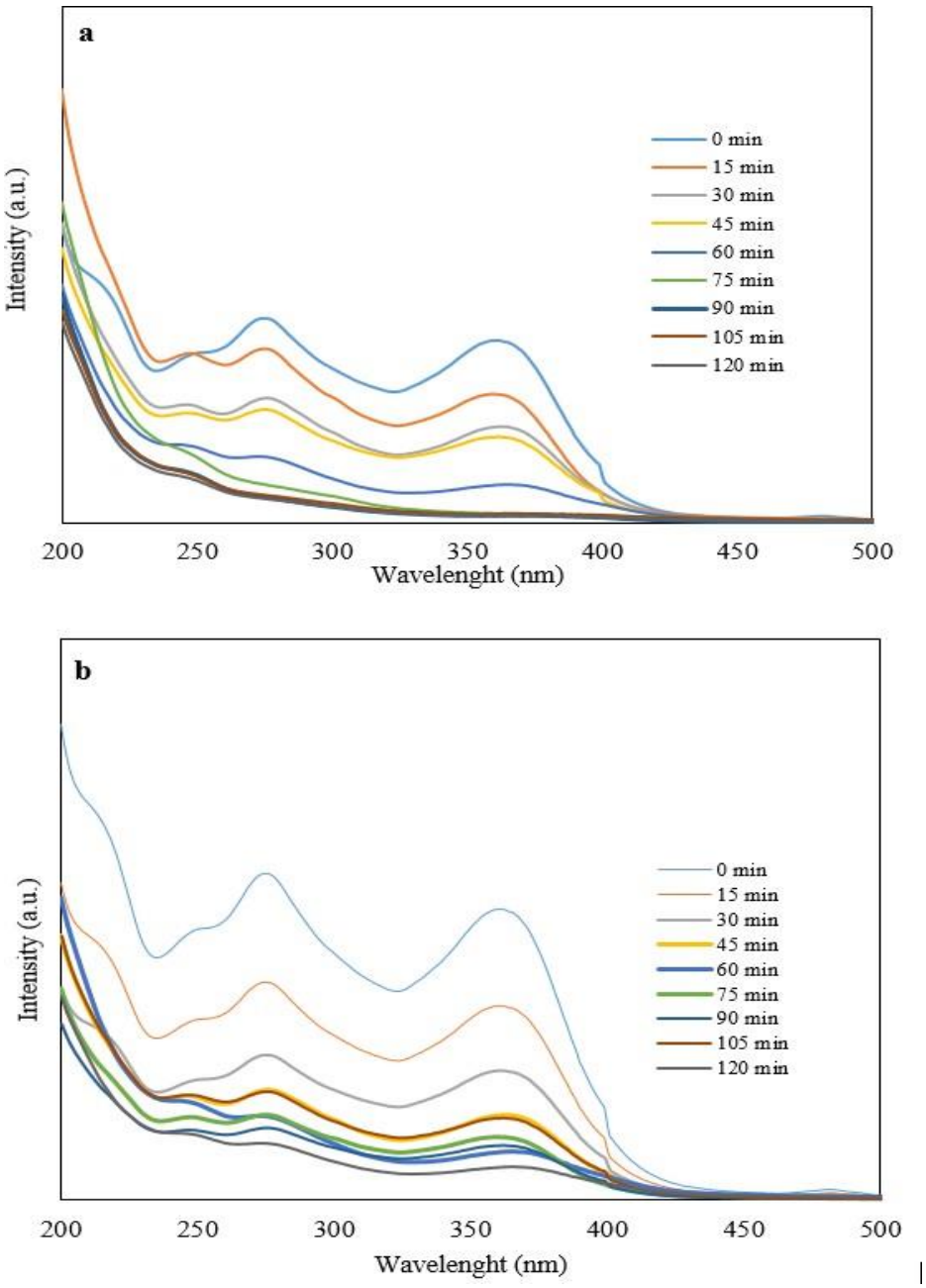

Figure 3. 7: Photocatalytic degradation of tetracycline under visible light irradiation using (a) digenite and (b) covellite phases of copper sulfide

3.2.6. Effect of catalysts loading

The amount of catalyst used in a degradation experiment has a significant effect on the efficiency of the degradation. The degradation study of TC solution was conducted with and

without a photocatalyst under visible light in order to establish the role of the photocatalysts. The results presented in Figure 3.8(a), (b) indicate that little or no degradation of TC occurred prior to the introduction of photocatalyst in both cases. About 5% degradation occurred in the absence of the catalyst after 120 min under visible light. The sharp increase in degradation only started after the introduction of digenite and covellite into the system. The degradation efficiency of TC increased with the catalyst loading up to 80 mg/L, implying a direct relationship between the catalyst loading and the percentage degradation. In addition, photoresponse due to adsorptive degradation is a predominant mechanism for TC removal using both catalysts. Therefore, enhanced degradation achieved with an increase in catalyst loading could be attributed to the increase in the number of active sorption or catalytic sites available on the surface of these catalysts. However, excess catalyst loading above the optimum dosage might cause the scattering of light and a screening effect, which might lead to a reduction in the specific activities of the photocatalysts. The degradation efficiency of 98.5% (Figure 3.8. (a)) was obtained for digenite using 80 mg loading after 120 min, while only 88% (Figure 3.8. (b)) was achieved for covellite using the same operating condition. This could be attributed to both the difference in their bandgap energy and visible-light absorption property. The oxidative potential of materials reduces with a decrease in the bandgap energy, and this may impact the photocatalytic potency of materials[76]. Both digenite and covellite exhibited comparable and highly competitive percentage degradation for TC in the first 110 min of exposure to light. Although covellite has a lower degradation ability owing to less absorption intensity under visible light compared to digenite, more than 80% degradation was achieved after 120 min, which showed that the covellite phase also has good photocatalytic behavior. Nagami *et al*., [77] studied the photocatalytic degradation of TC using cadmium sulfide nanocomposite (CdS/NC-T). About 83% degradation efficiency was obtained with an initial tetracycline concentration of 50 mg/L. Compared to our result, digenite and covellite could be better candidates for the complete removal of TC from water.

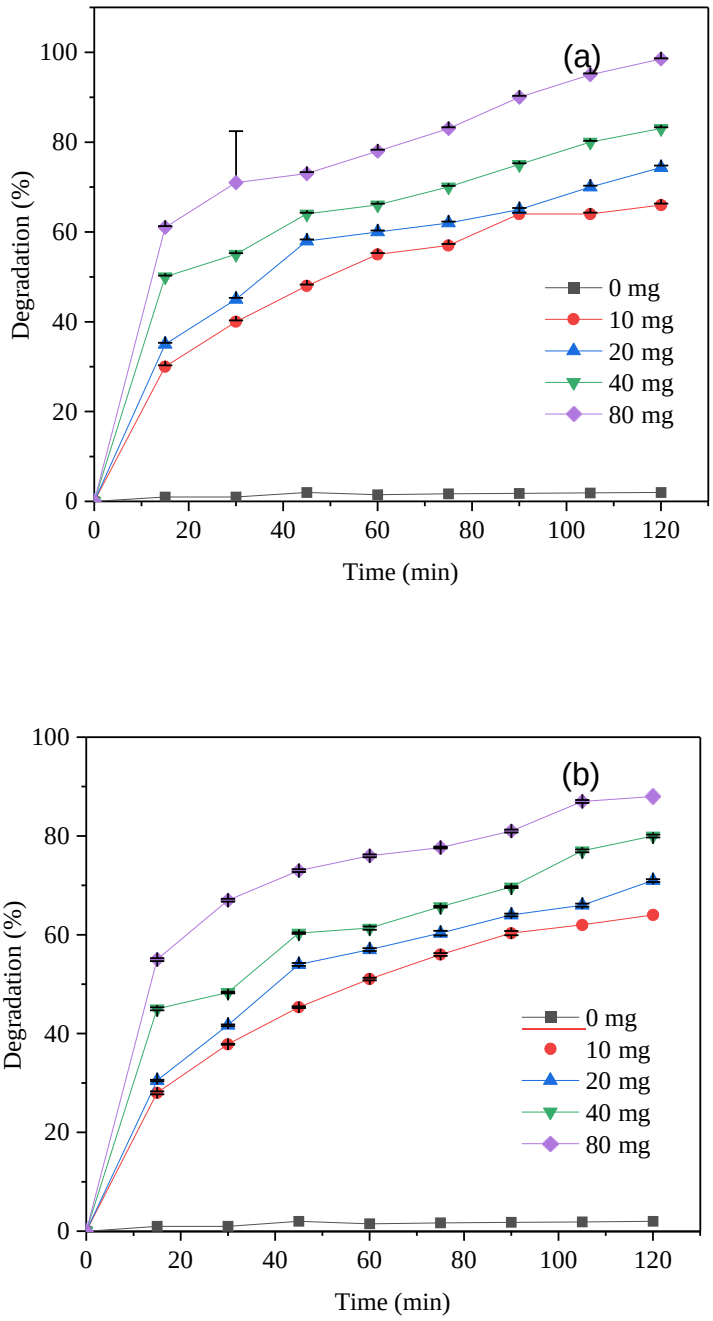

Figure 3. 8: The effect of catalyst loading on the photoreduction of TC on to (a) Digenite (b) covellite.

3.3. Conclusions

A simple, one-pot solvothermal route was utilized to prepare pure-phase hexagonal covellite and rhombohedral digenite nanoparticles, which were characterized by structural, morphological, and optical techniques. The phase transformation from covellite to digenite was accompanied by the formation of mixed phases of $Cu_{7.2}S_4$ and Cu_2S at 150 and 180 ºC, in addition to a morphological transformation from spherical- to rod-shaped structures. The pure phases were further used to affect the photodegradation of tetracycline in an aqueous solution. The digenite phase exhibited higher catalytic degradation of 98.5% compared to the covellite phase, which showed 88% degradation within the 120 min reaction time using 80 mg of the catalysts. A study of the effect of the concentration of copper sulfide on the photocatalytic properties showed that the activity not only depended on their phases but also strongly depended on the dosage of the catalyst used. This study provides a simple strategy for the preparation of different phases of copper sulfide with a low cost and improved photocatalytic activity.

3.4.0. References

1. Senthilkumar, M. and S.M. Babu, *Synthesis and characterization of hexagonal faceted copper sulfide ($Cu_{1.8}S$) nanodisks.* Materials Science in Semiconductor Processing, 2015. **40**: p. 203-208.

2. Zheng, L., *et al.*, *Photo/electrochemical applications of metal sulfide/TiO_2 heterostructures.* Advanced Energy Materials, 2020. **10**(1): p. 1902355.

3. Botha, N.L. and P.A. Ajibade, *Effect of temperature on crystallite sizes of copper sulfide nanocrystals prepared from copper (II) dithiocarbamate single source precursor.* Materials Science in Semiconductor Processing, 2016. **43**: p. 149-154.

4. Wang, Y., *et al.*, *One-pot synthesis and optical property of copper (I) sulfide nanodisks.* Inorganic chemistry, 2010. **49**(14): p. 6601-6608.

5. Tian, Q., *et al.*, *Hydrophilic Cu_9S_5 nanocrystals: a photothermal agent with a 25.7% heat conversion efficiency for photothermal ablation of cancer cells in vivo.* ACS nano, 2011. **5**(12): p. 9761-9771.

6. Abdelhady, A.L., M.A. Malik, and P. O'Brien, *High-throughput route to $Cu_{2-x}S$ nanoparticles from single molecular precursor.* Materials science in semiconductor processing, 2012. **15**(2): p. 218-221.

7. Ghahremaninezhad, A., E. Asselin, and D. Dixon, *Electrodeposition and growth mechanism of copper sulfide nanowires.* The Journal of Physical Chemistry C, 2011. **115**(19): p. 9320-9334.

8. Yoon, D., *et al.*, *Scalable synthesis of djurleite copper sulfide ($Cu_{1.94}S$) hexagonal nanoplates from a single precursor copper thiocyanate and their photothermal properties.* CrystEngComm, 2015. **17**(25): p. 4627-4631.

9. Zhang, H., et al., *Phase-selective synthesis and self-assembly of monodisperse copper sulfide nanocrystals.* The Journal of Physical Chemistry C, 2008. **112**(35): p. 13390-13394.

10. Whiteside, L.S. and R.J. Goble, *Structural and compositional changes in copper sulfide during leaching and dissolution.* The Canadian Mineralogist, 1986. **24**(2): p. 247-258.

11. Senthilkumar, M., *et al*., *Ligand assisted tunability of morphological and optical properties of copper sulfide nanocrystals.* Materials Science in Semiconductor Processing, 2019. **104**: p. 104685.

12. Liu, Y., M. Liu, and M.T. Swihart, *Reversible crystal phase interconversion between covellite CuS and high chalcocite Cu_2S nanocrystals.* Chemistry of Materials, 2017. **29**(11): p. 4783-4791.

13. Liao, X.-H., *et al.*, *A microwave assisted heating method for the preparation of copper sulfide nanorods.* Journal of Crystal Growth, 2003. **252**(4): p. 593-598.

14. Mu, C.-F., *et al*., *Controlled synthesis of various hierarchical nanostructures of copper sulfide by a facile microwave irradiation method.* Colloids and Surfaces A: Physicochemical and Engineering Aspects, 2010. **371**(1-3): p. 14-21.

15. Jia, B., *et al*., *Synthesis, characterization, shape evolution, and optical properties of copper sulfide hexagonal bifrustum nanocrystals.* Journal of nanoparticle research, 2013. **15**(3): p. 1-9.

16. Chen, L., W. Yu, and Y. Li, *Synthesis and characterization of tubular CuS with flower-like wall from a low temperature hydrothermal route.* Powder Technology, 2009. **191**(1-2): p. 52-54.

17. Phuruangrat, A., T. Thongtem, and S. Thongtem, *Characterization of copper sulfide hexananoplates, and nanoparticles synthesized by a sonochemical method.* Chalcogenide Lett, 2011. **8**: p. 291-295.

18. Singh, A., R. Manivannan, and S.N. Victoria, *Simple one-pot sonochemical synthesis of copper sulfide nanoparticles for solar cell applications.* Arabian Journal of Chemistry, 2019. **12**(8): p. 2439-2447.

19. Cheng, Z., *et al*., *Controlled synthesis of copper sulfide 3D nanoarchitectures through a facile hydrothermal route.* Journal of alloys and compounds, 2010. **492**(1-2): p. L44-L49.

20. Li, J., *et al*., *In situ fabricate Cu2S thin film with hierarchical petal-like nanostructures.* Materials Research Bulletin, 2013. **48**(8): p. 2940-2943.

21. Coughlan, C., *et a*l., *Compound copper chalcogenide nanocrystals.* Chemical reviews, 2017. **117**(9): p. 5865-6109.

22. Ajibade, P.A. and N.L. Botha, *Synthesis and structural studies of copper sulfide nanocrystals.* Results in physics, 2016. **6**: p. 581-589.

23. Dhasade, S., *et al*., *Copper sulfide nanorods grown at room temperature for photovoltaic application.* Materials Letters, 2013. **90**: p. 138-141.

24. Ke, H., *et al*., *Synthesis of flower-like CuS nanostructured microspheres using poly (ethylene glycol) 200 as solvent.* Journal of nanoscience and nanotechnology, 2010. **10**(11): p. 7770-7773.

25. Das, G., et al., *Water soluble sodium sulfate nanorods as a versatile template for the designing of copper sulfide nanotubes.* Journal of nanoscience and nanotechnology, 2014. **14**(6): p. 4455-4461.

26. Lim, W.P., *et al*., *Phase-selective synthesis of copper sulfide nanocrystals.* Chemistry of materials, 2006. **18**(26): p. 6170-6177.

27. Du, W., *et al*., *Shape-Controlled Synthesis and Self-Assembly of Hexagonal Covellite (CuS) Nanoplatelets.* Chemistry–A European Journal, 2007. **13**(11): p. 3241-3247.

28. Zhang, P. and L. Gao, *Copper sulfide flakes and nanodisks.* Journal of Materials Chemistry, 2003. **13**(8): p. 2007-2010.

29. Du, Y., *et al*., *A general method for the large-scale synthesis of uniform ultrathin metal sulfide nanocrystals.* Nature communications, 2012. **3**(1): p. 1-7.

30. Zhu, H., *et al*., *Novel CuS hollow spheres fabricated by a novel hydrothermal method.* Microporous and mesoporous materials, 2005. **80**(1-3): p. 153-156.

31. Wu, S., *et al.*, *Visible light photocatalytic degradation of tetracycline over TiO_2.* Chemical Engineering Journal, 2020. **382**: p. 122842.

32. Leng, Y., *et al*., *Transformation mechanisms of tetracycline by horseradish peroxidase with/without redox mediator ABTS for variable water chemistry.* Chemosphere, 2020. **258**: p. 127306.

33. Rizzi, V., *et al*., *Removal of tetracycline from polluted water by chitosan-olive pomace adsorbing films.* Science of The Total Environment, 2019. **693**: p. 133620.

34. Zhang, Z., *et al*., *Efficient removal of tetracycline hydrochloride from aqueous solution by mesoporous cage MOF-818.* SN Applied Sciences, 2020. **2**(4): p. 1-11.

35. Wu, K., *et al*., *The removal of tetracycline, oxytetracycline, and chlortetracycline by manganese oxide-doped copper oxide: the behaviors and insights of Cu-Mn combination for enhancing antibiotics removal.* Environ Sci Pollut Res Int, 2020. **27**(11): p. 12613-12623.

36. Smilack, J.D. *The tetracyclines*. in *Mayo Clinic Proceedings*. 1999. Elsevier.

37. Græsbøll, K., et al., *Effect of tetracycline treatment regimens on antibiotic resistance gene selection over time in nursery pigs.* BMC microbiology, 2019. **19**(1): p. 1-10.

38. Garrett, J.P. and D.J. Margolis, *Impact of long-term antibiotic use for acne on bacterial ecology and health outcomes: a review of observational studies.* Current Dermatology Reports, 2012. **1**(1): p. 23-28.

39. Miao, J., *et al*., *The adsorption performance of tetracyclines on magnetic graphene oxide: A novel antibiotics absorbent.* Applied Surface Science, 2019. **475**: p. 549-558.

40. Gao, Y., *et al*., *Adsorption and removal of tetracycline antibiotics from aqueous solution by graphene oxide.* Journal of colloid and interface science, 2012. **368**(1): p. 540-546.

41. Zhao, C., *et al*., *Removal of tetracycline from water using activated carbon derived from the mixture of phragmites australis and waterworks sludge.* ACS omega, 2020. **5**(26): p. 16045-16052.

42. Saitoh, T., *et al*., *Rapid removal of tetracycline antibiotics from water by coagulation-flotation of sodium dodecyl sulfate and poly (allylamine hydrochloride) in the presence of Al (III) ions.* Separation and Purification Technology, 2017. **187**: p. 76-83.

43. Jeong, J., *et al*., *Degradation of tetracycline antibiotics: mechanisms and kinetic studies for advanced oxidation/reduction processes.* Chemosphere, 2010. **78**(5): p. 533-540.

44. Guo, J., *et al*., *Photocatalytic degradation of tetracycline antibiotics using delafossite silver ferrite-based Z-scheme photocatalyst: Pathways and mechanism insight.* Chemosphere, 2021. **270**: p. 128651.

45. Vu, T.H., *et al*., *Removal of Tetracycline from Aqueous Solution Using Nanocomposite Based on Polyanion-Modified Laterite Material.* Journal of Analytical Methods in Chemistry, 2020. **2020**.

46. Sathiyaraj, E., *et al*., *Synthesis and characterization of Ni (II) complexes with functionalized dithiocarbamates: New single source precursors for nickel sulfide and nickel-iron sulfide nanoparticles.* Inorganica Chimica Acta, 2019. **498**: p. 119162.

47. Ji, H., *et al*., *Fabrication of CuS nanocrystals with various morphologies in the presence of a nonionic surfactant.* Materials Letters, 2005. **59**(24-25): p. 3169-3172.

48. Rajendran, V. and J. Gajendiran, *Nonionic surfactant poly (ethane 1, 2-diol)-400 assisted solvothermal synthesis of copper monosulfide (CuS) nanoplates and their structural, topographical, optical and luminescent properties.* Materials Science in Semiconductor Processing, 2015. **36**: p. 92-95.

49. Yadav, S. and P. Bajpai, *Synthesis of copper sulfide nanoparticles: pH dependent phase stabilization.* Nano-Structures & Nano-Objects, 2017. **10**: p. 151-158.

50. Leidinger, P., et al., *Nanoscale copper sulfide hollow spheres with phase-engineered composition: covellite (CuS), digenite ($Cu_{1.8}S$), chalcocite (Cu_2S).* Nanoscale, 2011. **3**(6): p. 2544-2551.

51. Sithole, R.K., et al., *One-step synthesis of Cu_3N, Cu_2S and Cu_9S_5 and photocatalytic degradation of methyl orange and methylene blue.* Journal of Photochemistry and Photobiology A: Chemistry, 2020. **397**: p. 112577.

52. Olatunde, O.C. and D.C. Onwudiwe, *Temperature Controlled Evolution of Pure Phase Cu_9S_5 Nanoparticles by Solvothermal Process.* Frontiers in Materials, 2021. **8**: p. 211.

53. Yadav, S., K. Shrivas, and P. Bajpai, *Role of precursors in controlling the size, shape and morphology in the synthesis of copper sulfide nanoparticles and their application for fluorescence detection.* Journal of Alloys and Compounds, 2019. **772**: p. 579-592.

54. Iqbal, S., *et al*., *Extensive evaluation of changes in structural, chemical and thermal properties of copper sulfide nanoparticles at different calcination temperature.* Journal of Crystal Growth, 2020. **547**: p. 125823.

55. Tao, F., *et al*., *Structural evolution from CuS nanoflowers to Cu_9S_5 nanosheets and their applications in environmental pollution removal and photothermal conversion.* RSC advances, 2016. **6**(68): p. 63820-63826.

56. Hosseinpour, Z., *et al.*, *A controlled solvothermal synthesis of CuS hierarchical structures and their natural-light-induced photocatalytic properties.* New Journal of Chemistry, 2015. **39**(7): p. 5470-5476.

57. Zhao, Y., et al., *Plasmonic $Cu_{2-x}S$ nanocrystals: optical and structural properties of copper-deficient copper (I) sulfides.* Journal of the American Chemical Society, 2009. **131**(12): p. 4253-4261.

58. Jiang, J., *et al.*, *Controllable preparation, formation mechanism and photocatalytic performance of copper base sulfide nanoparticles.* Materials Chemistry and Physics, 2020. **254**: p. 123504.

59. Tauc, J., *Optical properties and electronic structure of amorphous Ge and Si.* Materials Research Bulletin, 1968. **3**(1): p. 37-46.

60. Kundu, J. and D. Pradhan, *Controlled synthesis and catalytic activity of copper sulfide nanostructured assemblies with different morphologies.* ACS applied materials & interfaces, 2014. **6**(3): p. 1823-1834.

61. Santos Cruz, J., *et al.*, *Optical and electrical properties of thin films of CuS nanodisks ensembles annealed in a vacuum and their photocatalytic activity.* International Journal of Photoenergy, 2013. **2013**.

62. Senthilkumar, M. and S.M. Babu. *Crystal structure controlled synthesis and characterization of copper sulfide nanoparticles*. in *AIP Conference Proceedings*. 2016. AIP Publishing LLC.

63. Shi, J., *et al.*, *Sonochemical synthesis of CuS/reduced graphene oxide nanocomposites with enhanced absorption and photocatalytic performance.* Materials Letters, 2014. **126**: p. 220-223.

64. Jiang, X., *et al.*, *Preparation and phase transformation of nanocrystalline copper sulfides (Cu9S8, Cu7S4 and CuS) at low temperature.* Journal of Materials Chemistry, 2000. **10**(9): p. 2193-2196.

65. Sreelekha, N., *et al.*, *Structural, optical, magnetic and photocatalytic properties of Co doped CuS diluted magnetic semiconductor nanoparticles.* Applied Surface Science, 2016. **378**: p. 330-340.

66. Kalyanikutty, K., et al., *Hydrogel-assisted synthesis of nanotubes and nanorods of CdS, ZnS and CuS, showing some evidence for oriented attachment.* Chemical Physics Letters, 2006. **432**(1-3): p. 190-194.

67. Wang, X.-y., Z. Fang, and X. Lin, *Copper sulfide nanotubes: facile, large-scale synthesis, and application in photodegradation.* Journal of Nanoparticle Research, 2009. **11**(3): p. 731-736.

68. Zhang, F. and S.S. Wong, *Controlled synthesis of semiconducting metal sulfide nanowires.* Chemistry of materials, 2009. **21**(19): p. 4541-4554.

69. Wessels, J., *et al*., *The complexation of tetracycline and anhydrotetracycline with Mg^{2+} and Ca^{2+}: a spectroscopic study.* The Journal of Physical Chemistry B, 1998. **102**(46): p. 9323-9331.

70. Jin, L., et al., *Ca^{2+} and Mg^{2+} bind tetracycline with distinct stoichiometries and linked deprotonation.* Biophysical chemistry, 2007. **128**(2-3): p. 185-196.

71. Figueroa, R.A., A. Leonard, and A.A. MacKay, *Modeling tetracycline antibiotic sorption to clays.* Environmental science & technology, 2004. **38**(2): p. 476-483.

72. Boreen, A.L., W.A. Arnold, and K. McNeill, *Photochemical fate of sulfa drugs in the aquatic environment: sulfa drugs containing five-membered heterocyclic groups.* Environmental Science & Technology, 2004. **38**(14): p. 3933-3940.

73. Jiao, S., *et al*., *Aqueous photolysis of tetracycline and toxicity of photolytic products to luminescent bacteria.* Chemosphere, 2008. **73**(3): p. 377-382.

74. Yu, X., *et al*., *Effective photodegradation of tetracycline by narrow-energy band gap photocatalysts La2-xSrxNiMnO6 (x= 0, 0.05, 0.10, and 0.125).* Journal of Alloys and Compounds, 2019. **806**: p. 451-463.

75. Minallah, S., *et al.*, *Ternary adsorbent photocatalyst hybrid (APH) nanomaterials for improved abstraction of tetracycline from water.* Separation Science and Technology, 2020. **55**(15): p. 2623-2641.

76. Lou, Y., *et al*., *Femtosecond spectroscopic investigation of the carrier lifetimes in digenite quantum dots and discrimination of the electron and hole dynamics via ultrafast interfacial electron transfer.* The Journal of Physical Chemistry B, 2003. **107**(45): p. 12431-12437.

77. Nagamine, M., *et al*., *Tetracycline photocatalytic degradation under CdS treatment.* Journal of Marine Science and Engineering, 2020. **8**(7): p. 483.

Chapter 4

Photocatalytic degradation of tetracycline in aqueous solution using copper sulfide nanoparticles

4.0. Introduction

Antibiotics are generally used to prevent and treat microbial infections by either killing or inhibiting their growth. They are important for the control, prevention, and treatment of diseases in both humans and animals. In most developed nations, for example, it is estimated that livestock alone consumes between 50–80 % of antibiotics produced [1]. They could be divided into aminoglycosides, quinolone, sulfonamides, macrolides, and tetracycline based on their structures [2]. The misuse of antibiotics has a huge negative impact on environmental contamination, especially on soil and water resources. Some traces of antibiotics have been detected in sewage, ground, surface, and drinking water [3, 4]. The presence of antibiotics in the environment could result in the development of their resistance in microorganisms [5, 6], and tetracycline (TC) has been reported as one of the most widely used antibiotics [7].

TC is an amphoteric compound, which contains four connected rings consisting of different active functional groups, including alcohol, aldehyde, and phenol, with three ionizable groups-tricarbonylamide, dimethylamino, and phenolic-diketone groups. This allows TC to ionize with three dissociation constants of pKa 3.3, 7.7, and 9.7. Thus, it exists as anionic, cationic, and zwitterionic species under alkaline, acidic, and moderately acidic to neutral conditions, respectively [8, 9]. It is widely used in humans to treat bacterial infections and also in animal feed as a growth promoter [10]. Most of the administrated TC are relatively poorly adsorbed by animals or humans; therefore, their metabolites are excreted through faeces and urine into the environment. Once in the environment, they can lead to the development of multi-resistant bacterial strains which cannot be treated with the common known drugs [11, 12]. This possible risk makes it of great importance to explore feasible and cost-effective treatment for the removal of TC.

The removal of TC from water by different methods such as adsorption [13, 14], biological [15], and chemical degradation has been studied. However, their high cost and low removal efficiency usually limit their applications. Photocatalysis is a promising technique due to its low cost and efficiency. Different semiconductor nanomaterials have been used as photocatalysts either in their pure forms or as a composite to affect the degradation of TC. For example, TiO_2 [16], g-C_3N_4 [17], ZnS[18], and $BiVO_4$[19] have been used to achieve the removal of TC from an aqueous solution. The use of binary composites such as MWCNT/TiO_2 [20] Ag/TiO_2 [21] Sr-Bi_2O_3 [22] TiO_2 - SiO_2 [23] and ZnO/γ-Fe_2O_3 [24] or ternary composites including MGO-Ce-TiO_2 [25] CeO_2/ $Bi_2O_2CO_3$ [26], Ag/Ag_2CO_3/$BiVO_4$ [27] and IO-TiO_2-CdS[28] have also been reported . However, due to some demerits associated with some of these materials, such as high cost, economical non-viability, and poor efficiency, there is a need to explore other semiconductors. For example, despite the great advantages of TiO_2, its shortcomings include activation within the UV range only (due to a large bandgap of 3-3.2 eV), fast recombination between electron-hole pairs and a high tendency for agglomeration, modification of TiO_2 before its use as photocatalyst is one of the methods used to address thus shortcoming. Consequently, nontoxic semiconductor nanomaterials such as copper sulfide that is relatively cheap, and has good light absorption properties over a wide range of wavelengths, and exhibits different crystalline phases[29] that could open up wide areas of application, is a good alternative. Compared with other semiconductor materials, copper sulfide has not been explored in the photocatalytic degradation of TC.

Copper sulfide is a p-type indirect band-gap semiconductor material and occupies a very significant position within the family of compound semiconductors. The p-type conduction property is ascribed to the free holes, which are generated from the acceptor levels of copper vacancies [30]. It is reported to exhibit size-dependent properties that are similar to the widely explored lead and cadmium systems and has the advantage of being a non-toxic material. In addition, the earth's abundant nature of its component elements makes it a very promising candidate for the fabrication of devices [31]. Another interesting property of copper sulfide is its existence in variable stoichiometries. This makes it a very interesting compound for fundamental studies, possessing different bandgap energies and electronic properties. The different stoichiometric phases of copper sulfide range from the copper-rich phases: chalcocite (Cu_2S), djurleite ($Cu_{31}S_{16}$ or $Cu_{1.94}S$), digenite (Cu_9S_5 or $Cu_{1.8}S$), and anilite/roxbyite (Cu_7S_4 or $Cu_{1.75}S$) to the copper-poor phases: covellite (CuS) and villamaninite (CuS_2) [30, 32]. The

variation in stoichiometry also influences their band gap energy. For instance, while the chalcocite has an indirect bulk band gap energy of ~1.2 eV, the digenite phase possesses a band gap of 1.5 eV [33], and this is favorable for the absorption of light under sunlight illumination.

The synthesis of well-defined pure phase colloidal copper sulfide is a challenge, and the very close relationship that exists between properties and shapes implies that tailoring of the morphology of nanostructures is critical in the synthesis of desired materials with specific properties. Herein, a facile solvothermal method is reported for the synthesis of pure djurleite and roxbyite phases using copper(II) dithiocarbamate (CuDTC) as a single-source precursor and dodecanthiol (DDT) as surfactants. CuDTC was utilized as the single-source precursor due to its ease of preparation, good stability, and ability to undergo sharp decomposition with less impurity. By changing the reaction temperature during the decomposition process of the complex, it was possible to alter the nucleation and growth process of the copper sulfide nanoparticles, thereby manipulating their optical and structural properties. The as-prepared copper sulfides were air-stable; hence the obtained pure phases of djurleite ($Cu_{31}S_{16}$) and roxbyite (Cu_7S_5) were used as photocatalysts for the degradation of tetracycline in aqueous solution.

4.1.0. Material and methods

4.1.1. Preparation of Copper Dithiocarbamate Complex

The copper complex was prepared using an already reported procedure [34]. Briefly, a methanol solution featured an equimolar ratio of 4-ethylaniline and p-tolualdehyde (4.0 mmol) mixed together and stirred at room temperature for 2 h. Thereafter, the solvent was removed, and the resulting oily product was dissolved in an equal volume solution of methanol and dichloromethane. Sodium borohydride was added and stirred for another 2 h in ice, and the solution was stirred for 20 h at room temperature, which was followed by the removal of the solvent. The product was rinsed with water and extracted with dichloromethane. Then, the organic layer was evaporated to afford the substituted amine as a brownish oil, which was dissolved in ethanol and followed by the addition of potassium hydroxide. The solution was stirred for 30 min, and carbon disulfide was added dropwise while maintaining the temperature for 2 h. To this solution, a stoichiometric amount of copper(II) chloride dihydrate was added, and the resulting copper dithiocarbamate precipitates were rinsed using cold water and then air-dried.

4.1.2. Preparation of copper sulfide nanoparticles

Copper sulfide nanoparticles were prepared via a solvothermal reaction under N_2 atmosphere using the heat-up method. In a round bottom flask with a condenser, 0.75 g of copper(II) bis(*N*-4-methyl benzyl)-*N*-(4-ethyl phenyl) dithiocarbamate was added into 20 mL of dodecanthiol. After degassing, the mixture was heated at a steady temperature up to 120 °C and maintained for 1 h. afterward, the dark solution was left to cool down to room temperature. The obtained product was then separated by the addition of ethanol and centrifugation. To purify the product, ethanol and toluene (1:3 v/v) were used to wash the product 3 times. The procedure was repeated while the temperature of the reaction was changed to 150, 180, 220, and 250 °C, respectively.

4.1.3. Characterization of the prepared samples

The X-ray powder diffraction data were collected on a Bruker D8 Advanced, which utilizes CuKα radiation (wavelength, λ = 1.5406 Å) with variable slits at 45 kV/40 mA. Scanning electron microscope (SEM) measurement was carried out on JOEL JSM-6390 LVSEM, fitted with an energy dispersive X-ray spectrometer (EDX) for the elemental analysis of the samples. The internal morphology of the nanoparticles was studied using a TECNAI G2 (ACI) TEM equipped with a CCD Camera and operating at a voltage of 120 kV. The optical properties of the nanoparticles were studied using a Jobin Yvon LabRAM HR 800 UV/Vis/NIR spectrophotometer and a Perkin Elmer L45 photoluminescence spectrometer for the absorption and fluorescence measurement.

4.1.5. Photocatalytic evaluation

In the photocatalytic experiment, a LED visible light lamp ((l > 420 nm) was used as the light source. Firstly, about 80 mg of each catalyst was added to 100 mL of TC solution containing 50 mg/L TC in 200 mL flask and magnetically stirred the solution in the dark for 60 min in order to achieve adsorption-desorption equilibrium. The light source was then turned on in order to initiate the photocatalytic reaction. As the reaction progressed, approximately 5 mL of suspension was collected every 15 min, filtered through a 0.22 μm PTFE syringe filter. The obtained clear solution was introduced into a quartz cuvette, and the absorbance of the TC was measured using an ultraviolet-visible spectrophotometer. The concentration of the TC degraded was calculated using the formula given in Eq. (1).

$$DR(\%) = \frac{C_0 - C_i}{C_0} \times 100\% = \frac{A_0 - A_i}{A_0} \times 100(\%) \quad (1)$$

where, C_i is the concentration of TC at different times; C_0 is the initial concentration of TC; A_i is the TC absorbance at different times, and A_0 is the blank absorbance of the original TC solution).

4.2.0. Results and discussion

4.2.1. Structural studies

The phase structures of the as-synthesized nanoparticles at different reaction temperatures were investigated using XRD and presented in Figure 4.1. The temperature of synthesis of copper sulfide determines the composition and stoichiometry. In the samples obtained at 120 and 150 ºC, the peaks at 2θ = 37.53, 46.31, 48.63, and 54.22º correspond to the (-4 2 5), (10 5 2), (-2 8 2), and (2 6 6) planes, respectively, of monoclinic djurleite $Cu_{31}S_{16}$ with space group of P21/n (14) (JCPDS No. 034-0660) [35]. Our previous report involving the same complex but in oleylamine as solvent yielded pure phase covellite at lower temperature and digenite at higher temperature [36]. Similar studies involving the thermal decomposition of Bis(*O*-alkylxanthato)copper(II) in oleylamine showed the formation of djurleite ($Cu_{31}S_{16}$) phase as either impurity phase or as the secondary phase. The results further showed the dependence of copper sulfide phases on the factors such as precursor type, growth temperature, and synthesis method used [34].

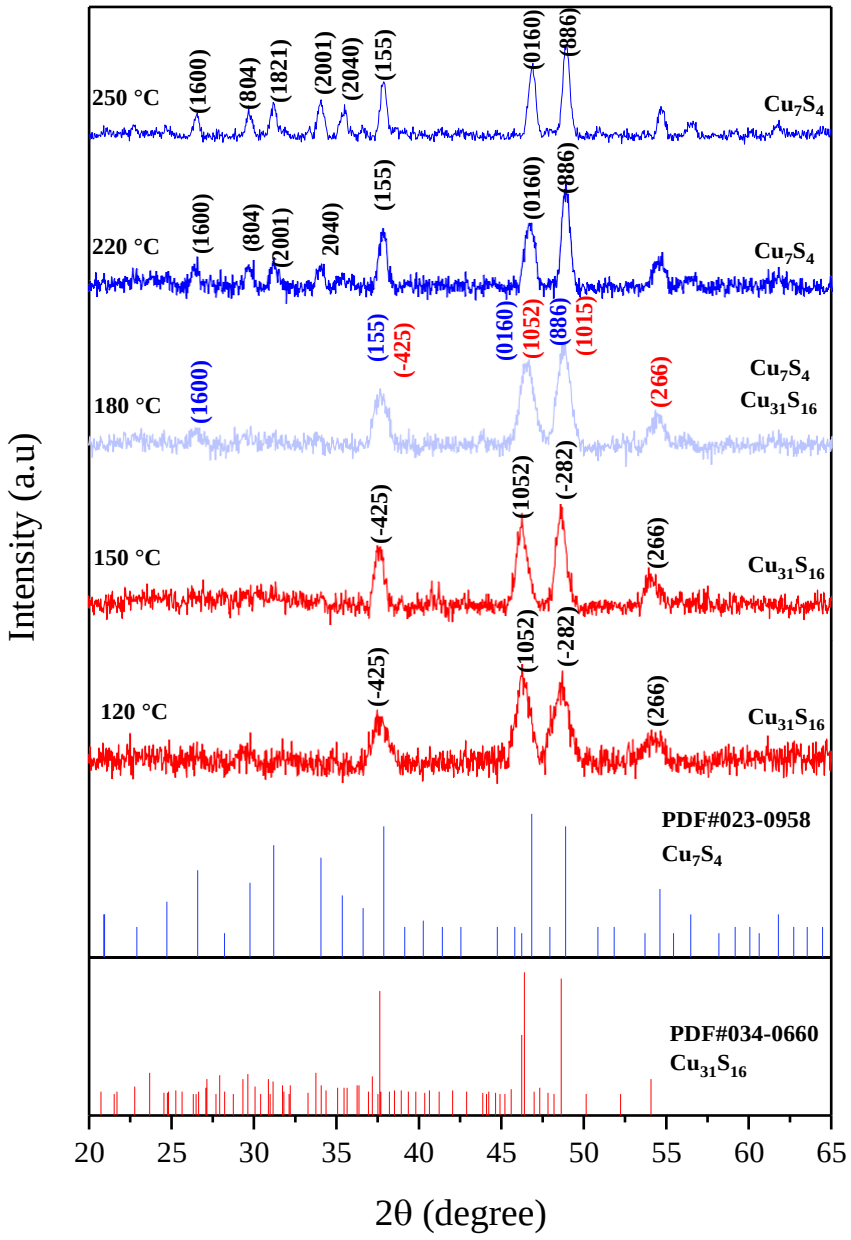

Figure 4. 1: Overlapped XRD patterns for the various phases of copper sulfide obtained at different synthesis temperatures

As the reaction temperature was increased to 180 ºC, the diffraction peaks of base-centered monoclinic Cu_7S_4 could be observed at 2θ = 26.53, 37.53, 46.50, and 48.72º, showing that the roxybite, syn phase of copper sulfide was beginning to form and may be generated at higher temperature. The formation of pure phase Cu_7S_4 was confirmed at 220 ºC, with the diffraction peaks at 2θ = 26.44, 29.62, 37.82, 46.70, and 48.82º, attributed to the (16 0 0), (8 0 4), (1 5 5), (0 16 0), and (8 8 6) of roxybite, syn (JCPDS No. 00-023-0958). XRD results for the two

samples at 220 and 250 ºC matched very well with the reported data of roxbyite [37, 38]. Obviously, the higher reaction temperature favored the phase transformation to the roxbyite phase, which perhaps was governed by the thermodynamic process. Furthermore, the formation of the Cu_7S_4 phase at higher temperature than the $Cu_{1.95}S$ phase was a confirmation of the difference in their stability temperature. Apart from the variation of the temperature, solvent system has also been used to alter the stoichiometry of the product in a solvothermal process involving the use of single-source precursors. For instance, Shen et al. [39] reported the formation of hexagonal phase Cu_2S nanocrystals by the thermal decomposition of copper diethyldithiocarbamate at 220 ºC when DDT was used as a surfactant. However, a change in the solvent system to oleic acid (OA) yielded pure monoclinic phase Cu_7S_4 (JCPDS: 23-0958)

4.2.2. Morphology studies by electron microscopy

The effects of reaction temperature on the size, morphology transformation, and also growth of the nanoparticles were studied by scanning and transmission electron microscopy. Figures 4.2(a and (b) show the SEM images of the pure djurlerite and roxbyite phases, respectively. The reaction temperature is a key factor in the controlled synthesis of colloidal inorganic nanoparticles [39-41]. The image showed that the samples were spherical even as the temperature was extended to 150 ºC. The formation of spherical nanoparticles in all the samples, as shown by the TEM images, could be ascribed to the ability of DDT as a surfactant to non-selectively adsorb on the surface of the crystal facets upon nucleation, thereby passivated all the surfaces of the crystal facets indiscriminately. This process successfully prohibited the facets from excessive growth and resulted in the isotropic growth of the nanoparticles.

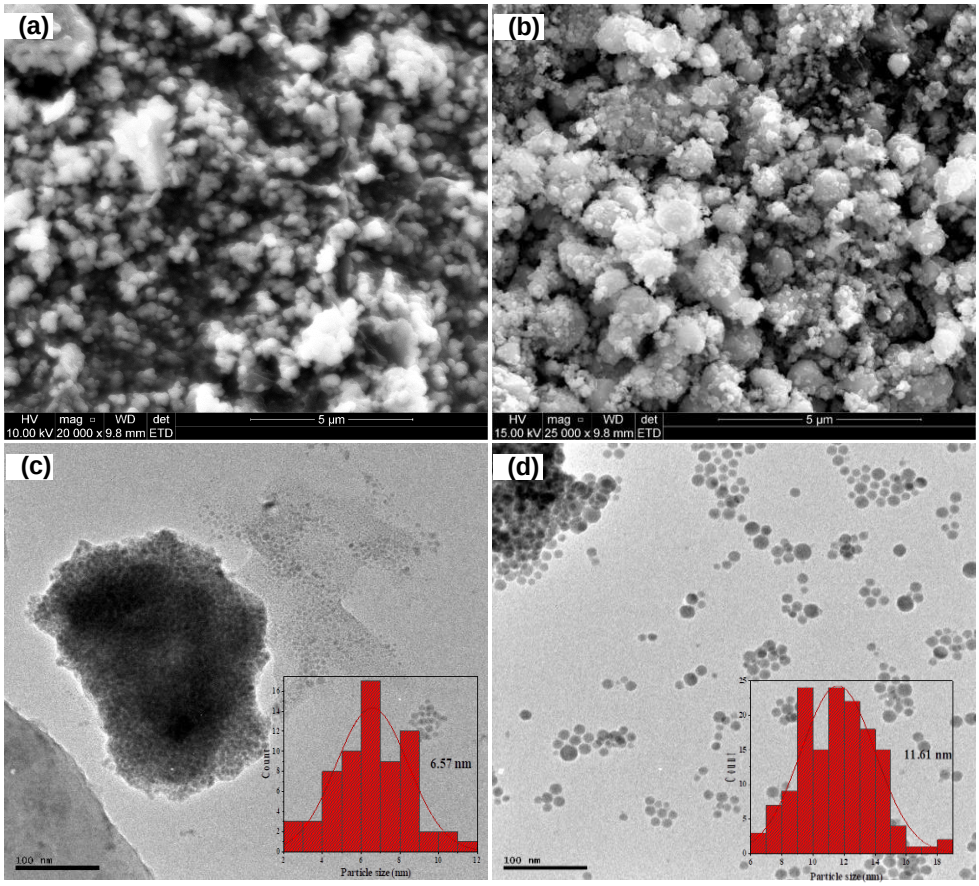

Figure 4. 2: SEM images of (a) $Cu_{31}S_{16}$ (120 °C) and (b) $Cu_{31}S_{16}$ (150 °C); TEM images of (c) $Cu_{31}S_{16}$ (120 °C) and (d) $Cu_{31}S_{16}$ (150 °C). Insets are the respective particle size distribution histogram.

In addition, the DDT played other roles during the thermal decomposition process of the copper complex precursor. It also acted as a sulfur donor, promoting the formation of sulfur-rich nanoparticles and also responsible for triggering the decomposition process of the single-source precursors at relatively low temperatures. This was important as it facilitates the separation of the nucleation process from the growth process, which is a critical factor for the development of high-quality nanoparticles. For example, the thermal decomposition temperature of the CuDTC was lowered from 260 °C in solid-state to 120 ºC in the presence of DDT in the solution state, similar to a previous report using oleylamine as a surfactant [42]. The micrographs showed no change in the morphology of the samples at both 120 and 150 ºC, but as presented in the particle size distribution histogram, an increase in the average nanoparticles size from 6.57 nm to 11.67 nm occurred as the reaction temperature was increased from 120 to 150 ºC.

Apart from the advantage of the single-source precursor method to be able to control the size and morphology of the nanoparticles through the choice of surfactants used in the reaction system, it also has the potential to control the chemical composition of the product in cases such as copper sulfide, with various stoichiometric compositions. As shown in Figures 4.3. (a)-(b), the roxbyite obtained at 220 and 250 ºC were quasi-spherical nanoparticles even as the reaction temperature was increased, and the TEM images presented in Figures 4.3. (c) and (d) indicated, at closer observation, that the morphology seemed to be tending towards hexagons. The alteration of morphology from distinct spherical structure to quasi-spherical structure, with temperature increase, showed that phase variation was associated with shape changes. The particles' size distribution histogram showed a size increase from 24.2 nm at 220 ºC to 26.4 nm at 250 ºC. Again indicating that a size growth occurred with temperature increase.

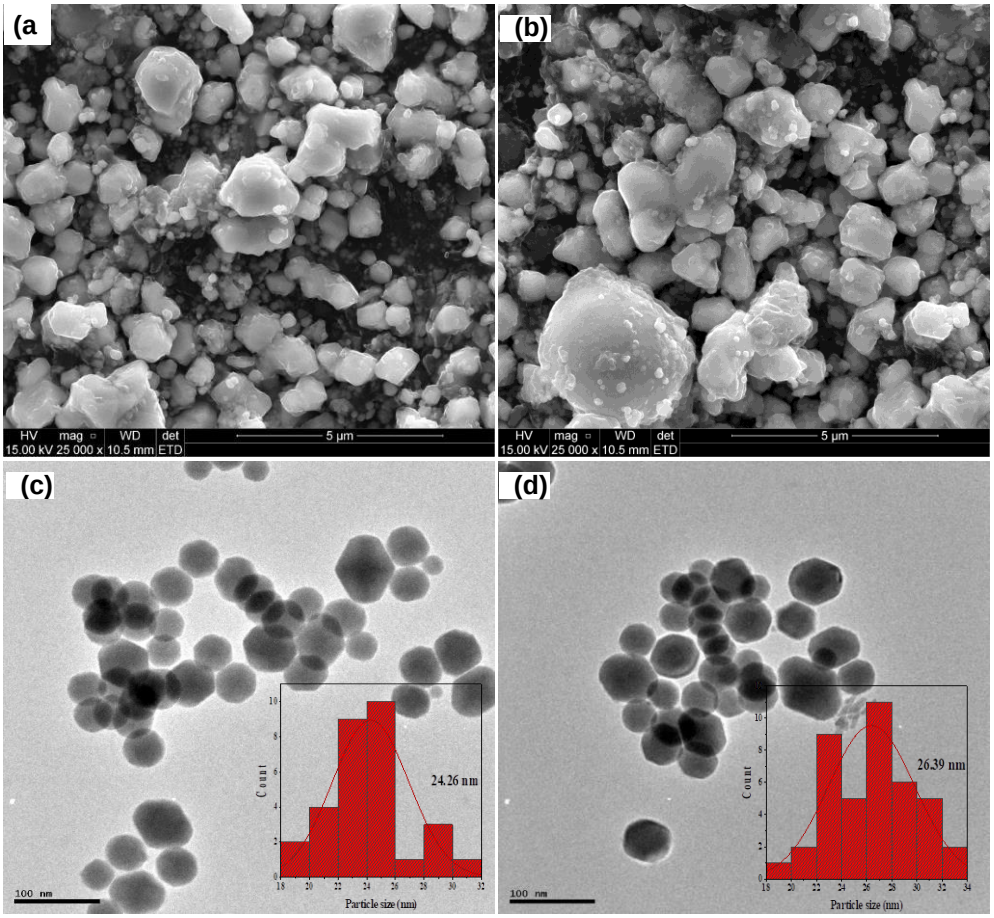

Figure 4. 3: SEM images of (a) Cu_7S_4 (220 °C), and (d) Cu_7S_4 (250 °C); TEM images of (c) Cu_7S_4 (220 °C), and (d) Cu_7S_4 (250 °C). Insets are the respective particle size distribution histogram.

4.2.3. Brunauer, Emmett, and Teller (BET) surface area analysis

The specific surface area of $Cu_{31}S_{16}$ (120 °C), $Cu_{31}S_{16}$ (150 °C), Cu_7S_4 (220 °C), Cu_7S_4 (250 °C) was investigated by the Brunauer−Emmett−Teller (BET) method, and the result obtained is summarized in Table 1. According to the adsorption isotherm classification of BET, the material was found to be a mesoporous structure. This is due to the presence of more surface active sites for the adsorption of TC molecules on all the synthesized copper sulfide nanoparticles investigated. The result revealed that the specific surface area of copper sulfide nanoparticles of $Cu_{31}S_{16}$ (120 °C), $Cu_{31}S_{16}$ (150 °C), Cu_7S_4 (220 °C), and Cu_7S_4 (250 °C) was found to be 14.98, 15.45, 16.95 and 17.32 m^2/g, while their pore sizes fall between 17.62 to 18.52 nm. Although the spherical shapes of these photocatalysts affect their BET measurement, the structure and specific surface area were favorable for adsorbing TC [43]

Table 4. 1: BET analysis of copper sulfide photocatalyst samples

Sample name	**Surface area** ***(m^2/g)***	**Pore diameter** ***(nm)***	**Pore volume** ***(m^3/g)***
$Cu_{31}S_{16}$ (120 °C)	14.98	17.62	0.074
$Cu_{31}S_{16}$ (150 °C)	15.45	17.45	0.077
Cu_7S_4 (220 °C)	16.95	18.23	0.085
Cu_7S_4 (250 °C)	17.32	18.52	0.087

4.2.4. Absorbance studies

The absorption spectra of the synthesized djurleite and roxbyite phases at different temperatures are shown in Figure 4. It shows some similarities in the spectra of the djurleite (120 and 150 °C) (Figure 4.4 (a) and (b)). Likewise, similar absorption spectra could be seen in the pattern of the roxbyite phase (220 and 250 °C) in Figure 4.4. (c) and (d). The djurleite phases show a broad peak from 300 to around 600 nm, while the roxbyite showed a narrow peak around 260 nm, which reaches a maximum of around 450 nm and declines to a minimum at ∼650 nm. In all the phases, the absorbance never reaches zero intensity, even at their minimum, but rises again towards the longer wavelengths region, and this is thought to arise due to the free-carrier intraband absorbance [44]. The absorbance of the roxbyite phases in this

longer wavelength region is stronger than the djurleite phases and may be due to free-carrier absorbance [45]. Considering that this NIR absorbance derives from free carriers, it should exhibit a stoichiometric dependence, and the observed behavior could be rationalized on this basis. In the spectrum of the djurleite at 120 ºC, there is an absorption shoulder around 900 nm. This corresponds to the bandgap energy of 1.36 eV and could be attributed to the band edge absorption of the nanoparticles.

The bandgap energies were determined by using Tauc relation:

$$\alpha h\upsilon = \beta(h\upsilon - Eg)^n$$

Where h is photon energy, α is the absorption coefficient, i.e., $\alpha = \frac{2.303A}{t}$ and β is the band edge. The n value can be 2 or 0.5 for direct or indirect transition, respectively [46].The values for the optical band gaps where found to be 1.34, 1.38, 2.14 and 2.20 eV for the $Cu_{31}S_{16}$ (120 ºC), (b) $Cu_{31}S_{16}$ (150 ºC), (c) Cu_7S_4 (220 ºC), and (d) Cu_7S_4 (250 ºC) respectively (inserts). These values are comparable to other similar studies [47, 48] and also indicated a shift to a shorter wavelength compared to the bandgap energy of their bulks [49, 44].

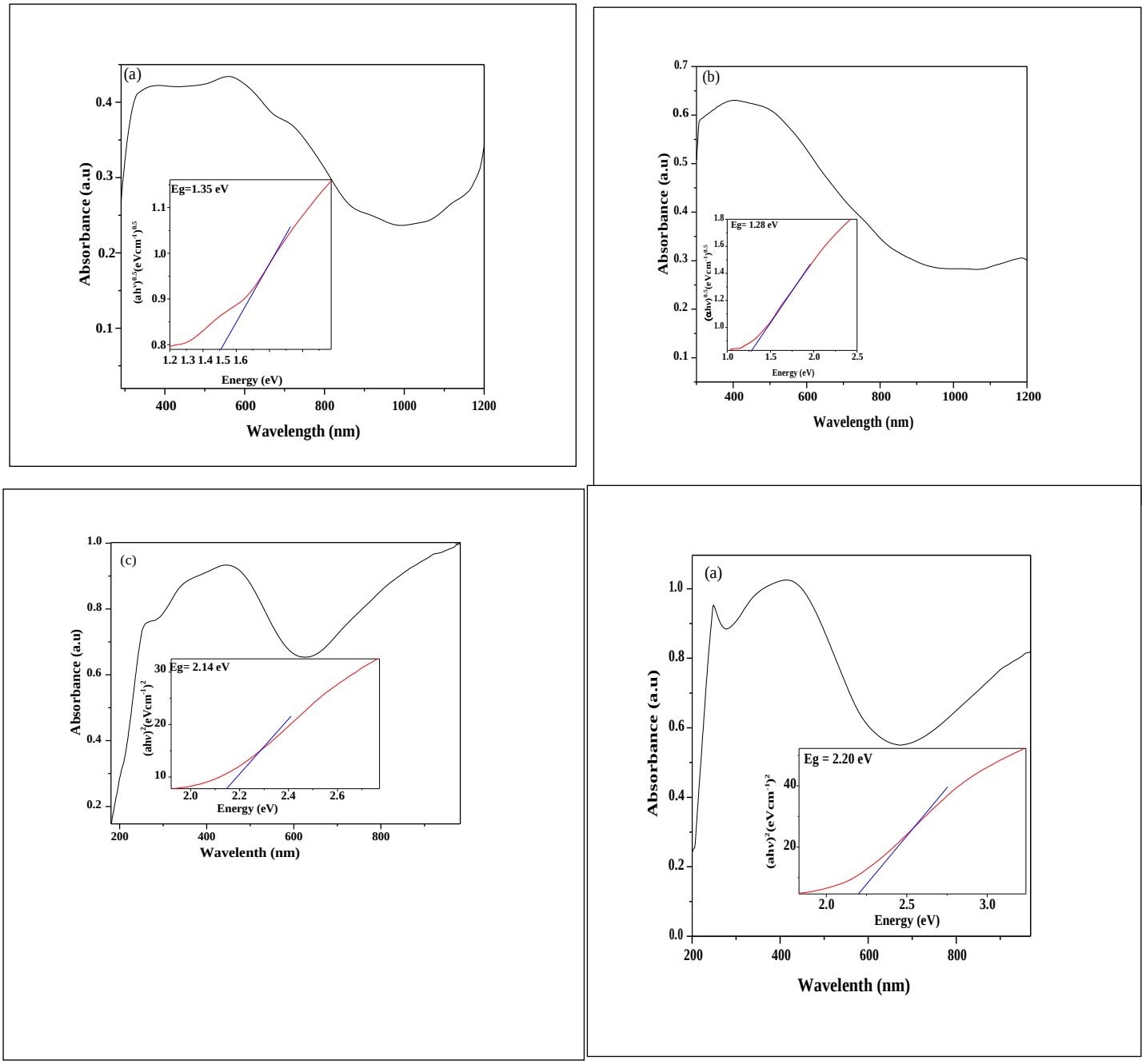

Figure 4. 4: UV-vis-NIR spectra of (a) $Cu_{31}S_{16}$ (120 °C), (b) $Cu_{31}S_{16}$ (150 °C), (c) Cu_7S_4 (220 °C), and (d) Cu_7S_4 (250 °C). Inset are the respective Tauc plots

4.3.0 Photocatalytic degradation of TC using roxybite and djulerite

The photocatalytic degradation of TC solution using the pure phase samples ($Cu_{31}S_{16}$ (120 ºC), $Cu_{31}S_{16}$ (150 ºC), Cu_7S_4 (220 ºC), and Cu_7S_4 (250 ºC)), was conducted under the visible light irradiation. In the absorption spectrum of an aqueous solution of TC, two absorption bands at approx. 275 and 360 nm are ascribed to the conjugated double-bond structures with two carbonyl groups and enolic groups, respectively [50]. The absorption spectra of tetracycline

using $Cu_{31}S_{16}$ (120 ºC), $Cu_{31}S_{16}$ (150 ºC), Cu_7S_4 (220 ºC), and Cu_7S_4 (250 ºC) as catalysts are shown in Figure 4.5. (a)-(d) respectively. The figure showed that the two phases of the copper sulfide nanoparticles, roxybite- Cu_7S_4 and djulerite-$Cu_{31}S_{16}$, irrespective of their difference in synthesis temperature, have similar degradation patterns. During the photocatalysis processes, a non-sequential decrease and a slight shift of the absorption peak at greater wavelengths were observed with an increase in irradiation time up to 120 min. The two roxybite phases exhibited greater catalytic ability than the djulerite phases, with 90% and 99% degradation for the Cu_7S_4 (220 ºC) and Cu_7S_4 (250 ºC) respectively, which could be ascribed to higher crystallinity of the roxybite phase at 250 ºC. The djulerite phases at 120 and 150 ºC showed lower degradation percentages of 70 and 85%, respectively. Therefore, there seemed to be a direct relationship between temperature and degradation efficiencies, and the degradation performance of these photocatalysts towards tetracycline molecules could be placed in the order $Cu_{31}S_{16}$ (120 ºC) < $Cu_{31}S_{16}$ (150 ºC) < Cu_7S_4 (220 ºC) < Cu_7S_4 (250 ºC). In addition to the crystallinity, the higher absorption properties observed in the absorption spectra of the roxybite phases could be responsible for higher photocatalytic activities [51] and a faster mineralization rate compared to the djulerite phases [50]. Due to the high degradation efficiency of the Cu_7S_4 (250 ºC), subsequent degradation experiments for further studies were limited to this phase.

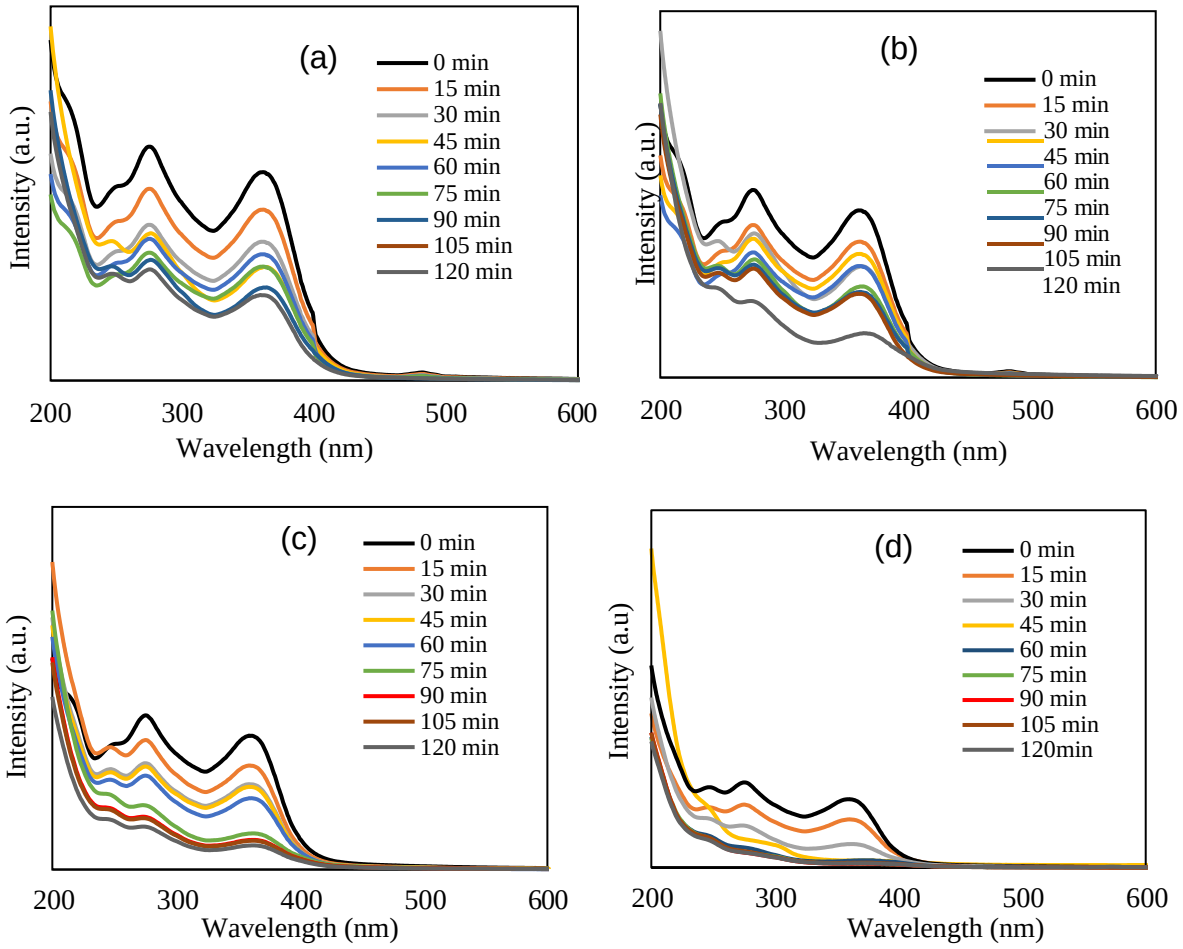

Figure 4. 5: Photocatalytic degradation of tetracycline under visible light irradiation using (a) $Cu_{31}S_{16}$ (120 °CºC), (b) $Cu_{31}S_{16}$ (150 °C), (c) Cu_7S_4 (220 °C), and (d) Cu_7S_4 (250 °C)

4.3.1. Effect of TC solution pH on the degradation efficiency

The initial pH of the solution is one of the important parameters that influence photocatalytic process of compounds through the surface electrical charge characteristics of photocatalysts, and it dictates the ionization state of the catalyst surface. The effect of the solution's pH was studied using 50 mg/L concentrations of TC, 80 mg of Cu_7S_4 (250 ºC), and solution pH in the range of 2–10. Figure 4.6. presents the removal efficiencies at different irradiation time up to 120 min. The degradation efficiency obtained at pH 4 was 99%, while pH 2, 6, 8, and 10 were 73.4, 62.3, 54.1, and 46.7 %, respectively. In addition, the outcome showed a decrease in percentage degradation of TC from 99 to 46.7% with an increase in the pH of the solution, an indication that pH 4 was the optimum [52]. Alkaline pH values (8 and 10) adversely affected

the photocatalytic degradation of TC, resulting in a decrease in the removal efficiency up to 46.7%. The decrease in removal efficiency of TC in the alkaline pH range could be attributed to the concentration of hydroxyl radical, which was influenced by the solution pH. Perhaps the pH of TC solution might have a significant effect on the surface ionic speciation of the Cu_7S_4 and was able to control the reactants type and products obtained in the process. Similar results were reported by Ahmadi et al., [53] and Hao et al., [54] on the photocatalytic degradation of TC using different photocatalysts. However, the influence of solution pH 2 on the degradation process was not very clear because no direct trend could be established on the basis of the acidity and alkalinity of the solution[55].

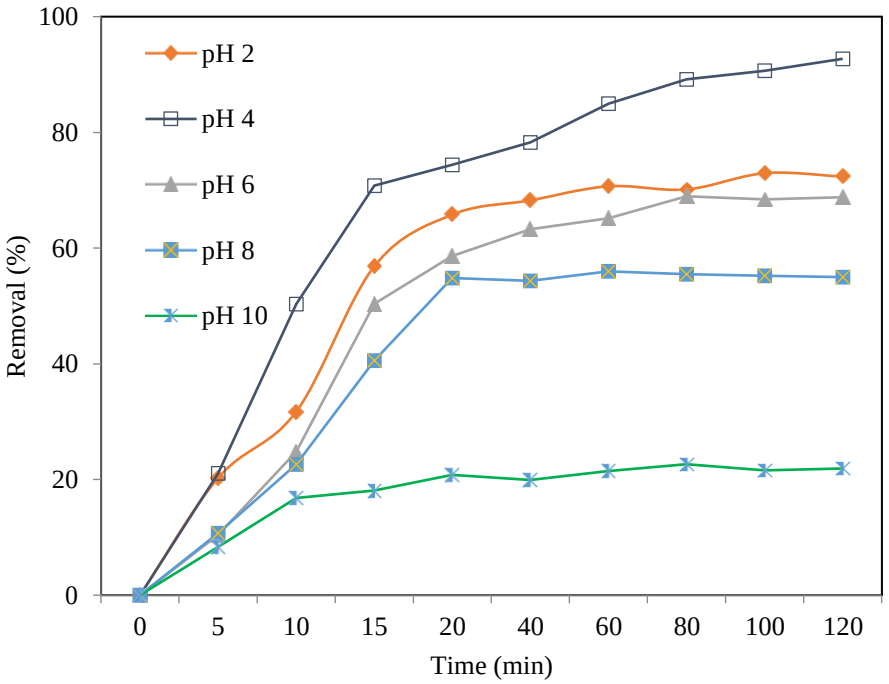

Figure 4. 6: Effect of TC solution pH on Cu_7S_4 (250°C), (dosage: 80 mg/L, irradiation time: 120 min, TC: 50 mg/L).

4.3.2 Effect of catalysts (Cu_7S_4 (250 ºC)) loading

The degradation of TC was conducted under the visible light irradiation in the absence of the photocatalyst, and very little (3 %) degradation of TC could be observed after 120 min reaction as presented in Figure 4.7. The removal of TC using different catalyst loading at pH 4 and TC concentration of 50 mg/L under the visible light was conducted afterward. An increase in the

degradation rate constants with an increase in catalyst loading from 5 to 80 mg occurred, with about 99.1 and 25 % degradation efficiencies achieved with 80 mg and 5 mg of Cu_7S_4 (250 ºC), respectively. The increase in degradation of TC with increasing concentration of Cu_7S_4 (250 ºC) in the solution could be ascribed to the increasing availability of more active sites, higher formation of OH, and increased effective interaction of the catalyst with the TC molecules. However, at a higher catalyst loading above 80 mg, most of the catalysts may suffer deactivation due to their accumulation, agglomeration, or precipitation, which could lead to decrease in the available catalyst surface for light absorption and consequently result in a decrease in the degradation rate. Although catalyst loading above 80 mg was not investigated, Figure 4.7 shows almost 100 % degradation of TC using 80 mg, indicating an optimal or equilibrium dosage for TC in this operating condition. These results were in accordance with some earlier reported studies involving the degradation performances of copper sulfide [56, 57].

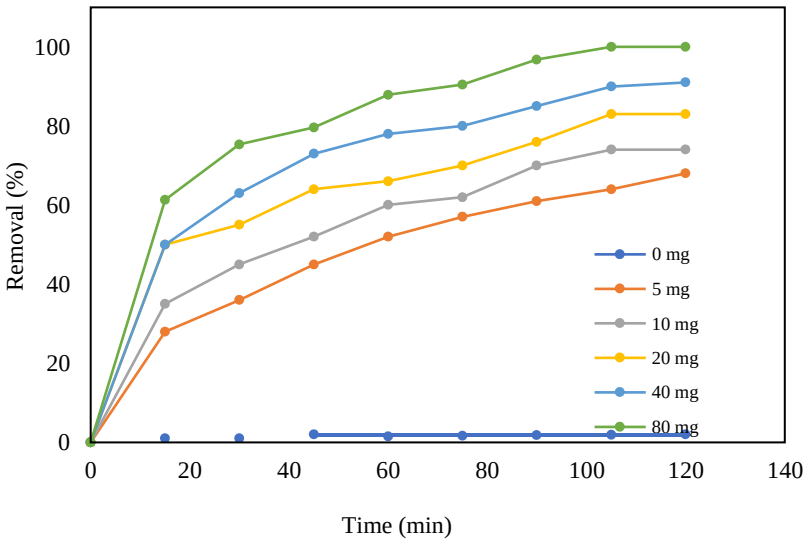

Figure 4. 7: The effect of catalyst loading on the photoreduction of TC using Cu_7S_4 (250°C) as photocatalyst.

4.3.3. Effect of initial concentration of TC

The effect of initial TC concentration on the removal efficiency of Cu_7S_4 (250 ºC) was investigated and presented in Figure 4.8(a). The rate of degradation could be determined by the formation of hydroxyl radicals at any TC concentration. It could be observed that the removal efficiency of the photocatalyst decreased with an increase in the initial TC concentrations from

5, to 25 mg/L after 120 min, which reflected lower removal efficiency at higher TC concentrations. This, thus, implies that the rate of the TC degradation will decrease with an increase in the initial TC concentration, which could be due to the fact that the concentration of generated •OH on the surface of the photocatalyst will decrease as more TC ions cover the active sites of the photocatalyst. Furthermore, there will be an increase in the concentration of TC molecules adsorbed on the surface of the photocatalyst as the initial TC concentration increases. The high concentration of adsorbed TC resulted in an inhibitive effect on the reaction of TC molecules with photogenerated holes or hydroxyl radicals due to the lack of any direct contact between them [58]. The increase in internal optical density that makes the solution become impervious to visible light is another reason for obtaining lower degradation efficiency at higher TC concentration. In addition, increasing TC concentration, which led to the absorption of light by the TC molecules, could also hinder the photons from reaching the photocatalyst surface, thereby decreasing the photocatalytic removal efficiency [59]. The equal amount of reactive radicals formed in all concentrations might lead to an increased reaction of TC molecules with radicals at lower TC concentrations. This could also result in a decrease in degradation [60]. The reusability of Cu_7S_4 (250 °C) was evaluated to determine its long-term user as a photocatalyst in the removal of TC. This experiment was conducted by repeating the degradation studies of TC using a solution of 25 mg/L. Figure 4.9. displays the recyclability of Cu_7S_4 (250 °C) for four cycles, and it can be clearly seen that the photocatalyst could be reused effectively after four cycles with little loss in activity. Thus, industrial application of this product is highly viable due to its reusability and stability properties. Similar results were reported in the studies related to the photodegradation of antibiotics [61, 62].

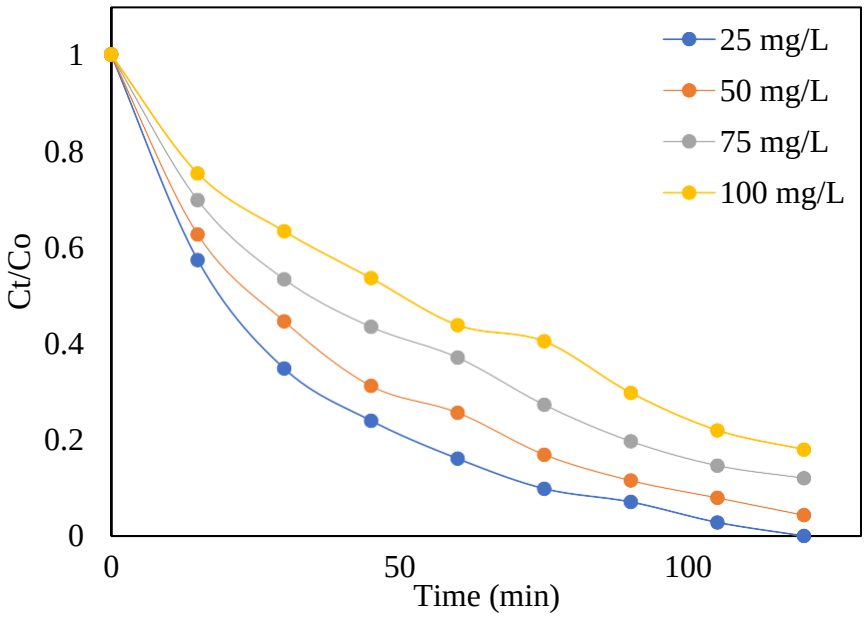

Figure 4. 8: Effect of TC concentration on to Cu_7S_4 (250 °C) (dosage: 80 mg, irradiation time: 120 min, pH: 4)

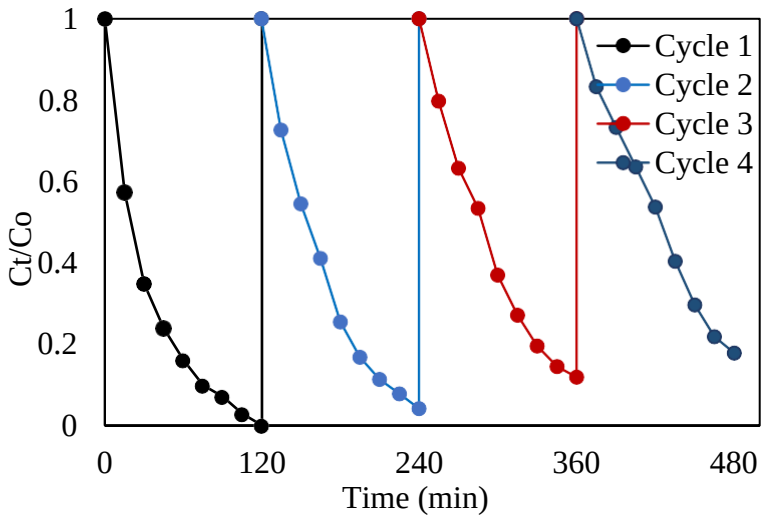

Figure 4. 9: Reusability cycles of TC degradation using Cu_7S_4 (250 °C) nanocomposite and a solution of 25 mg/L TC.

4.3.4. Photocatalytic degradation mechanism

Based on the obtained results and other related studies[16, 63], the possible mechanism involved in the photocatalytic degradation of TC under visible light has been proposed and presented in Figure 4.10. Upon the irradiation of Cu_7S_4, the photocatalysts are excited, leading to the generation of photogenerated electron-hole pairs that have strong reducing and oxidizing

powers, respectively. The photo-induced electron-hole pair is transferred to the surface of the photocatalyst and could directly be involved in the photocatalytic reaction process or produce active radicals[64]. In general, hydroxyl radicals ($^{\cdot}OH$), superoxide radicals ($^{\cdot}O_2^-$), and holes (h^+) can be found in the photocatalytic degradation process. Since the redox potential of the LUMO of Cu_7S_4 was more negative than that of $O_2/^{\cdot}O_2^-$ ($E_0 = -0.33$ eV/NHE), the dissolved O_2 can interact with the photoelectrons on the LUMO. This leads to the generation of $^{\cdot}O_2^-$ radicals and the charge carrier separation. The photogenerated holes can react with H_2O to form hydroxyl radicals (•OH). Finally, ($•O_2^-$) and (•OH) degrade TC into other products as shown in Figure 4.10.

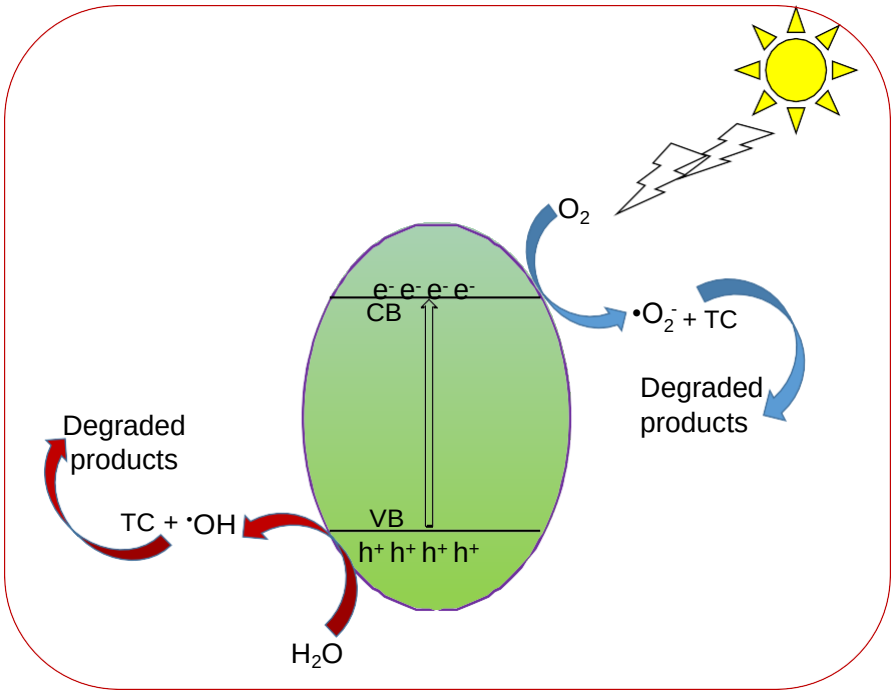

Figure 4. 10: The schematic representation of the possible photocatalytic mechanism involved in the degradation of TC under visible light irradiation

4.4.0. Conclusions

In summary, a simple one-pot solvothermal route was used to prepare pure phase copper sulfide nanoparticles by variation in the reaction temperature, resulting in phase transformation from djurleite ($Cu_{31}S_{16}$) to roxbyite phase as temperature increased from 120 to 250 ºC. No morphological changes accompanied the phase transformation process even after increasing the reaction temperature to 250 ºC. An observable increase in particle size occurred, which

was induced by temperature increase, and the optical characterization showed bandgap energy in the range 1.34 - 2.20 eV. Photocatalytic degradation of TC using the synthesized pure phases djurlite and roxbyite phases showed photocatalytic activities, with Cu_7S_4 (250 ºC) exhibiting the greatest efficiency of 99% at pH 4 compared to the performances achieved using the other samples (Cu_7S_4 (220 ºC), djurleite $Cu_{31}S_{16}$ (150 ºC), and $Cu_{31}S_{16}$ (120 ºC). The photocatalytic experimental data conform to a pseudo-second order kinetics model with higher correlation factor. This is an indication that the interaction between TC and copper sulfide-nanoparticles is based on chemical reaction. Overall, roxybite (Cu_7S_4) could be considered as a potential catalyst for the degradation of TC in solution.

4.5.0. References

1. Cully, M., *Public health: the politics of antibiotics.* Nature, 2014. **509**(7498): p. S16-S17.
2. Cheng, D., *et al.*, *A critical review on antibiotics and hormones in swine wastewater: Water pollution problems and control approaches.* Journal of hazardous materials, 2020. **387**: p. 121682.
3. Pan, Y., *et al*., *Enhanced removal of antibiotics from secondary wastewater effluents by novel UV/pre-magnetized Fe0/H_2O_2 process.* Water research, 2019. **153**: p. 144-159.
4. Wang, J. and R. Zhuan, *Degradation of antibiotics by advanced oxidation processes: An overview.* Science of The Total Environment, 2020. **701**: p. 135023.
5. Ahmadi, M., *et al*., *Enhanced photocatalytic degradation of tetracycline and real pharmaceutical wastewater using MWCNT/TiO2 nano-composite.* Journal of environmental management, 2017. **186**: p. 55-63.
6. De Cazes, M., *et al*., *Design and optimization of an enzymatic membrane reactor for tetracycline degradation.* Catalysis Today, 2014. **236**: p. 146-152.
7. Tong, X., *et al*., *Insights into the interactions between tetracycline, its degradation products and bovine serum albumin.* SpringerPlus, 2016. **5**(1): p. 1-9.
8. Ji, Y., *et al*., *Thermo-activated persulfate oxidation system for tetracycline antibiotics degradation in aqueous solution.* Chemical Engineering Journal, 2016. **298**: p. 225-233.
9. Gu, C. and K. Karthikeyan, *Interaction of tetracycline with aluminum and iron hydrous oxides.* Environmental science & technology, 2005. **39**(8): p. 2660-2667.
10. Xiong, H., *et al*., *Enhancing degradation and mineralization of tetracycline using intimately coupled photocatalysis and biodegradation (ICPB).* Chemical Engineering Journal, 2017. **316**: p. 7-14.
11. Zhu, X., *et al*., *A novel porous carbon derived from hydrothermal carbon for efficient adsorption of tetracycline.* Carbon, 2014. **77**: p. 627-636.
12. Zhu, X.-D., *et al*., *Photocatalytic degradation of tetracycline in aqueous solution by nanosized TiO2.* Chemosphere, 2013. **92**(8): p. 925-932.
13. Liu, M., *et al*., *Zero valent iron particles impregnated zeolite X composites for adsorption of tetracycline in aquatic environment.* RSC advances, 2015. **5**(125): p. 103480-103487.

14. Chen, X., *et al.*, *Facile fabrication of hierarchical porous ZIF-8 for enhanced adsorption of antibiotics.* Journal of hazardous materials, 2019. **367**: p. 194-204.
15. Zhao, Y., *et al*., *Comparing polyvalent bacteriophage and bacteriophage cocktails for controlling antibiotic-resistant bacteria in soil-plant system.* Science of the Total Environment, 2019. **657**: p. 918-925.
16. Wu, S., *et al*., *Visible light photocatalytic degradation of tetracycline over TiO2.* 2020. **382**: p. 122842.
17. Wang, X., *et al.*, *Three-dimensional g-C_3N_4 aggregates of hollow bubbles with high photocatalytic degradation of tetracycline.* 2018. **136**: p. 103-112.
18. Ahadi, M., *et al*., *Novel preparation of sensitized ZnS nanoparticles and its use in photocatalytic degradation of tetracycline.* 2016. **13**(12): p. 2797-2804.
19. Yan, M., *et al*., *Microwave-assisted synthesis of monoclinic–tetragonal BiVO 4 heterojunctions with enhanced visible-light-driven photocatalytic degradation of tetracycline.* 2015. **5**(110): p. 90255-90264.
20. Ahmadi, M., *et al*., *Enhanced photocatalytic degradation of tetracycline and real pharmaceutical wastewater using MWCNT/TiO_2 nano-composite.* 2017. **186**: p. 55-63.
21. Xiong, H., *et al*., *Enhancing degradation and mineralization of tetracycline using intimately coupled photocatalysis and biodegradation (ICPB).* 2017. **316**: p. 7-14.
22. Niu, J., et al., *Visible-light-mediated Sr-Bi2O3 photocatalysis of tetracycline: kinetics, mechanisms and toxicity assessment.* 2013. **93**(1): p. 1-8.
23. Duong, T.-N.-B. and M.-V. Le. *High efficiency degradation of tetracycline antibiotic with TiO_2-SiO_2 photocatalyst under low power of simulated solar light irradiation*. in *AIP Conference Proceedings*. 2019. AIP Publishing LLC.
24. Semeraro, P., *et al*., *Photocatalytic degradation of tetracycline by ZnO/γ-Fe_2O_3 paramagnetic nanocomposite material.* 2020. **10**(8): p. 1458.
25. Cao, M., *et al*., *Visible light activated photocatalytic degradation of tetracycline by a magnetically separable composite photocatalyst: graphene oxide/magnetite/cerium-doped titania.* 2016. **467**: p. 129-139.
26. Lai, C., *et al.*, *Facile synthesis of CeO2/carbonate doped $Bi_2O_2CO_3$ Z-scheme heterojunction for improved visible-light photocatalytic performance: Photodegradation of tetracycline and photocatalytic mechanism.* 2021. **588**: p. 283-294.

27. Liu, Y., *et al*., *Enhanced photocatalytic activity over flower-like sphere $Ag/Ag_2CO_3/BiVO_4$ plasmonic heterojunction photocatalyst for tetracycline degradation.* 2018. **331**: p. 242-254.
28. Lv, C., *et al*., *Rapidly and highly efficient degradation of tetracycline hydrochloride in wastewater by 3D IO-TiO_2-CdS nanocomposite under visible light.* 2021. **42**(3): p. 377-387.
29. Page, M., *et al*., *Copper sulfide as a light absorber in wet-chemical synthesized extremely thin absorber (ETA) solar cells.* 2009. **2**(2): p. 220-223.
30. Isac, L., *et al*., *Copper sulfides obtained by spray pyrolysis—possible absorbers in solid-state solar cells.* Thin Solid Films, 2007. **515**(15): p. 5755-5758.
31. Khan, M.D., *et al*., *Tuning the phase and shape of copper sulfide nanostructures using mixed solvent systems.* ChemistrySelect, 2016. **1**(18): p. 5982-5989.
32. Ueda, H., *et al*., *Copper pyrites CuS 2 and CuSe 2 as anion conductors.* Physical Review B, 2002. **65**(15): p. 155104.
33. Mulder, B.J., *Optical properties of crystals of cuprous sulphides (chalcosite, djurleite, Cu1.9S, and digenite).* physica status solidi (a), 1972. **13**(1): p. 79-88.
34. Akhtar, M., et al., *Phase controlled synthesis of copper sulfide nanoparticles by colloidal and non-colloidal methods.* Materials Chemistry and Physics, 2016. **180**: p. 404-412.
35. Schneider, N., D. Lincot, and F. Donsanti, *Atomic layer deposition of copper sulfide thin films.* Thin Solid Films, 2016. **600**: p. 103-108.
36. Ravele, M.P., O.A. Oyewo, and D.C. Onwudiwe, *Controlled Synthesis of CuS and Cu_9S_5 and Their Application in the Photocatalytic Mineralization of Tetracycline.* 2021. **11**(8): p. 899.
37. Qin, Y., *et a*l., *High-performance aqueous polysulfide-iodide flow battery realized by an efficient bifunctional catalyst based on copper sulfide.* Materials Today Energy, 2021. **21**: p. 100746.
38. Jiao, S., et al., *Well-defined non-spherical copper sulfide mesocages with single-crystalline shells by shape-controlled Cu_2O crystal templating.* Advanced Materials, 2006. **18**(9): p. 1174-1177.
39. Shen, S., *et al*., *Generalized synthesis of metal sulfide nanocrystals from single-source precursors: size, shape and chemical composition control and their properties.* CrystEngComm, 2011. **13**(14): p. 4572-4579.

40. Zhuang, Z., Q. Peng, and Y. Li, *Controlled synthesis of semiconductor nanostructures in the liquid phase.* Chemical Society Reviews, 2011. **40**(11): p. 5492-5513.
41. Wang, Y., *et al*., *Shape-controlled synthesis of PbS nanocrystals via a simple one-step process.* Langmuir, 2012. **28**(47): p. 16436-16443.
42. O.C Olalekan and D.C. Onwudiwe, *Temperature controlled evolution of pure phase Cu_9S_5 nanoparticles by solvothermal process.* Frontiers in Materials, 2021.
43. Zhang, S., *et al*., *Preparation of Nano-Copper Sulfide and Its Adsorption Properties for 17α-Ethynyl Estradiol.* Nanoscale Research Letters, 2020. **15**(1): p. 48.
44. Zhao, Y., *et al*., *Plasmonic $Cu2-x$ S nanocrystals: optical and structural properties of copper-deficient copper (I) sulfides.* Journal of the American Chemical Society, 2009. **131**(12): p. 4253-4261.
45. Partain, L., *et al*., *Degradation of a Cu* x *S/CdS solar cell in hot, moist air and recovery in hydrogen and air.* Journal of applied physics, 1983. **54**(11): p. 6708-6720.
46. Aftab, M., *et al*., *Optical and electrical properties of NiO and Cu-doped NiO thin films synthesized by spray pyrolysis.* Optical Materials, 2021. **119**: p. 111369.
47. Mulder, B., *Optical properties and energy band scheme of cuprous sulphides with ordered and disordered copper ions.* physica status solidi (a), 1973. **18**(2): p. 633-638.
48. Behboudnia, M. and B. Khanbabaee, *Investigation of nanocrystalline copper sulfide Cu_7S_4 fabricated by ultrasonic radiation technique.* Journal of crystal growth, 2007. **304**(1): p. 158-162.
49. Abdelhady, A.L., *et al*., *New routes to copper sulfide nanostructures and thin films.* Journal of Materials Chemistry, 2011. **21**(44): p. 17888-17895.
50. Wu, S., *et al*., *Visible light photocatalytic degradation of tetracycline over TiO2.* Chemical Engineering Journal, 2020. **382**: p. 122842.
51. Wang, D., *et al*., *Simultaneously efficient adsorption and photocatalytic degradation of tetracycline by Fe-based MOFs.* 2018. **519**: p. 273-284.
52. Nasseh, N., B. Barikbin, and L. Taghavi, *Photocatalytic degradation of tetracycline hydrochloride by FeNi3/SiO2/CuS magnetic nanocomposite under simulated solar irradiation: Efficiency, stability, kinetic and pathway study*. Environmental Technology & Innovation, 2020. **20**: p. 101035.
53. Ahmadi, M., *et al*., *Enhanced photocatalytic degradation of tetracycline and real pharmaceutical wastewater using MWCNT/TiO2 nano-composite.* Journal of Environmental Management, 2017. **186**: p. 55-63.

54. Hao, R., *et al*., *Efficient adsorption and visible-light photocatalytic degradation of tetracycline hydrochloride using mesoporous BiOI microspheres.* 2012. **209**: p. 137-145.
55. Nasseh, N., *et al*., *Synthesis and characterizations of a novel $FeNi_3/SiO_2/CuS$ magnetic nanocomposite for photocatalytic degradation of tetracycline in simulated wastewater.* Journal of Cleaner Production, 2018. **179**: p. 42-54.
56. Kundu, J. and D. Pradhan, *Controlled synthesis and catalytic activity of copper sulfide nanostructured assemblies with different morphologies.* ACS applied materials & interfaces, 2014. **6**(3): p. 1823-1834.
57. Chen, Y., et al., *Recent advances in the utilization of copper sulfide compounds for electrochemical CO2 reduction.* Nano Materials Science, 2020. **2**(3): p. 235-247.
58. Ahmad, F., D. Zhu, and J. Sun, *Environmental fate of tetracycline antibiotics: degradation pathway mechanisms, challenges, and perspectives.* Environmental Sciences Europe, 2021. **33**(1): p. 64.
59. Dai, J., Y. Sun, and Z. Liu, *Efficient degradation of tetracycline in aqueous solution by Ag/AgBr catalyst under solar irradiation.* Materials Research Express, 2019. **6**(8): p. 085512.
60. Farzaneh, S., N. Keramati, and M.M. Ghazi, *Optimization of Photocatalytic Degradation of Tetracycline Using Titania Based on Natural Zeolite by Response Surface Approach.* Journal of Water Chemistry and Technology, 2020. **42**(1): p. 30-35.
61. Farzadkia, M., *et al., Investigation of photocatalytic degradation of clindamycin antibiotic by using nano-ZnO catalysts.* 2014. **31**(11).
62. Zuo, S., *et al., A facile and novel construction of attapulgite/Cu2O/Cu/g-C3N4 with enhanced photocatalytic activity for antibiotic degradation.* 2017. **43**(3): p. 3324-3329.
63. Hou, C., H. Liu, and Y.J.R.A. Li, *The preparation of three-dimensional flower-like $TiO_2/TiOF$ 2 photocatalyst and its efficient degradation of tetracycline hydrochloride.* 2021. **11**(25): p. 14957-14969.
64. Jin, Y., *et al., Construction of ultrafine TiO 2 nanoparticle and SnNb 2 O 6 nanosheet 0D/2D heterojunctions with abundant interfaces and significantly improved photocatalytic activity.* 2017. **7**(11): p. 2308-2317.

Chapter 5

Copper oxide nanoparticles and their applications in the photocatalytic degradation of acyclovir (ACV)

5.0. Introduction

Antivirals are an essential class of pharmaceuticals because of their therapeutic activity in humans. These drugs are also preventive and could protect the body from getting viral infections by fighting off harmful viruses. They ease the symptoms and shorten the length of viral infection [1]. Currently, there are 13 groups of 90 approved antiviral drugs classified into different categories based on their mechanism of action, structure, or regulation. The outbreak of HIV, influenza, coronavirus, etc., has led to their high consumption rate, resulting in their increased presence in the environment. Consequently, both the virus and the antiviral drugs could co-exist in the same waterbody, causing the organisms to develop resistance. This is the leading cause for virus developing resistance towards antiviral drugs.

Antivirals are amongst the most dangerous drugs towards aquatic species. Even in small concentrations, their presence is of enormous concern because the available conventional water treatment techniques can not completely get rid of them [2]. Acyclovir (ACV) is the focus of this study due to its wide use and production worldwide; it was detected in wastewater treatment plants (WWTPs), confirming its persistence, and rivers with concentrations up to 0.04–3.2 μgL^{-1} [3].

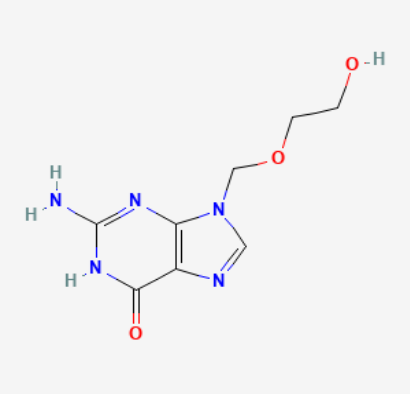

Figure 5. 1: Structure of acyclovir

In human medicine, ACV is used to treat cold sores, herpes simplex virus (HSV) types 1 and 2, varicella-zoster virus, Epstein-Barr virus, hepatitis B virus, and cytomegalovirus. It can also be used to treat genital herpes and chickenpox. In veterinary, it is used to treat parvovirus [4].

Although ACV is administered in high doses, it has low absorption due to its poor solubility in water. This results in its excretion from the body in its unchanged form as an active compound. Its continuous utilization has led to its detection in numerous water bodies [4, 5], wastewater treatment plants [5] [6], and drinking water [4]. Once in water bodies, it could react with inorganic or organic constituents present in water, leading to a persistent additional molecule. As a contaminant in water, small amounts of ACV consumption may cause diarrhea, headache, renal failure, and stomach upset [7]. Therefore, it is crucial to remove ACV from water.

Numerous technologies have been employed for ACV elimination, such as catalytic ozonation [8], photolysis [9], adsorption [6,10-11] , UV/H_2O_2 [12], biological treatment [13], and photocatalytic degradation [14,15]. In photocatalytic degradation processes involving UV light, high exposure to irradiation may occur, which is detrimental to the human system and, in addition to the high cost of the light source. To avoid the danger associated with the exposure and also address the cost issues of the UV light, it might be helpful to explore photocatalysts that utilize the visible light. The solar spectrum is mainly made of visible light; therefore, it could serve as a good source of radiation and energy required to initiate the formation of free radicals in the semiconductor materials. Currently, in the literature, studies involving the photodegradation of ACV using semiconductor metal oxides is not well reported; therefore, this study will explore the photodegradation of ACV by using visible light.

Metal oxides have emerged as promising semiconductors that can utilize visible light due to their wide bandgap energies. Examples includes, $BiVO_4$ [16], Fe_2O_3 [17] ,WO_3 [18] , Bi_2WO_6 [19, 20], BiOI [21]. CuO has been selected in this study as the metal oxide of choice due to its desirable properties, including low cost, high stability, environmental friendliness, and excellent light absorption with an indirect bandgap of 1.3-2.1 eV (based on the conditions and synthesis method) [22], making it a suitable semiconductor. It (CuO) is a p-type semiconductor, which arises from its self-doping that is occasioned by non-stoichiometry [22].

5.1.0. Materials and Methods

Copper(II) acetate monohydrate was purchased from Sigma Aldrich, South Africa. It was of analytical grade and used as received without further purification.

5.1.1 Instrumentation

The crystalline structures were studied using powder XRD on a Bruker D8 Avance X-Ray Diffractometer (Karlsruhe, Germany). Microstructural studies were carried out using a transmission electron microscope (Hitachi HF–2000 TEM at 200 kV by Hitachi High-Tech Corporation, Tokyo, Japan) operated at 200 kV and a JEOL 6400F field-emission SEM (Zeiss, Oberkochen Germany). The atomic-level compositions were examined by energy-dispersive spectroscopy (EDS) attached to the SEM. Functional groups of the complex were studied using Fourier transform infrared (FTIR) spectroscopy on a Bruker Alpha-P FTIR spectrometer (Bremen, Germany). The absorption spectra were measured using Lambda 365 double-beam UV-Visible spectrophotometer (PerkinElmer). Thermal analysis (TGA, a SDTQ 600 Thermal instrument) was conducted from room temperature to 650 °C under flowing nitrogen using simultaneous thermal analysis (STA) technique for parallel recording of TG (thermogravimetry) and DSC (differential scanning calorimetry) curves. A heating rate of 10 °C min−1 was used.

5.2.2. Synthesis of copper oxide nanoparticles

About 5.5 g of copper acetate was dissolved in 25 mL of deionized water. The solution was heated slowly to 90 °C with continuous stirring followed by the addition of 5 mL of ethylene glycol. The resultant solution was heated and maintained at 120 °C with constant stirring until it changed into brown solids. The loose powdered solids were further calcinated at 350, 400, and 450 °C for 4 h.

5.2.3. Photocatalytic evaluation

The photocatalytic activity of the CuO NPs was tested for degradation of acyclovir (ACV) (Aldrich 97%) in aqueous solutions under visible light irradiation. In the experiments, 20 mg amount of each photocatalyst was introduced into the 100 mL flask containing a 500 mL aqueous solution of 1mg/L ACV in the photocatalytic reactor. An LED visible light lamp was used as the light source. After stirring the solution in the dark for 60 min in order to attain an adsorption-desorption equilibrium between the ACV molecules and photocatalysts, the reactor was illuminated with LED light, and the process lasted for 120 min. During the experiment, about 5 mL aliquots of the solution were collected at 15 min intervals and

filtered using 0.45 μm nylon syringe filters (PerknElmer). A UV–vis spectrophotometer was used to measure the concentration variations of the residual ACV during the photodegradation process. The process was repeated for different concentrations as well as pH. The initial concentrations of ACV were adjusted by HCl and NaOH (0.1M). Degraded ACV concentration was calculated using the formula:

$$degradation\% = \frac{C0 - Ci}{Co} X100\% = \frac{A0 - Ai}{Ao} X100\%$$

where Ci is the concentration of ACV at a specific time, C0 denotes the initial concentration of ACV, Ai is the absorbance of ACV at different times, and A0 is the blank absorbance of the original solution.

5.3.0. Results and discussion

5.3.1. Thermogravimetric analysis of Cu(acetate)

Thermogravimetric analysis (TGA) of the copper acetate was carried out under N_2 atmosphere in order to determine the temperature at which the complex is completely converted into the desired metal oxide. Figure 5.1. (a) presents the TG analysis graph, from which it is apparent that the decomposition of the copper acetate commenced at about two step decomposition process was observed. The second decomposition step occurred at about 230 ºC. An approximate mass loss of about 10.10% occurred in the first decomposition step (91-162 °C), and evidence from the literature showed that the first stage is mainly the dehydration of the sample [23-25]. This step has maximum decomposition at 145 °C, according to the DTG (Figure 5.1.(b)), and corresponds to an endothermic peak in the DSC graph (Figure 5.1.(c)). The second decomposition was then the decomposition of anhydrous copper acetate, in the temperature range of 230-300°C, which caused a weight loss of 53.60%. The Maximum temperature of decomposition of this stage was around 250 C in the DTG and corresponded to an endothermic peak in the DSC graph (Figure 5.1. (c)). This second step has been found to be exothermic in the air [26]. The probable reactions that may be involved in this decomposition process could be described thus:

$$Cu(CH_3COO)_2{\cdot}H_2O \rightarrow Cu(CH_3COO)_2 \quad (1)$$

$$Cu(CH_3COO)_2 \rightarrow Cu_2O \quad (2)$$

Although copper could exist as Cu(I) and Cu(II), under nitrogen atmosphere, the more favored

state is Cu(I), and possible oxidation to a higher oxidation state of Cu could occur under atmospheric air. Thermogravimetric analysis of copper(II) acetate, carried out in the air, has shown a mass gain of about 2.50% around 300 to 400 °C, which was attributed to the oxidation of Cu_2O to CuO [27].

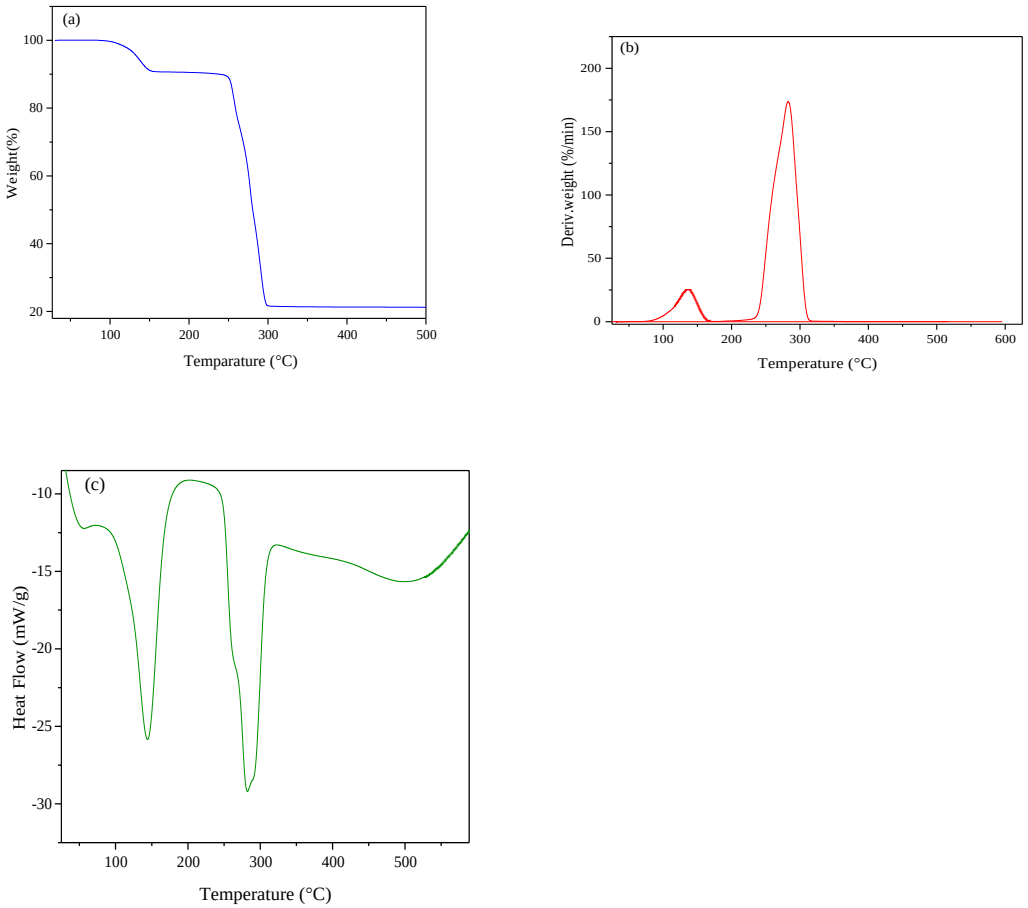

Figure 5. 2: (a) Thermogravimetric analysis (TGA), (b)derivative thermogravimetry (DTG), and (c)differential scanning calorimetry (DSC) of copper acetate.

5.3.2. Synthesis of CuO nanoparticles

CuO nanoparticles were prepared by the thermal decomposition of copper acetate mixed with ethylenelycol in a furnace at different temperatures between 350 – 450 °C for 4 h. At a lower reaction time (less than 4 h), mixed phases were obtained. The temperature of calcination was established by TG analysis of copper acetate under nitrogen atmosphere and based on the decomposition profile presented in the TGA graph, three synthesis temperatures were chosen. Figure 5.2. presents a schematic presentation of the synthesis steps :

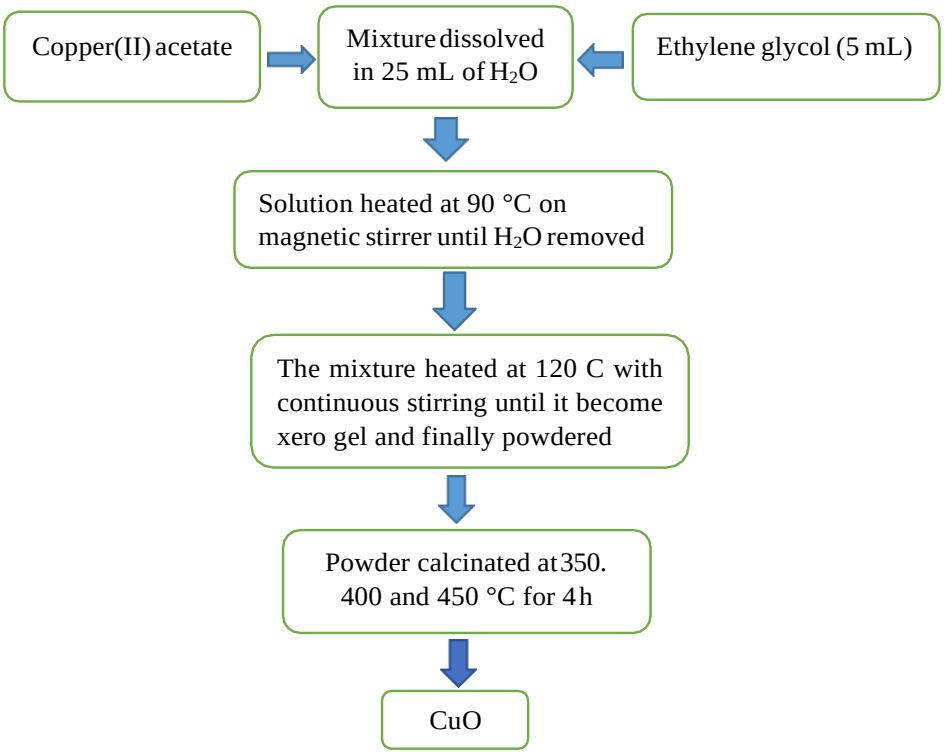

Figure 5. 3: Synthesis scheme for the CuO nanoparticles

5.3.3. XRD analysis of the copper oxide nanoparticles

The structural and the phase purity of the as-synthesized copper oxide nanoparticles at the two different temperatures were carried out using XRD and presented in Figure 5.3. The decomposition temperature of the precursor compound determines the composition and stoichiometry of the copper oxide. For the samples obtained at 350 and 400 ℃, the diffraction patterns identified at 2θ (32.5, 35.63, 38.78 and 48.65°) corresponded to (110), (11-1), (111) and (20-2) planes respectively of monoclinic tenorite (CuO) with space group C2/c and JPCD no. 0481548. The sharpness of the patterns indicated that the obtained NPs at these temperatures were highly crystalline. At these temperatures, there were no impurity peaks observed[28] [29]. The average crystalline sizes at these temperatures were calculated using the Scherrer equation:

$$D = \frac{k\lambda}{\beta cos\theta}$$

Where D=crystallite size (nm)

K=0.9 (Scherrer constant)

λ=0.15406nm (wavelength of the x-ray sources

β=FWHM (radians)

θ=peak position (radians)

and were found to be 32.16 and 32.75 nm for 350 and 400 ℃, respectively, and agreed with the previously reported study [30]. The XRD patterns of the sample obtained at low-temperature calcination (300 C) showed peaks identified at 2θ = 29.56, 36.33,42.21,61.45, and 73.58°, which corresponded to the cubic Cu_2O phase of copper oxide.

This indicated that calcination temperature above the decomposition temperature of the copper acetate is required to ensure the pure phase of CuO

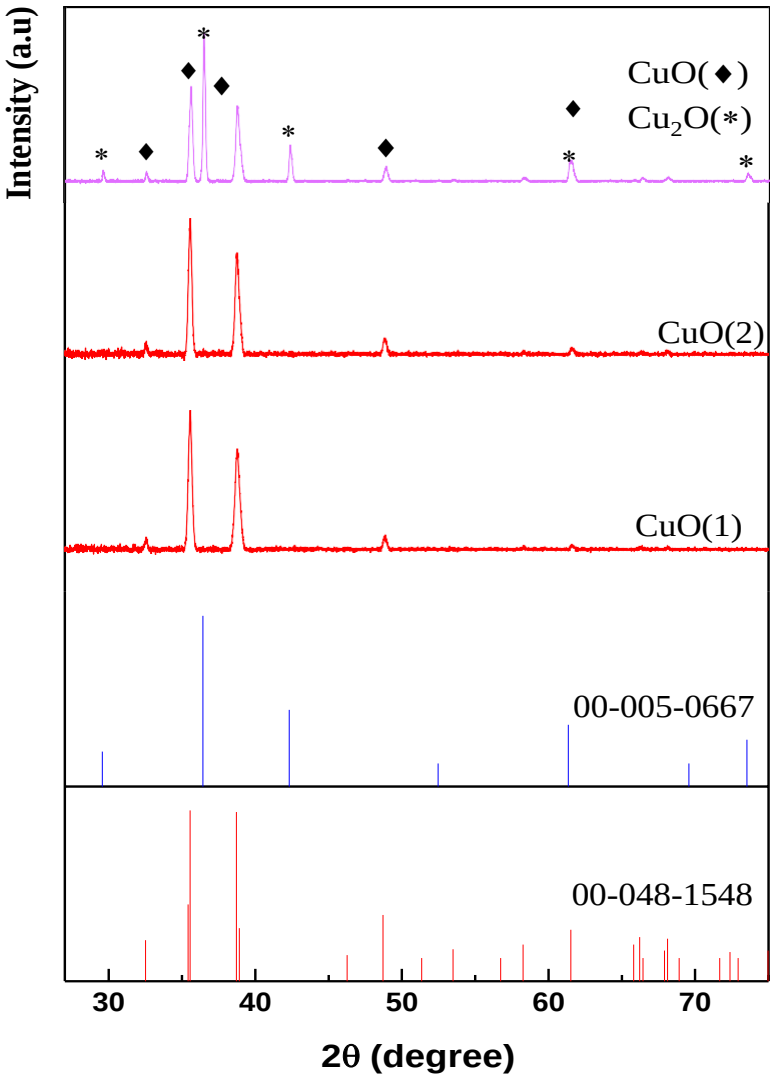

Figure 5. 4: XRD patterns of the copper oxide nanoparticles obtained from copper acetate

5.3.4.Morphological studies of the copper oxide nanoparticles

Figure 5.4. shows the external and internal morphologies of the CuO, presented by their SEM and TEM images, respectively. Figure 5.4 (a) and (b) show the SEM images of CuO(350) and CuO(400) NPs, respectively, which are of spherical morphology and were evenly distributed across the entire structure. The samples obtained at 400 C appeared to be more grain-like which might be due to increased crystallinity resulting from higher calcination temperature. The TEM images, 5.4. (c) and 5.4 (d) confirmed spherical morphology for both CuO(350) and CuO(400), respectively, with an almost uniform diameter. The particle size distribution histogram presented as an inset of Figure 5.4. (c) and 5.4. (d) showed average particle sizes of 47.15 and 47.67, respectively, which weren't too far from the crystalline sizes obtained from the XRD pattern.

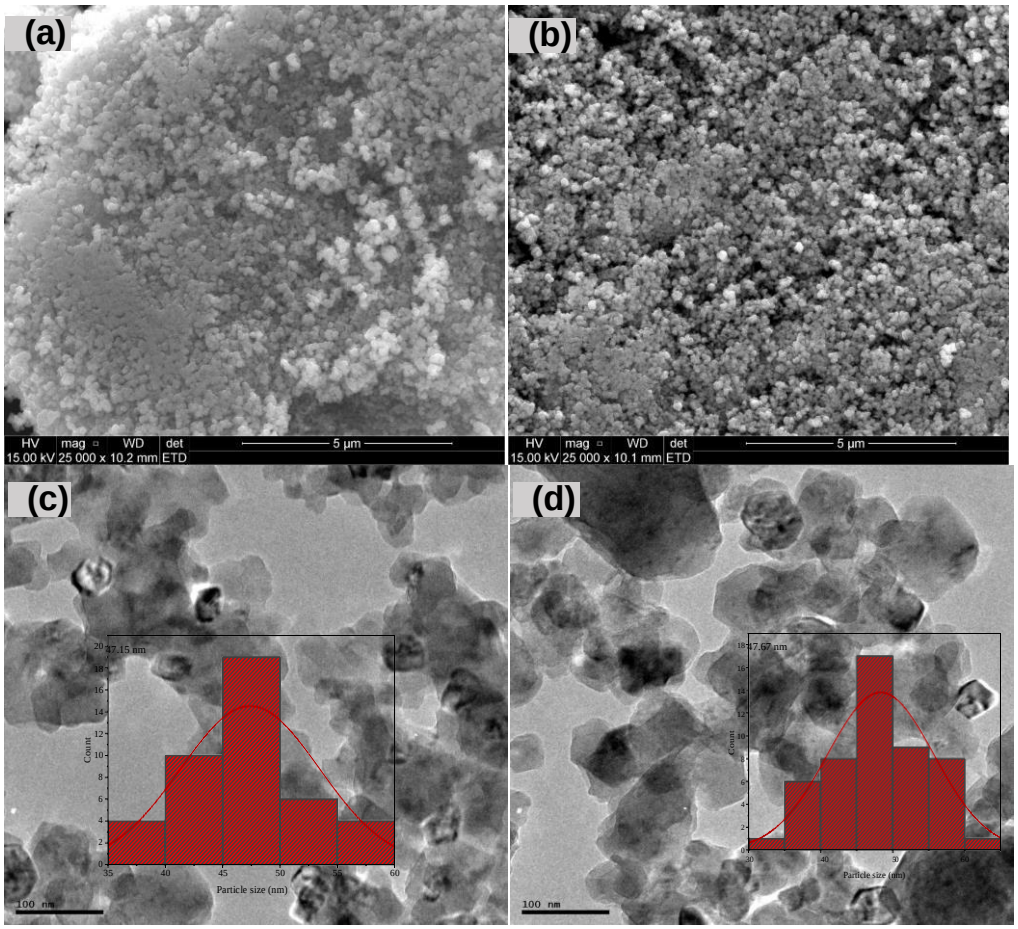

Figure 5. 5: (a, b) SEM and (c,d) TEM images of CuO(350) and CuO(400) NPs respectively, with their particle size distribution histogram in the inset.

5.3.5. UV-vis studies of the copper oxide nanoparticles

The absorption spectra of the synthesized CuO(350) and CuO(400) NPs are shown in Figures 5.5. (a) and (b), respectively. Their spectra show close similarity, with a broad peak from around 446 to around 560 nm, which attained a maximum at around 501 nm and declined to a minimum at around 639 nm. This indicates that the synthesized CuO absorbs in the visible region, excellent optical property of a material that will be used for photocatalysis.

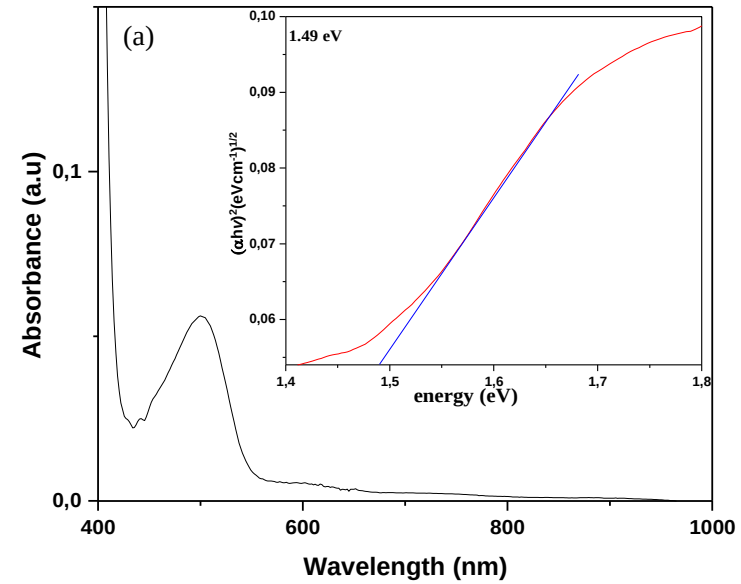

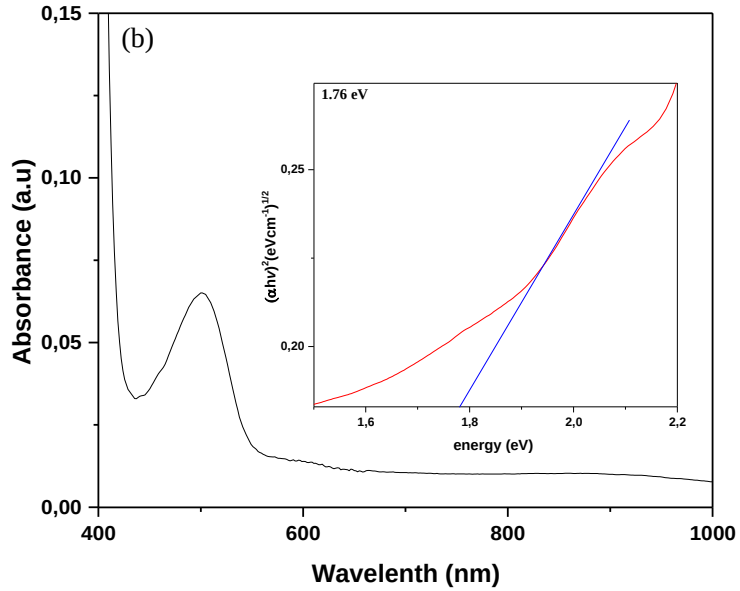

Figure 5. 6: UV-vis- spectra of (a) CuO(350 °C), (b) CuO(400 °C). The insets are the respective Tauc plots.

The bandgap energy is a significant characteristic of a semiconductor catalyst. By using the

Tauc relation:

$$\alpha h\upsilon = \beta(h\upsilon - Eg)^n$$

Where $h\upsilon$ is the photon energy, α is the absorption coefficient, i.e., α=2.303A, and β is the band edge. The n value could be 2 or 0.5 for a direct or indirect transition, respectively [31], the values for the optical band gaps were found to be 1.49 and 1.76 eV for CuO(350 °C) and (b) CuO(400 °C) respectively (inserts). These values are comparable to other similar studies [32] [33]

5.4.0. Photocatalytic degradation of acyclovir over CuO nanoparticles

The removal of antiviral from water has attracted a lot of research attention, and the search for highly efficient photocatalyst that can completely degrade them is a major challenge. This is in the quest for the reduction of their effect on environmental safety and human health. The synthesized CuO nano photocatalysts were studied under visible light irradiation in order to evaluate their ability to degrade acyclovir as a model antiviral compound. Firstly, a solution of acyclovir with the respective CuO nanoparticles was stirred in the dark for about 1 h using a magnetic stirrer to ensure equilibrium was established between the acyclovir and the photocatalysts before the degradation reaction. Thereafter, the reaction mixture was exposed to visible light irradiation with a constant stirring for 2 h for a photodegradation study. The degradation reaction was monitored using UV–Vis absorption spectroscopy. The characteristic absorbance peak of acyclovir around 250 nm was chosen to monitor the degradation reaction.

Figures 5.6.(a) and (b) present the UV–visible absorption spectra of photocatalytic acyclovir degradation as a function of irradiation time under visible light using CuO (350°C) and CuO(400°C), respectively. The graph in both instances indicated that the solution concentration of acyclovir decreased gradually with increased time. Acyclovir is photosensitive and will tend to self-degrade under light without the addition of a catalyst. As shown in Figure 5.6 ((a) and (b)), the intensity of the absorbance decreased continuously during the irradiation process, indicating a reduction in the concentration of acyclovir in the reaction system. In these experiments, both CuO(350°C) and CuO(400°C) demonstrated high and

comparable removal efficiency (94.33%). This might be ascribed to their high absorption of light in the visible region. The high adsorbed photons resulted in an enhancement in their removal rate of acyclovir.

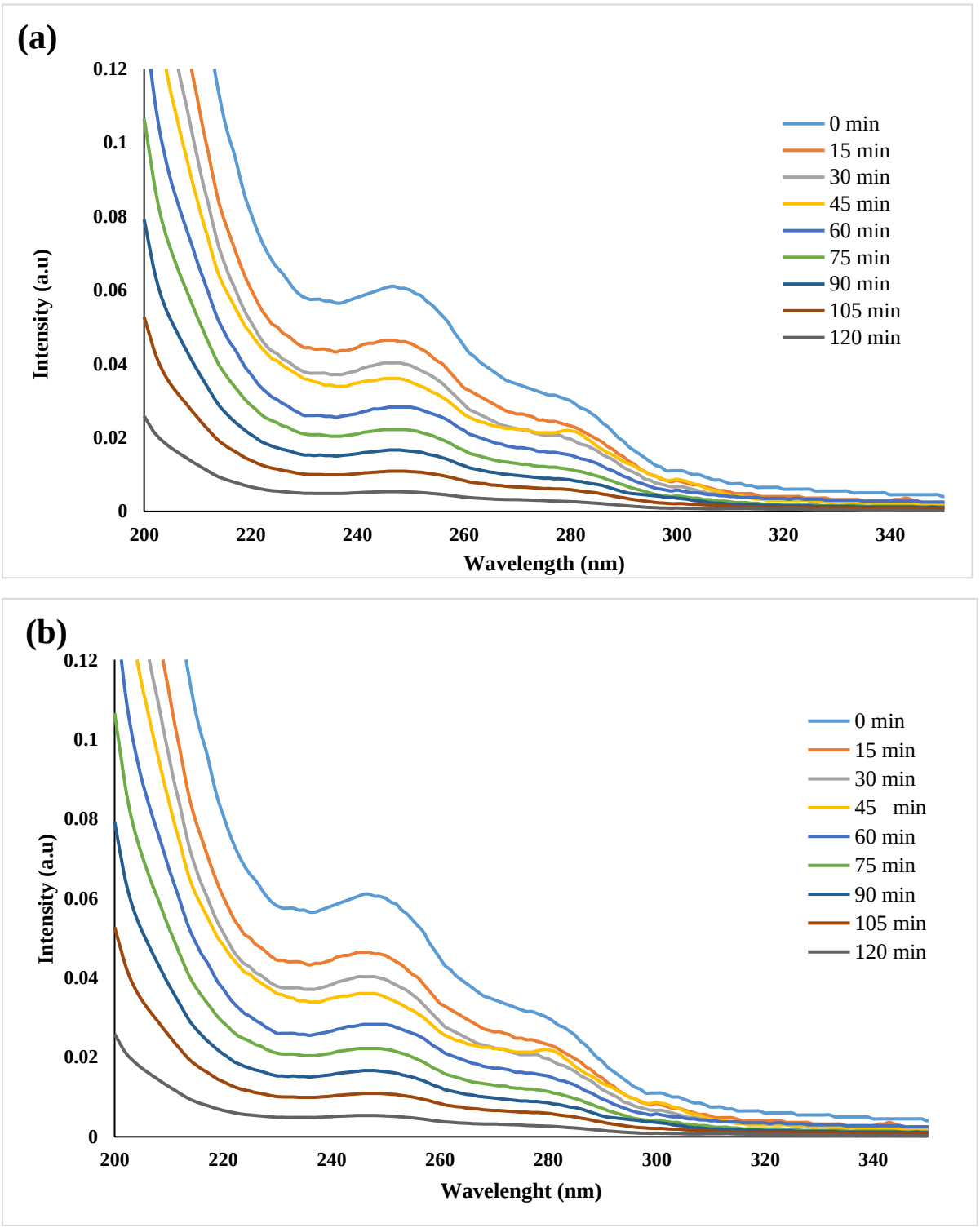

Figure 5. 7: Photocatalytic degradation of acyclovir under visible light irradiation using (a) CuO (350 ºC) and (b) CuO (400 ºC).

5.4.1. The effect of ACV solution pH on the degradation efficiency

The reaction pH is considered one of the main factors affecting photocatalytic activity. Hence, the solutions at different pH (2.0, 4.0, 6.0, 8.0, and 10.0) were prepared, with the adjustment in the pH achieved using 0.1 M NaOH or HCl. The results are presented in Figures 5.7 (a) and (b) for the CuO(350 °C) and CuO(400 °C), respectively. For both CuO(350 °C) and CuO(400 °C), the degradation of ACV increased as the pH solution increased from 2 to 4 but decreased with a further increase in pH to 10. This behavior could be attributed to the electrostatic interaction between the ACV molecules and catalyst at different pH values [34]. The pH of 4 was the favorable pH condition for ACV degradation and might be due to the minimization of electrostatic repulsion.

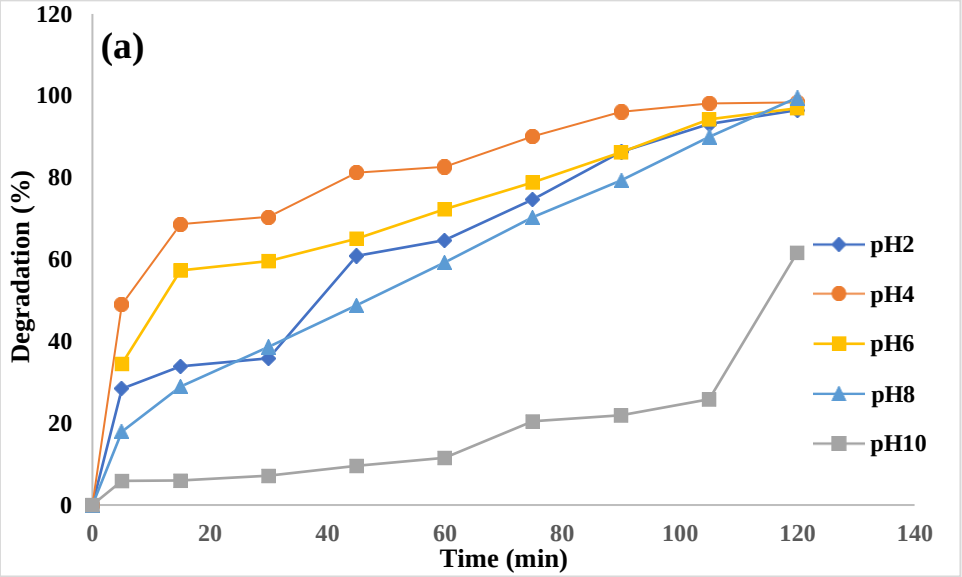

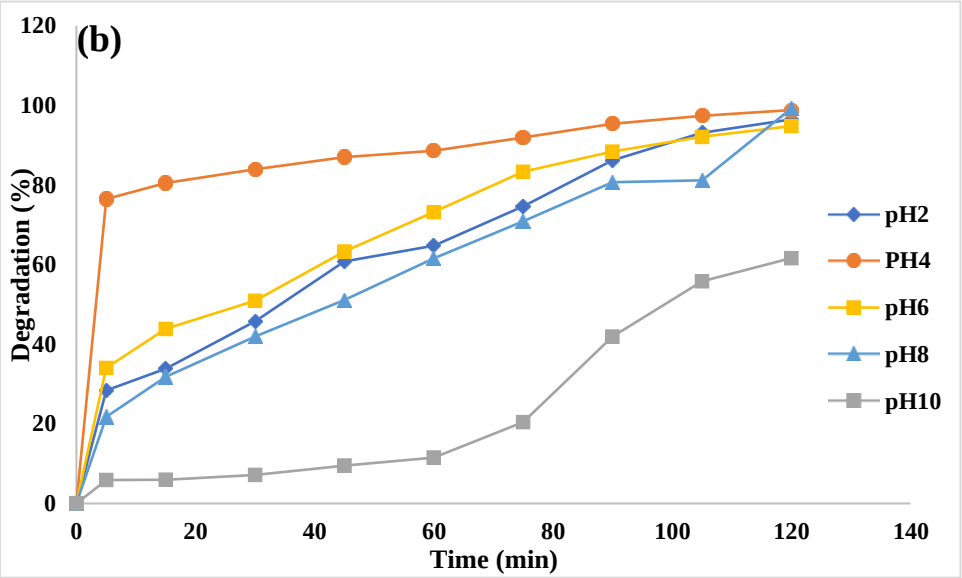

Figure 5. 8: Effect of ACV solution pH on (**a**) CuO (350 °C) and (**b**) CuO 400 (°C) (dosage: 20 mg/L, irradiation time: 120 min, ACV: 1 mg/L).

5.4.2. The effect of catalyst CuO(350) and CuO(400) loading on the degradation efficiency

The effects of the initial concentration of catalyst loading were studied and presented in Figure. 5.8. (a) and (b) respectively. The absence of catalyst showed that the degradation of ACV after 2 h was less than 15%. However, with the gradual increase of the concentration of the catalysts, the degradation rate sequentially and attaining about 72.77, 76.89, 85.58, and 96.61 % with CuO(350°C) and 76.08, 85.38, 95.58, and 99.55 % when CuO(400°C) was used at a concentration of 5, 10, 15 and 20 mg respectively. At high catalyst loading, the amount of photogenerated carriers was increased, which also affected the interaction of carriers with the ACV molecules, thereby increasing its photocatalytic performance. Although high catalyst concentration is not conducive for photocatalytic activity, 20 mg of the CuO exhibited the best photocatalytic performance of ACV removal at the pollutant concentration of 1 mg. Considering the fact that wastewater often has a low concentration of pollutants, 20 mg of the catalyst could be considered as the effective photocatalyst dosage for the degradation of ACV in this experiment.

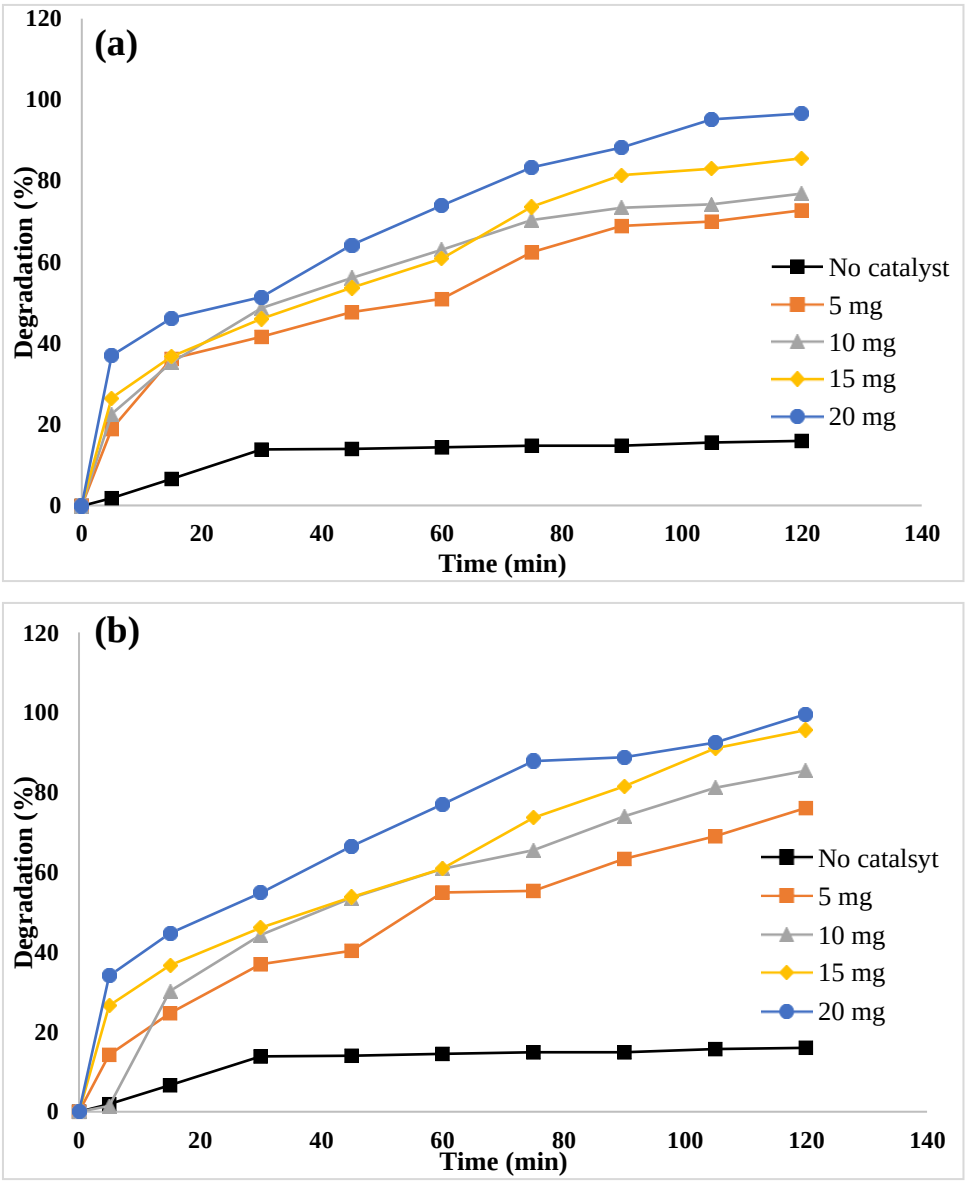

Figure 5. 9: The effect of catalyst loading on the photoreduction of ACV on (**a**) CuO (350 °C) and (**b**) CuO 400 (°C).

5.5.0 Degradation pathway of ACV

Three degradation intermediates have been detected in the photocatalytic degradation of ACV [34], as shown in Figure 5.9. These intermediates include P1, P2, and P3 with t_R3.4 min, 3.0 min, and 2.8 min, respectively. The primary intermediate, P1 (m/z = 214), is first produced during the photocato-degradation process, corresponding to the monohydroxylation of the purine ring and the consequent breakdown of the side chain. The intermediate P2 (m/z = 205)

results from the breakdown of the acyclovir purine ring, and the prolonging of the irradiation time gives rise to P3 (m/z = 152) identified as guanine. This is the product of loss of the side chain.

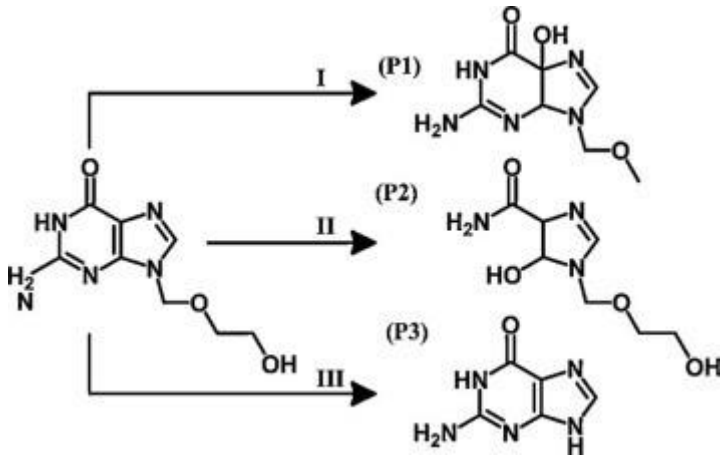

Figure 5. 10: Proposed photocatalytic degradation pathway of acyclovir in water

5.6.0. Conclusion

Nanoparticulate forms of copper tenorite were prepared by a cost-effective thermal decomposition of copper (II) acetate monohydrate. Three calcination temperatures of 300, 350, and 400 C were selected based on the thermogravimetric result, and the as-synthesized samples were characterized. The lowest calcination temperature (300 C) formed a mixed phase of CuO and Cu_2O, while pure copper tenorite phases (CuO) were the products of the calcination temperatures of 350 and 400 C. Both CuO(350) and CuO(400) NPs showed no striking morphological difference as ascertained by scanning and transmission electron microscopies. The as-synthesized CuO(350) and CuO(400) NPs were further utilized for the photo-degradation of acyclovir (ACV) in aqueous solution, and both exhibited good photocatalytic efficiency above 98%. Some of the main factors affecting photocatalytic activity, including solution pH and concentration of the catalyst loading, were evaluated to study their effect on the efficiency of the reaction. The degradation of ACV increased as the pH solution increased from 2 to 4 but decreased with further increase in pH to 10. This behavior could be attributed

to the electrostatic interaction between the ACV molecules and catalyst at different pH values. Initial concentration of catalyst also affected the photodegradation process linearly. This is because, at high catalyst loading, the amount of photogenerated carriers are increased, which also affects the interaction of carriers with the ACV molecules, thereby increasing its photocatalytic performance. The activity of the photocatalyst was attributed to the low bandgap and large surface area.

5.6.0. References

1. Razonable, R.R. *Antiviral drugs for viruses other than human immunodeficiency virus*. in *Mayo Clinic Proceedings*. 2011. Elsevier.
2. Nannou, C., *et al*., *Analytical strategies for the determination of antiviral drugs in the aquatic environment.* Trends in Environmental Analytical Chemistry, 2019. **24**: p. e00071.
3. Prasse, C., *et al*., *Antiviral drugs in wastewater and surface waters: a new pharmaceutical class of environmental relevance?* Environmental science & technology, 2010. **44**(5): p. 1728-1735.
4. Peng, X., *et al.*, *Profile and behavior of antiviral drugs in aquatic environments of the Pearl River Delta, China.* Science of the total environment, 2014. **466**: p. 755-761.
5. Bradley, P.M., et al., *Riverbank filtration potential of pharmaceuticals in a wastewater-impacted stream.* Environmental pollution, 2014. **193**: p. 173-180.
6. Jain, S., *et al.*, *Adsorption optimization of acyclovir on prepared activated carbon.* The Canadian Journal of Chemical Engineering, 2014. **92**(9): p. 1627-1635.
7. Portilla, D., L. Schnackenberg, and R.D. Beger. *Metabolomics as an extension of proteomic analysis: study of acute kidney injury*. in *Seminars in nephrology*. 2007. Elsevier.
8. Bing, J., C. Hu, and L. Zhang, *Enhanced mineralization of pharmaceuticals by surface oxidation over mesoporous γ-Ti-Al2O3 suspension with ozone.* Applied Catalysis B: Environmental, 2017. **202**: p. 118-126.
9. Zhou, C., *et al*., *Photolysis of three antiviral drugs acyclovir, zidovudine and lamivudine in surface freshwater and seawater*. Chemosphere, 2015. **138**: p. 792-797.
10. Jain, S., *et al.*, *Adsorption of antiviral drug, acyclovir from aqueous solution on powdered activated charcoal: kinetics, equilibrium, and thermodynamic studies.* Desalination and Water Treatment, 2014. **52**(25-27): p. 4953-4968.
11. Akbarzadeh, H. and R. Tayebee, *Adsorption mechanism of different acyclovir concentrations on 1–2 nm sized magnetite nanoparticles: A molecular dynamics study.* Journal of molecular liquids, 2018. **254**: p. 64-69.
12. Liu, C., *et al*., *Enhancement of Fe@ porous carbon to be an efficient mediator for peroxymonosulfate activation for oxidation of organic contaminants: Incorporation*

NH2-group into structure of its MOF precursor. Chemical Engineering Journal, 2018. **354**: p. 835-848.

13. Prasse, C., *et al*., *Biotransformation of the antiviral drugs acyclovir and penciclovir in activated sludge treatment.* Environmental science & technology, 2011. **45**(7): p. 2761-2769.
14. Chen, J., *et al*., *Anatase TiO_2 nanoparticles–carbon nanotubes composite: Optimization synthesis and the relationship of photocatalytic degradation activity of acyclovir in water.* Applied Catalysis A: General, 2014. **485**: p. 188-195.
15. Zhang, Y., et al., *Removal of emerging organic contaminants with a pilot-scale biofilter packed with natural manganese oxides.* Chemical Engineering Journal, 2017. **317**: p. 454-460.
16. Orimolade, B.O., et al., *Solar photoelectrocatalytic degradation of ciprofloxacin at a FTO/$BiVO_4$/MnO_2 anode: Kinetics, intermediate products and degradation pathway studies.* Journal of Environmental Chemical Engineering, 2020. **8**(1): p. 103607.
17. Li, J., *et al*., *Controlled synthesis of Fe_2O_3 modified Ag-010$BiVO_4$ heterostructures with enhanced photoelectrochemical activity toward the dye degradation.* Applied Surface Science, 2017. **399**: p. 1-9.
18. Peleyeju, M.G. and E.L. Viljoen, *WO_3-based catalysts for photocatalytic and photoelectrocatalytic removal of organic pollutants from water–A review.* Journal of Water Process Engineering, 2021. **40**: p. 101930.
19. Qin, Y., *et al*., *Fabrication of Bi_2WO6/In_2O_3 photocatalysts with efficient photocatalytic performance for the degradation of organic pollutants: Insight into the role of oxygen vacancy and heterojunction.* Advanced Powder Technology, 2020. **31**(7): p. 2890-2900.
20. Yang, R., *et al*., *PW12/CN@ Bi2WO6 composite photocatalyst prepared based on organic-inorganic hybrid system for removing pollutants in water.* Separation and Purification Technology, 2020. **235**: p. 116270.
21. Yang, Y., *et al*., *Construction of iodine vacancy-rich BiOI/Ag@ AgI Z-scheme heterojunction photocatalysts for visible-light-driven tetracycline degradation: transformation pathways and mechanism insight.* Chemical Engineering Journal, 2018. **349**: p. 808-821.
22. Steinhauer, S., *Gas Sensors Based on Copper Oxide Nanomaterials: A Review.* Chemosensors, 2021. **9**(3): p. 51.

23. Mansour, S., *Thermoanalytical investigations of the decomposition course of copper oxysalts: III. Copper (II) acetate monohydrate.* Journal of Thermal Analysis and Calorimetry, 1996. **46**(1): p. 263-274.
24. Alconchel, S.A., M.A. Ulla, and E.A. Lombardo, *Characterization of freeze-dried precursors of La1. 85Sr0. 15CuO4.* Materials Science and Engineering: B, 1996. **38**(3): p. 205-215.
25. Maslowska, J. and A. Baranowska, *KINETIC-PARAMETERS OF THE THERMAL-DECOMPOSITION OF CU (II) AND ZN (II) SALTS OF CARBOXYLIC-ACIDS.* JOURNAL OF THERMAL ANALYSIS, 1984. **29**(2): p. 309-315.
26. Obaid, A., et al., *Deifallah El-HM: J. Therm. Anal.* Cal, 2000. **61**: p. 985.
27. Lin, Z., D. Han, and S. Li, *Study on thermal decomposition of copper (II) acetate monohydrate in air.* Journal of thermal analysis and calorimetry, 2012. **107**(2): p. 471-475.
28. Diachenko, O., et al., *Structural and Optical Properties of CuO Thin Films Synthesized Using Spray Pyrolysis Method.* Coatings, 2021. **11**(11): p. 1392.
29. Xu, Y., *et al., CuO microflowers composed of nanosheets: Synthesis, characterization, and formation mechanism.* Materials research bulletin, 2007. **42**(9): p. 1723-1731.
30. Mallick, P. and S. Sahu, *Structure, microstructure and optical absorption analysis of CuO nanoparticles synthesized by sol-gel route.* Nanosci. Nanotechnol, 2012. **2**(3): p. 71-74.
31. Aftab, M., *et al., Optical and electrical properties of NiO and Cu-doped NiO thin films synthesized by spray pyrolysis.* Optical Materials, 2021. **119**: p. 111369.
32. Lim, Y.-F., J.J. Choi, and T. Hanrath, *Facile synthesis of colloidal CuO nanocrystals for light-harvesting applications.* Journal of Nanomaterials, 2012. **2012**.
33. Yankson, A., *et al., A low cost synthesis and characterization of CuO nanoparticles for photovoltaic applications.* Ghana Journal of Science, 2019. **60**(1): p. 17-23.
34. Nguyen, T.H.A., *et al., Green synthesis of Nb-doped ZnO nanocomposite for photocatalytic degradation of tetracycline antibiotic under visible light.* Materials Letters, 2021: p. 131129.
35. Li, G., *et al., Can environmental pharmaceuticals be photocatalytically degraded and completely mineralized in water using g-C_3N_4/TiO_2 under visible light irradiation?—Implications of persistent toxic intermediates.* Applied Catalysis B: Environmental, 2016. **180**: p. 726-732.

Chapter 6

Conclusion and Future work

6.0. Conclusion

The continuous release of pharmaceuticals, including antibiotics and antivirals, into the aquatic environment due to human or industrial activities, and the inadequate removal by conventional treatment methods, has inspired the search for viable solutions to this rising global challenge. One promising alternative is the use of photocatalysts since they represent a viable, simple, and highly effective technique with less footprint. Copper chalcogenides are typical II-VI semiconductor materials and have potential as photocatalysts in wastewater treatment processes. This is due to their ability to absorb light in the visible region of the solar spectrum.

In this dissertation, the photocatalytic activity of different copper chalcogenides (Cu2-xS and CuO) was explored for the degradation of an antibiotic (tetracycline) and antiviral (acyclovir) as model pharmaceutics. The copper sulfides and copper oxides were prepared from copper(II) dithiocarbamate and copper acetate respectively as single-source precursor compounds. Effects of reaction temperature as well as capping agent were explored for $Cu_{2-x}S$, which resulted in different crystal phases of the $Cu_{2-x}S$ NPs. The photocatalytic activity of these samples was explored in chapters 3 to 5.

Furthermore, the efficiency of CuO was explored in the degradation of acyclovir (chapter 5).

In chapter 3, hexagonal covellite and rhombohedral digenite phases, obtained via the thermal decomposition of copper(II) dithiocarbamate in oleylamine, were used for the degradation of tetracycline. The results demonstrated that photocatalytic activity of the rod-shaped digenite phase was higher (98.5%) compared to that of spherical shaped covellite phase (88%) within 120 min reaction time. The higher degradation efficiency achieved with the digenite phase was attributed to its higher absorption of visible light compared to covellite. Furthermore, a study of the effect of the concentration of copper sulfide on the photocatalytic properties showed that the activity not only depended on their phases but also strongly depended on the dosage of the catalyst used.

In chapter 4, spherically shaped of djurlite ($Cu_{31}S_{16}$) waas obtained in the solvothermal decomposition of copper(II) dithiocarbamate in dodecanthiol ata temperature below 150 ºC, while roxybyte (Cu_7S_4) of quasi- spherical morphology was synthesized at temperatures

beyond 200 ºC. These copper sulfide phases were also used for the degradation of TC under visible light irradiation. The results of the study showed that Cu_7S_4 (250 °C) exhibited the best activity in the reaction system with the TC degradation rate of up to 99% at pH 4 within 120 min of light exposure, while the $Cu_{31}S_{16}$ (120 °C) system was only 46.5% in the same reaction conditions. The photocatalytic experimental data conform to a pseudo-second-order kinetics model with a higher correlation factor. Overall, roxbyite (Cu7S4) could be considered as a potential catalyst for the degradation of TC in solution.

In Chapter 5, copper oxide nanoparticles were prepared by a cost-effective thermal decomposition of copper(II) acetate monohydrate. Three calcination temperatures of 300, 350, and 400 C were selected based on the thermogravimetric analysis result, and the products labeled as CuO(300), CuO(350), and CuO(400) showed a mixed phase of CuO and Cu2O for CuO(300). However, pure copper tenorite phases (CuO) were obtained for CuO(350) and CuO(400), and both phases showed striking similarities in their optical and morphological properties. They were further utilized for the photo-degradation of acyclovir (ACV) in aqueous solution, and both exhibited good photocatalytic efficiency above 98%.

In conclusion, this study has proven that copper chalcogenides could be used for the degradation of pharmaceuticals in water using visible light irradiation.

6.1. Recommendations for future work

Despite the significant progress made in this study, there are several questions that still need to be addressed to further understand the potential of copper chalcogenides as semiconductors for pharmaceutical degradation in order to promote and gain interest from other researchers in this area of study. The following are recommended for further study:

- The exploration of possible enhancement in the photocatalytic activities by the surface modification of these materials.
- The identification of degradation products using LC-MS should be explored further
- The investigation of the toxicity of the degradation products released during the photocatalytic process.
- The evaluation of the efficiency of these nanoparticles on other pharmaceuticals.
- Carrying out a real sample analysis using effluent from either the clinics or pharmaceutical companies.